INTEGRATED CMOS-BASED BIOCHEMICAL SENSOR MICROSYSTEMS

by

Lei Yao

Department of Electrical and Computer Engineering

McGill University, Montreal

June, 2010

A thesis submitted to McGill University in partial fulfillment of the requirements

of the degree of

Doctor of Philosophy

ACKNOWLEDGEMENTS

First, I would like to thank my advisor, Professor Vamsy Chodavarapu, for his advice, guidance, constant encouragement and inspiration during the past three years of my Ph.D. studies. Without his support, I would not have the opportunity to accomplish what I have achieved in my research work.

I would also like to thank Professor Frank Bright and his students at University of Buffalo for their support on the xerogel sensor materials preparation. I also want to thank Dr. Rosemonde Mandeville and her research group at BioPhage Pharma, Inc. for providing bacteriophages, bacteria materials and biological testing environment. Special thanks go to Philippe Lamarche for his help to enrich my knowledge in microbiology.

I would like to thank all my colleagues in Sensor Microsystems Laboratory for their assistance during the past three years. Special thanks go to Dr. Mohamad Hajj Hassan, Dr. Maurice Cheung, and Dr. Phillipe Roche for their great help to answer my optical, material, and MEMS questions. I would also like to thank Rifat Khan for his support in the experimental data processing and Nasr Madi for his help in the French abstract.

Finally, I am deeply grateful to my parents for their constant love and support, and I would like to thank my friend Yang Luo for her constant encouragement during my writing of this dissertation.

TABLE OF CONTENTS

ABSTRACT

Complementary Metal-Oxide-Semiconductor (CMOS) based sensor systems continue to play an important role in various biomedical, chemical, industrial, food safety, national security and defense, and environmental applications. This is because CMOS fabrication processes would allow one to produce miniaturized systems with low cost, low power and mass-producibility. This dissertation deals with the development of integrated CMOS optical and CMOS electrochemical sensor microsystems for biochemical sensing applications for monitoring of oxygen and bacteria.

The CMOS optical sensor microsystems developed as part of this dissertation are based on the luminometric intensity and lifetime measurement techniques and use sol-gel derived xerogel based sensing elements to encapsulate analyte specific fluorophores in micro-/nano- scale porous structures. The majority of the research efforts have concentrated on the development of oxygen sensor microsystems using CMOS detection and processing circuits. A phase luminometric oxygen sensor system is developed with a novel circuit technique applied to enhance the detection sensitivity performance. Multi-sensor microsystem based on sensor microarrays and custom designed low power CMOS imager is developed to investigate the sensor microarrays imaging and temperature effects on sensor microarrays. Finally, CMOS based Direct Time Interval Measurement (DTIM) method is proposed as a new technique to perform direct luminescence lifetime measurement.

The CMOS electrochemical microsystem developed as a part of this dissertation is based on the conductometric measurement technique and employs bacteriophages as the biological recognition elements (bioreceptors). We focus on the development of CMOS conductometric integrated circuit system which converts the resistance input to a digital output signal. We proposed a novel bacteria activity monitoring system by integrating CMOS conductometric IC with bacteriophages.

In future, based on the principles and prototypes discussed in this dissertation, we can develop novel sensor microsystems for different biochemical sensing applications based on CMOS detection and signal processing in the manner of smaller size, lower cost and equivalent/better performance compared to conventional available instruments.

RÉSUMÉ

Les capteurs en semi-conducteur à oxyde de métal complémentaire (CMOS) continuent d'être cruciaux dans les domaines biomédicaux, chimiques, industriels, environnementaux et autres. La popularité des systèmes CMOS est attribuée à leurs processus de fabrication qui permet de produire des systèmes miniaturisés facile à reproduire en masses à un bas prix et à une basse consommation propre. Cette thèse de doctorat a pour sujet le développement de microsystèmes optiques CMOS intégrés et des capteurs électrochimiques pour surveiller les cultures bactériennes et le taux d'oxygène.

Le capteur optique CMOS développé pour cette thèse est basé sur l'intensité luminométrique et les mesures de durée de vie. Le capteur utilise le sol-gel qui est dérivé des éléments de détection basé sur le Xerogel qui encapsule des fluorophores dans des structures poreuse sur l'échelle micro et nano. La plupart des efforts de recherche sont concentrés sur le développement d'un capteur d'oxygène qui utilise un capteur CMOS et un circuit d'analyse. Dans cette thèse un capteur luminométrique est développé avec un nouveau circuit qui améliore la sensibilité de la détection. Le microsystème de plusieurs capteurs en micro-matrice et d'imageurs a basses consommation personnalisés examine la formation d'image et les effets de la température sur les capteurs en micro-matrice. En plus, nous proposons l'utilisation d'une nouvelles technique CMOS pour mesurer la durée de vie de la luminescence suivant la méthode Direct Time Interval Measurement (DTIM).

Le microsystème électrochimique développé pour cette thèse est basé sur des mesures conductométriques et utilise des bactériophages pour la reconnaissance biologique. Le

système conductometrique intégré CMOS converti la résistance à l'entrée à un signal numérique a la sortie. Nous proposons une nouvelle méthode pour surveiller l'activité bactérienne en intégrant un circuit intégrée conductométrique CMOS avec les bactériophages.

En se basant sur les principes et les prototypes présentés dans cette thèse, on peut développer des nouveaux capteurs pour plusieurs applications d'analyses biochimiques. Les systèmes basés sur la détection CMOS et l'analyse de signaux ont l'avantage d'être plus petits, moins couteux, et plus performants que les instruments conventionnels.

LIST OF FIGURES

LIST OF TABLES

PUBLICATIONS

JOURNAL PUBLICATIONS:

- **L. Yao**, R. Khan, V. P. Chodavarapu, V. Tripathi, F. V. Bright, *"Sensitivity Enhanced CMOS Phase Luminometry System using Xerogel-based Sensors"*, IEEE Transactions on Biomedical Circuits & Systems, vol. 3, pp. 304-311, 2009.

- **L. Yao**, K. Y. Yung, R. Khan, V. P. Chodavarapu, F. V. Bright, *"CMOS Imaging of Pin-Printed Xerogel based Luminescent Sensor Microarrays"*, Accepted in IEEE Sensors Journal, 2010.

- **L. Yao**, K. Y. Yung, V. P. Chodavarapu, F. V. Bright, *"CMOS Imaging of Temperature Effects of Pin-Printed Xerogel Sensor Microarrays"*, Submitted to IEEE Transactions on Biomedical Circuits & Systems, 2010.

- **L. Yao**, V. P. Chodavarapu, *"CMOS based Direct Time Interval Method for Measurement of long-lived luminescence lifetimes"*, Submitted to Electronics Letters, 2010.

- **L. Yao**, P. Lamarche, N. Tawil, R. Khan, A. M. Aliakbar, V. P. Chodavarapu and R. Mandeville, *"CMOS Conductometric System for Growth Monitoring and Sensing of Bacteria"*, Submitted to IEEE Transactions on Biomedical Circuits & Systems, 2010.

- M. Hajj-Hassan, S. J. Kim, M. Cheung, **L. Yao**, V. Chodavarapu, A. Cartwright, *"Porous Silicon and Porous Polymer Substrates for Optical Chemical Sensors"*, Submitted to SPIE Journal of Nanophotonics, 2010.

- P. J. R. Roche, M. C. Cheung, **L. Yao**, A. G. Kirk, V. P. Chodavarapu, *"Enhancement of luminescent quenching based oxygen sensing by gold nanoparticles: a comparison between luminophore:matrix:nanoparticle thin films on glass and gold coated substrates"*, Submitted to Analytica Chimica Acta, 2010.

CONFERENCE PUBLICATIONS:

- P. J. R. Roche, M. C. Cheung, **L. Yao**, A. G. Kirk, V. P. Chodavarapu, *"Enhancement in sensitivity and detection of luminescent quenching based oxygen sensing by gold nanoparticles"*, SPIE Photonics North, Niagara Falls, 2010.

- **L. Yao**, V. Tripathi, K. Yi Yung, V. P. Chodavarapu, A. N. Cartwright, F. V. Bright, *"Enabling Intelligent Readout of Optical Signals from Nanoscale Sensors"*, Invited paper to Proceedings of SPIE Photonics West (BiOS), San Jose, 2009.

- **L. Yao**, M. Hajj-Hassan, V. Chodavarapu, A. Shabani, B. Allain, M. Zourob, R. Mandeville, *"CMOS Imager Microsystem for Multi-Bacteria Detection"*, Proceedings of IEEE NEWCAS Conference, Montreal, 2008.

- **L. Yao**, M. Hajj-Hassan, E. Ghafar-Zadeh, A. Shabani, V. Chodavarapu, M. Zourob, "CMOS Capacitive Sensor System for Bacteria Detection using Phage Organisms", Proceedings of IEEE Canadian Conference on Electrical and Computer Engineering, Niagara Falls, 2008.

CONTRIBUTIONS OF AUTHORS

This dissertation is based on five published, accepted and submitted manuscripts. The candidate, Lei Yao, is the primary author for all these manuscripts.

Chapter 2 is based on the published paper entitled *"Sensitivity Enhanced CMOS Phase Luminometry System using Xerogel-based Sensors"*, IEEE Transactions on Biomedical Circuits & Systems, vol. 3, pp. 304-311, 2009.

Chapter 3 is based on two the following two papers: **L. Yao**, K. Y. Yung, R. Khan, V. P. Chodavarapu, F. V. Bright, *"CMOS Imaging of Pin-Printed Xerogel based Luminescent Sensor Microarrays"*, Accepted in IEEE Sensors Journal, 2010., and *"CMOS Imaging of Temperature Effects of Pin-Printed Xerogel Sensor Microarrays"*, Submitted to IEEE Transactions on Biomedical Circuits & Systems, 2010. The sensor microarrays used in this paper are prepared by K. Y. Yung.

Chapter 4 is based on the following paper: **L. Yao**, V. P. Chodavarapu, *"CMOS based Direct Time Interval Method for Measurement of Long-lived Luminescence Lifetimes"*, submitted to Electronics Letters, 2010.

Chapter 5 is based on the paper submitted to IEEE Transactions on Biomedical Circuits & Systems in 2010: *"CMOS Conductometric System for Growth Monitoring and Sensing of Bacteria"*. The biological materials and methods are provided by Philippe Lamarche and Nancy Tawil at BioPhage Pharma, Inc.

CHAPTER 1 INTRODUCTION AND BACKGROUND

1.1 INTRODUCTION AND HISTORICAL BACKGROUND OF SENSORS

Sensors play an important role in almost every aspect of modern human society. Sensors are the most ubiquitous devices with which one would have a direct or indirect interaction each day. From accelerometers in airbag release systems, capacitive touch sensitive screens in smartphones, glucose test strips and pace makers to gene chips to mass spectrometers used by space probes searching for alien life forms in our galaxy all require different sensors. Thus, integrated sensor systems have a tremendous influence on our social wellbeing and economic growth and development.

First, it is important to define the meaning of what is a sensor, in simple terms it is a device that gives a signal for the detection or measurement of a physical, chemical, or biological property to which it responds. Our human body itself relies upon a number of sensors: eyes respond and detect light signals, ears detect sound signals, nose detects different odors and tongue detects different chemicals, etc. Since the dawn of history, humans have been known to use many nature-mimetic and bio-mimetic sensory devices for thousands of years. However, Galileo Galilei in 17^{th} century is often credited with inventing the thermoscope which is recognized as the first physical sensor in the human history [1]. Since then, there are numerous examples of people developing and using sensors for many applications.

Historically, physical properties that humans could directly feel/see/hear such as temperature, pressure, sound and weight are the first things that people wanted to quantize and analyze. Since the industrial revolution in late 18th century, people have been developing these very sensors for industrial applications and scientific explorations. Eugene Bourdon invented Bourdon tube [2-3] in 1849 used as a pressure sensor which is still one of the most widely used instruments for measuring the pressure of liquids and gases of all kinds. The invention of the acoustic sensor (telephone) patented by Alexander Graham Bell in 1876 [4] may be the most remarkable development of the sensor technology in the 19th century. Along with the fast development of analytical chemistry in the 19th century, chemical sensors emerged to help quantize and identify chemical components and reactions. Hughes developed the first portable chemical sensor used to determine the pH of the chemical solutions in the 1922 [5]. Drunkometer was first used in the criminal investigations to detect alcohol in the human breath in 1927 [6].

An important chemical sensor invention in the 20th century was the oxygen (O_2) sensor developed by Lenard Clark in 1954 [7] which is considered as the first biological sensor or biosensor. In 1962, Lenard Clark again developed another important biosensor namely glucose sensor [8], which later become the market driver for the biosensor industry for the next few decades and to date. Since the first biosensor was developed, the rapid technological advances in engineering, chemistry, biology and medicine in the late 20th century and the increasing concern on human healthcare, environment protection and biological research have led to the recent advancements in sensor technology focusing on the development of sensors for biological applications such as bacteria detection [9-10], DNA sequencing [11-12], drug discovery [13-14] and protein engineering [15] .

1.2 SENSOR SYSTEMS

Sensor system architecture is first introduced in this section. The sensor system classification into the three different types based on the different transducer types in the sensor system is discussed next, followed by discussion on the performance and practicability issues of the sensor system. Finally, the current research focus on sensor system is discussed.

1.2.1 SENSOR SYSTEM ARCHITECTURE

The general architecture of a modern sensor system is shown in Figure 1.1. The sensor responds to the information of interest through the sampling aperture and gives out a signal which is then converted by a transducer into an easily understandable signal (e.g.,

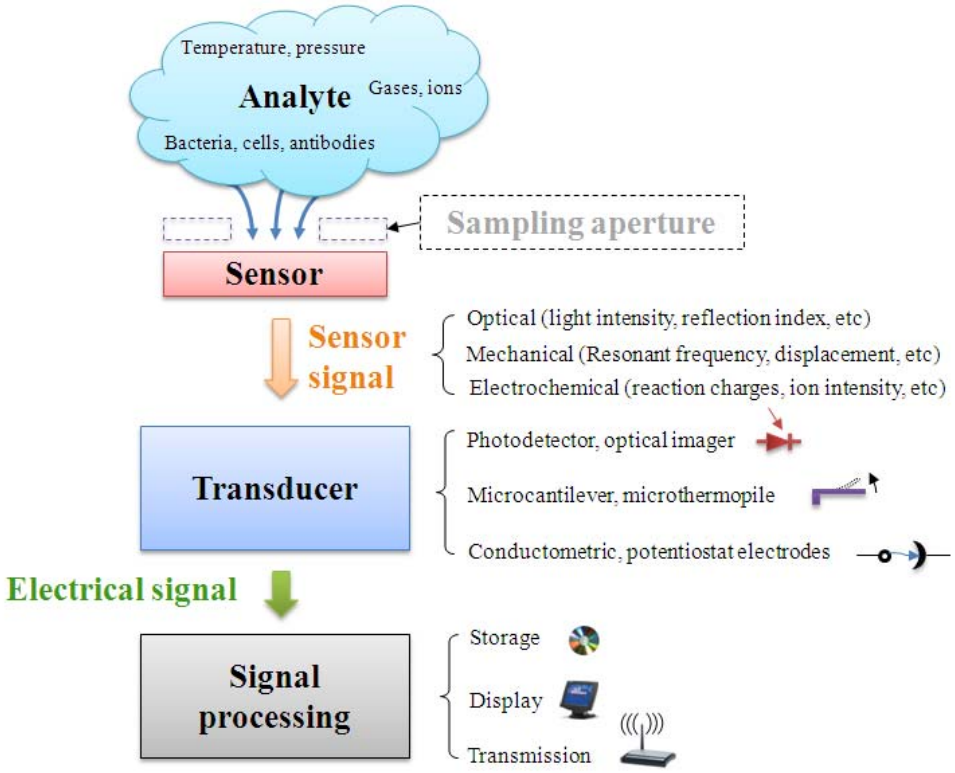

Figure 1.1 Typical architecture of sensor system

electrical or optical signal) for further processing, storing or distribution. The information of interest can be physical properties such as temperature and pressure or biological and chemical entities such as ions, bacteria etc. The sampling aperture in a sensor system is often considered as a non-essential component in most other literatures. However, the recent increasing demands in acquiring and conditioning fluidic samples for biochemical applications and the requirements for packaging integrated sensor systems make the sampling aperture important for many advanced sensor systems. Based on the sensor response mechanism and construction, sensors give out different sensor signals which could be optical, mechanical or electrochemical. Before further processing, these signals in different forms are converted into electrical signals by a transducer due to the fact that the modern electronics industry is well established and it is the most preferable way for information storage, display, analyzing and transmission. This situation might change if a new technology for information processing becomes mature such as the optical signal processing and optical computing, in which case the output of the transducer could be shifted to an optical signal.

1.2.2 SENSOR SYSTEM CLASSIFICATION

The sensor system can be classified according to various aspects depending on their analyte, sensor signal, transducer or operational characteristics. In this dissertation, the sensor system is classified into three main types based on the type of sensor signal or the type of transducer: mechanical, optical, and electrochemical.

Mechanical: Mechanical sensors are the oldest and most widely used sensor systems. They sense the mechanical property change such as mechanical expansion, reflection, distortion, etc. As mentioned before, the first sensor in human history is a temperature

sensor and it is based on the mechanical expansion of air to measure temperature [1]. Typical mechanical sensors include microphones [16-17], accelerometers [18-19], gyroscopes [20-21], etc. They are widely used in industrial process control, navigation, consumer electronics, and scientific research.

Optical: The widespread use of optical sensor systems began from the first practical photodector invented in 1934 for television industry [22]. Photomultiplier tubes (PMTs), Charge coupled devices (CCDs) and photodiodes are typical optical sensors. In addition to their widespread application in camera and television industry, the optical sensor system is also widely used as effective analytical methods in non-intrusive medical diagnostics and scientific research [23-26] because of the spatial transmission ability and the special spectrum characteristics of the optical signal.

Electrochemical: Electrochemical sensor systems were initially used to help analyze the chemical reactions and identify chemical components. The information in the chemical solution is interpreted by the electrical information collected through the electrodes inserted into the test solutions. All electrochemical sensors have similar constructional structure which is electrodes in specific configurations placed in the sample solutions. They are widely used in the biochemical industry and research [27-31] because of their simple structure and user-friendly interface with both biochemical environments and electrical environments.

Works presented in this thesis is focused on the optical sensor systems and electrochemical sensor systems. Before introducing these works, initial motivations of these works will be discussed.

1.2.3 CHARACTERIZATION OF SENSOR SYSTEM

To build a “better” sensor system is always a motivation for scientific and industrial research. First, the word “better” has to be clearly defined through the characterization of sensor system. Basically a sensor system can be classified according to 1) performance characterization and 2) practicality characterization. The performance characterization is the technical characterization of a sensor system regardless of any practical limitations. Some important performance characteristics are described as follows:

Selectivity: Selectivity is the essence of sensor systems. It can be defined as the ratio of the sensor's response to the analyte of interest to its response to other analytes not of interest. For an ideal sensor system the selectivity is infinity which means it only responds to the analyte of interest.

Sensitivity: Sensitivity is defined as the input parameter (i.e. gas concentration) change that is required to produce a standardized output change. To be more specific, for example, in a linear sensor system, the sensitivity is the slope of the calibration curve. While in a non-linear system, the sensitivity at any operational point is the derivative of the calibration curve at that particular operational point.

Resolution: Resolution is the minimum input (i.e. lowest gas concentration) given to the sensor system that can produce a detectable change at the output. It is closely related to the noise figure of the sensor system. In most cases the noise level of the sensor system decides the resolution of the sensor system.

Response time: Response time is defined as the time the sensor system takes to react to a change in the input. In a sensor system, many factors can affect the system response

time including the sensor's response time, the transducer's response time and the electrical signal processing module's response time.

Repeatability: Repeatability presents the stability of the sensor system. It is essentially the indication of the sensor system's noise and error level.

Lifetime: Lifetime is the maximum time period that a sensor system can operate within its specified performance since it has been manufactured. This parameter is particularly important for biochemical sensor systems which are used in the medical field since the failure of sensor system would cause vital consequences.

The characteristics listed above describe the performance of a sensor system. However, to develop a sensor system which can fit into a specific application and environment, the following practicality characterizations has to be considered carefully:

Size: The size of the sensor system is always one of the major concerns in many applications. Smaller dimensions provide a lot of advantages such as portability, light-weight, easy to use, etc. The recent increasing demands for implantable sensors in the biomedical field have stressed this characteristic.

Cost: Low cost sensor system is always preferable for industrial applications and one of the important goals in scientific researches. Lower cost means more competitive and easy to be widely used.

Power Consumption: Power consumption is a major concern in portable (battery supported) handheld sensor systems. Long sensor lifetime is an important characteristic

in many applications and particularly in implantable sensor systems in which changing of a battery is a tedious procedure.

Packaging and compatibility: The packaging of the sensor system is critical for the sensor system used in some special environments, especially the sensor systems related to biochemical applications. The packaging has to isolate the sensor system (except the aperture part which is in contact with the sample) from the environment to avoid any possible cross-talk and damage to either the sensor system or the surrounding environment.

To enhance the performance and improve the practicality of sensor systems, many research works have been done in both the industry and universities [32-42]. One of the major developments is the sensor system miniaturization or also called sensor microsystems, which is initially driven by the demands for portable/implantable sensor systems, and is enabled by the fast development of the semiconductor technology since 1970s. Sensor microsystems offer tremendous advantages compared to conventional sensor systems including smaller size, lower noise, higher resolution, lower cost due to the mass-production, and smarter system and have been under intensive investigation in the past 40 years.

1.2.4 SENSOR SYSTEMS INTEGRATION

The great success of the semiconductor technology in 20^{th} century is a driving force for the sensor system integration. The emergence of versatile electrical information processing devices such as microprocessors and CPUs enable the possibility of a micro-scale sensor system. From late 1970s, researchers started to take advantage of the well

established semiconductor technology to construct miniaturized sensors and transducers for different applications [43-45]. The current most popular methods for sensor system integration are Complementary Metal-Oxide-Semiconductor (CMOS) and Micro Electro-Mechanical System (MEMS).

CMOS: CMOS (Complementary Metal-Oxide-Semiconductor) currently is the dominant technology in semiconductor field for microelectronics devices and integrated circuit (IC) fabrication which can have millions of transistors within 1 millimeter by 1 millimeter square area that perform complex functions [46]. The electrical signal processing module in a sensor system can be fully integrated monolithically through CMOS technology. Many research efforts are made to develop application specific integrated circuits (ASICs) for different types of sensor systems [39-42]. Besides the electrical signal processing module, CMOS technology can also be applied to implement transducers such as the well known CMOS optical imager [42, 47] and electrochemical sensors such as ISFET [48], BioFET [49], etc.

MEMS: MEMS (Micro Electro-Mechanical System) is an important method used for device fabrication in the semiconductor technology. It has the ability to fabricate 3D micro structures such as micro-cantilevers, mirrors, and gear wheels employing similar fabrication processes as in IC fabrication using surface micromachining or bulk micromachining. MEMS is the most widely used method to fabricate micro-sensors [50-52] and micro-transducers [53-56]. It is highly compatible with IC fabrication, which makes it a popular method if not the only method to realize monolithic sensor microsystems [57-59].

Besides CMOS and MEMS technologies, there are also other technologies used in integrated sensor systems such as 3D printing [60], laser polymerization [61], microfluidics [62], etc. These technologies are specific for certain applications (i.e. microfluidics for aquatic environment) and are not discussed in this dissertation.

The work presented in this dissertation is focused on CMOS based integrated sensor systems for biochemical sensing applications: Optical Oxygen Sensor System and Electrochemical Bacterial Sensor System. The fundamentals of these two systems are introduced in the following sections.

1.3 OPTICAL OXYGEN SENSOR SYSTEMS

Oxygen detection is one of the most important sensor applications in biochemical analyzing, clinical surgery, food/beverage safety, environment monitoring, etc [63]. There are different kinds of oxygen sensors based on electrochemical (Winkle titration and Clark Electrode [7]) and optical (Fluorometric) sensing mechanism. Fluorometric oxygen sensor is based on the principles of fluorescence spectroscopy. Generally speaking, fluorescence spectroscopy provides more advantages than the conventional electrochemical methods for biochemical applications since it does not consume oxygen (critical for clinical applications), it has high sensitivity in lower concentration ranges, it has a fast response time and it is able to monitor oxygen concentration in the gaseous environment [63].

1.3.1 FLUORESCENCE SPECTROSCOPY

Fluorescence spectroscopy is one of the oldest and most popular analytical techniques in chemical and biological sensor applications [64]. It is classified as a branch of

photoluminescence in the luminescence family. Luminescence is the emission of light from any substrate at low temperature distinguishing itself from incandescence which is the light emission at a high temperature (above 750K). There are different kinds of luminescence based on the different excitation sources such as chemoluminescence, electroluminininescence, bioluminescence, photoluminescence, etc. Photoluminescence by its name is the luminescence caused by the photonic excitation, in which a fluorophore substance (i.e. Quinine, ethidium bromide) is excited by photons of light with short wavelength or, in another words, higher energy.

The photoluminescence process is illustrated in Figure 1.2. S_0, S_1 and S_2 are the ground, first and second energy level for the electrons of the photoluminescent chemical compound respectively. At each level, there can be several vibrational energy states denoted as 0, 1, 2, etc. The electrons absorb the excitation photon's energy and are excited to higher energy levels (S_1, S_2 or their sub-vibrational energy states). After the excitation, within a very short time (on the order of picoseconds or less) the excited electrons may undergo some internal conversions from higher vibration energy states to the lower ones. There are two possibilities after this internal conversion depending on the different types of photoluminophores. In one case, these excited electrons at the lowest vibration state of higher energy level ($S_{1\text{-}0}$ in Figure 1.2) return to the ground level (S_0) along with light emission (energy releasing) in the form of *fluorescence*. In the other case, these excited electrons undergo an *intersystem crossing* process to a *triplet state*. The electrons trapped in the *triplet state* can also return back to the ground energy level along with light emission but at a much slower rate (milliseconds to hours) due to the fact that the electron transition from a *triplet state* to the ground level is kinetically not favored. This slow emission is known as *phosphorescence*.

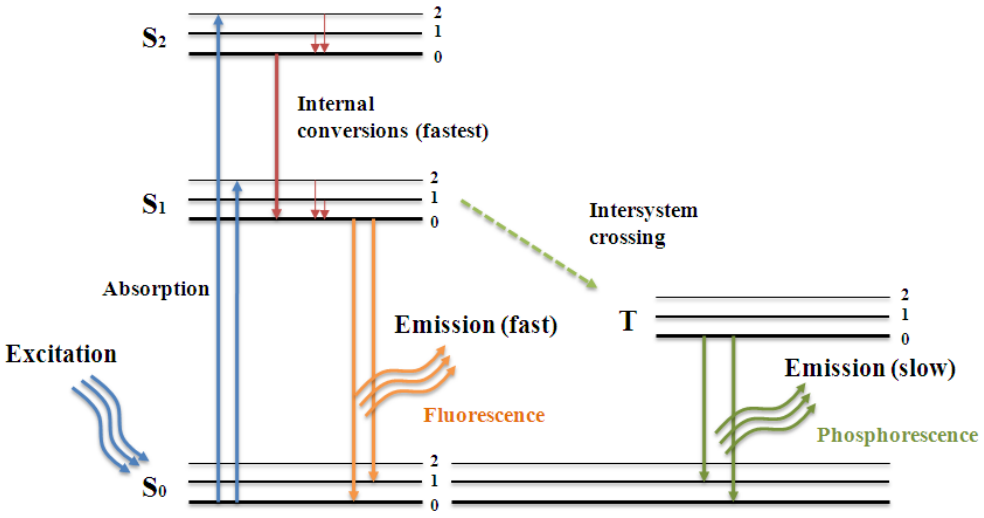

Figure 1.2 Block diagram of photoluminescence process

The works in this dissertation concentrate on the fluorescence and its properties. The fundamental properties of fluorescent substance (fluorophore) can be used as sensing material in that the emitted fluorescence can be *quenched* by molecules specific to the fluorophore [64] and this quenching results in changes in the properties of the emitted fluorescence such as intensity and excited state luminescence life-time. By calibrating the intensity or the life-time of the emitted fluorescence, the molecule which quenches the fluorescence (quencher) can be identified and quantized. There are several quenching mechanisms such as collisional or dynamic quenching, static quenching, energy transfer quenching, and charge transfer reaction quenching. The collisional quenching is related to the works in this dissertation and will be discussed in detail. The details of other quenching mechanisms can be found in [64].

In the collisional quenching, the quencher collides and interacts with the fluorophore. A simplified fluorescence process diagram is shown in Figure 1.3, assuming the fluorophore is under constant excitation, *G(t)*. When the quencher is absent, there are two

ways for the excited electrons to return to the ground state: radiative emission (fluorescence) and non-radiative dissipation (heat, atoms rotation, etc.). Γ is the radiative emission rate and k_{nr} is the non-radiative decay rate. Under constant excitation, the number of the excited electrons on S_1 will get balanced and fixed. The balance in this scenario can be described as:

$$\frac{dn_0(t)}{dt} = G(t) - (\Gamma + k_{nr})n_0(t) = 0 \qquad (1.1)$$

where, $n_0(t)$ is the number of excited electrons stays on S_1.

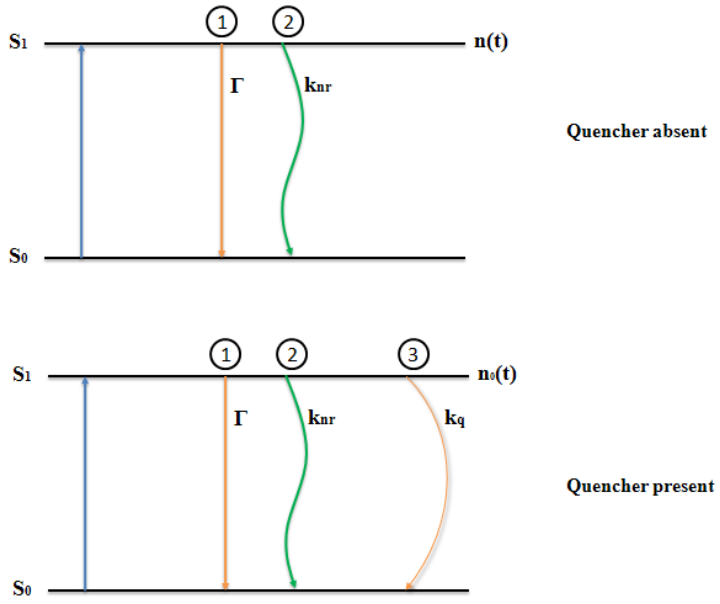

Figure 1.3 Black diagram of fluorescence process with and without collisional quenching

When the quencher is present and interacts with the fluorophore, another alternative way for the excited electrons to return to the ground state appears: collisional interaction. $k_q[Q]$ presents the collisional interaction rate which is related to the quencher parameter

[Q] such as partial pressure, concentration, etc. The balance in the quencher present scenario is described as:

$$\frac{dn(t)}{dt} = G(t) - (\Gamma + k_{nr} + k_q[Q])n(t) = 0 \tag{1.2}$$

where, n(t) is the number of excited electrons stays on S_1 in the quencher present case.

The lifetime of the fluorescence is defined as the time it takes for the fluorescence to decay after a pulse stimulation and it can be expressed as [64]:

$$\tau_0 = \left(\Gamma + k_{nr}\right)^{-1} \tag{1.3}$$

$$\tau = \left(\Gamma + k_{nr} + k_q[Q]\right)^{-1} \tag{1.4}$$

where, τ_0 is the life-time with quencher absent and τ is the life-time with quencher present.

The division of Equation 1.1 and 1.2 yields:

$$\frac{n_0(t)}{n(t)} = 1 + k_q\tau_0[Q] \tag{1.5}$$

Since the intensity of the emitted fluorescence is proportional to the number of the excited electrons, Equation 1.5 can be rewritten as:

$$\frac{I_0}{I} = 1 + k_q \tau_0 [Q] \tag{1.6}$$

which is the well-known Stern-Volmer equation.

The division of Equations 1.3 and 1.4 gives:

$$\frac{\tau_0}{\tau} = 1 + k_q \tau_0 [Q] \tag{1.7}$$

indicating an equivalent decrease in the lifetime to the intensity during the collisional quenching. Equations 1.6 and 1.7 represent the relationship between the fluorescence's property (intensity, life-time) and the quencher's property [Q]. By calibrating the intensity or lifetime of the fluorescence, [Q] can be quantized. This is the very basic fundamental property for the fluorometric oxygen sensors presented in this dissertation.

1.3.2 OXYGEN SENSOR LAYER: FLUOROPHORE AND XEROGEL

To develop a practical sensing layer using the fluorometric method discussed above, a fluorophore which can be quenched by the analyte and an appropriate immobilization method has to be selected.

Fluorophore: Fluorophore is fluorescence substance that absorbs energy at a specific wavelength typically in the range of ultra-violet/visible electromagnetic radiations with short wavelengths (higher energy) and emits energy at longer wavelengths (lower energy). Fluorophores that are widely used in oxygen detection include tris(4,7-diphenyl-1,10-phenanthroline) ruthenium(II) ($[Ru(dpp)_3]^{2+}$) and *tris*(2,2'-bipyridyl)

dichlororuthenium(II) hexahydrate ($[Ru(bpy)_3]^{2+}$) [64] which are employed in this dissertation. A typical absorption and emission spectrum for the fluorophore $[Ru(dpp)_3]^{2+}$ is shown in Figure 1.4. To implement sensor systems using fluorophores, several important characteristics need to be understood very well in this figure. First, the excitation source has to be carefully selected so that the wavelength spectrum of the source (LED Em. in Figure 1.4) resides within the maximum absorption wavelength range of the fluorophore absorption spectrum ($[Ru(dpp)_3]^{2+}$ Abs. in Figure 1.4). Secondly, an optical filter (565 LP) is required to remove the source excitation and let fluorescence emission ($[Ru(dpp)_3]^{2+}$ Em.) pass through for photonic detection. As seen from the figure there is also residual emission (LED Em. x100) after filtering which may influence the overall performance of the fluorometric sensor system.

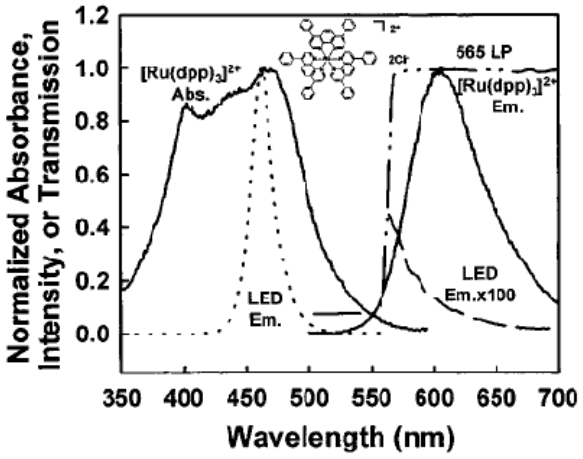

Figure 1.4 Absorption and emission spectrum for $[Ru(dpp)_3]^{2+}$, taken from [65]

To form a stable and reliable sensor layer, a good immobilization method has to be applied to encapsulate the fluorophore within the sensor layer. Xerogels are selected as the immobilization method in this dissertation.

Xerogel and *sol-gel* process: Xerogel is a material which has been widely used for the development of sensors [41, 66-67]. It has special characteristics and advantages to make itself a suitable for encapsulating materials for fluorometric sensing system such as optical transparency in visible spectrum, does not interact with fluorophores, porous structure for the quencher's molecules to access fluorophores, structural stability, good thermal stability, etc. Xerogel is the ambient conditioned product of a chemical process named *sol-gel* process which involves conversion of a *sol* (solution) containing colloidal particles with dimension on the order of 1-100nm into a *gel* which is a rigid porous networks with dimensions up to micro-scale. The *sol-gel* process technique has been used to create a variety of glasses, ceramics, and composite/hybrid materials. The *sol-gel* chemical process can be performed at low temperature ambient conditions and is widely used to create materials and devices of different forms and shapes incuding monoliths, waveguides, coatings, thin films, fibers, pin-printed spots, etc. Its nano-/micro- structured pores can be used for reliably encapsulating various biochemical recognition elements for the development of sensors. When the processing occurs under ambient conditions, the resulting materials are called xerogels. The *sol-gel* process offers a number of other advantages for the development of biochemical sensing elements such as:

- optical transparency in the visible region of the electromagnetic spectrum
- accessibility of the biochemical recognition element to the analyte
- good thermal stability
- tunable sensitivity
- structural stability
- Biocompatibility
- not altering the physiochemical properties of the entrapped molecule
- being compatible with a wide variety of fluorophores and biomolecules

As just mentioned, the *sol-gel* process involves conversion of a *sol* (solution) containing colloidal particles with dimensions on the order of 1-100 nm into a *gel*, which is a rigid porous network with dimensions typically in the micro/nano-scale. Three main chemical processes occur during the *sol-gel* process: hydrolysis, condensation and drying/aging. The typical *sol-gel* process is illustrated in Figure 1.5. The first step is hydrolysis. Hydrolysis is a chemical reaction during which molecules of water (H_2O) are split into hydrogen cations (H^+) and hydroxide anions (OH^-) in the process of a chemical mechanism. Alkoxide precursors such as TEOS (chemical formula: $Si(OC_2H_5)_4$) and TMOS (chemical formula: $Si(OCH_3)_4$) are popularly used in *sol-gel* process because they react readily with water to allow the hydrolysis process to take place. During the hydrolysis of the alkoxide precursors for example TEOS, a hydroxyl ion becomes attached to the silicon atom as follows:

$$Si(OR)_4 + H_2O \rightarrow HO - Si(OR)_3 + R - OH$$

where, R represents the alkyl group C_2H_5. Depending on the amount of water and catalyst present, hydrolysis may proceed to completion, so that all of the OR groups are replaced by OH groups, as follows:

$$Si(OR)_4 + H_2O \rightarrow Si(OH)_3 + 4R - OH$$

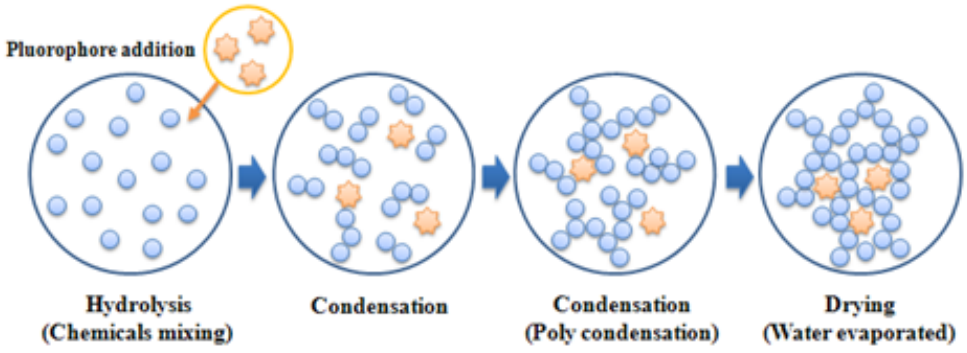

Figure 1.5 Typical chemical process of *sol-gel* and xerogel based sensor layer development

Any intermediate species such as $(OR)_2$–Si-$(OH)_2$ or $(OR)_3$–Si-(OH) would be considered the result of partial hydrolysis. In addition, two partially hydrolyzed molecules can link together in a condensation reaction to form a siloxane Si–O–Si bond:

$$(OR)_3 - Si - OH + HO - Si - (OR)_3 \rightarrow [(OR)_3 Si - O - Si(OR)_3] + H - O - H$$
$$(OR)_3 - Si - OR + HO - Si - (OR)_3 \rightarrow [(OR)_3 Si - O - Si(OR)_3] + R - O - H$$

Thus, the three dimensional network of siloxane Si–O–Si bonds is formed accompanied by the production of H-O-H and R-O-H species. After the condensation, drying process (normally heating under a certain temperature) is used to remove the accompanied products H-O-H and R-O-H. The temperature and time set for the drying process controls the property of the final product - siloxane network based polymer, one of which is the xerogel.

1.3.3 CMOS LUMINOMETRIC OXYGEN SENSOR SYSTEM

As explained before the luminometric (more general term for fluorometric) method for oxygen sensing offers a number of advantages over the conventional electrochemical methods, however, one of the drawbacks for the luminometric method is that it requires a transducer to convert the optical signal, in most cases these are very weak optical signals, into an electrical signal for further processing and analyzing. Conventionally, the optical signal detection in these sensors is done using sensitive and low noise photodetection devices such as photomultiplier tubes (PMTs) and charge coupled devices (CCDs) [68-71] . PMTs and CCDs are the primary photodetectors that people used to employ to obtain reliable data from luminometric sensor systems till the last decade after which the use of CMOS photodetector emerged [41, 72-73]. The attraction of using a CMOS

photodetector, as opposed to the PMTs and CCDs, is the possibility of integrating signal detector elements or arrays of detector elements with on-chip processing circuitry in a low cost, efficient, and portable fashion. Though the relative low performance remains an issue for CMOS photodetector and it still needs to be improved before their widespread use in practical field applications, prototypes of CMOS based luminometric sensor systems has been proposed by many researchers previously [41-42, 66-67, 74].

A general diagram of the CMOS based luminometric sensor system can be presented as shown in Figure 1.6. The excitation source excites the luminophores (more general term for fluorophores) which are encapsulated in the xerogel matrix. The luminescence (more general term for fluorescence) emission passes through an optical filter which is used to remove the excitation and which is then detected by the CMOS detection IC. Based on the calibrated intensity or life-time of the luminescence, property of the analyte (concentration, partial pressure, etc.) can be obtained using Equations 1.6 and 1.7. As mentioned before the CMOS based luminometric sensor systems still needs to be improved before practical applications. In this dissertation, different circuit techniques are

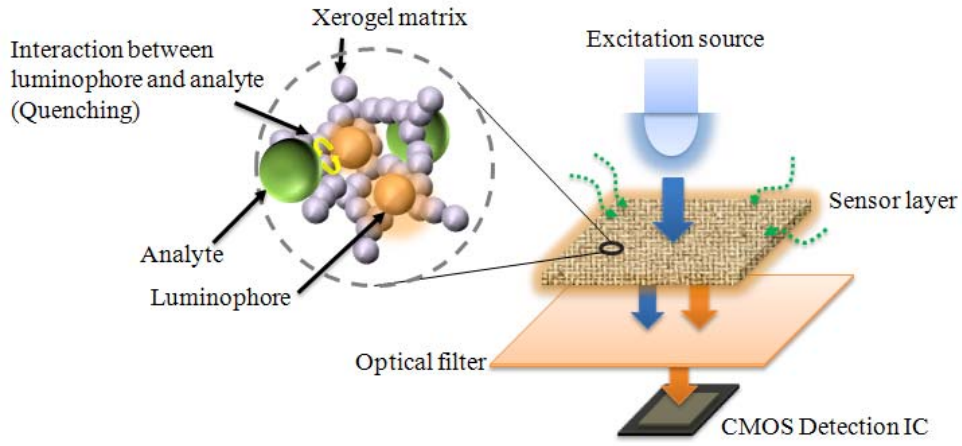

Figure 1.6 General diagram of the CMOS based luminometric sensor system

proposed to enhance the system sensitivity and novel CMOS based luminometric sensor system prototypes are proposed to expand the system functionality. The works are intensively discussed through Chapter 2 to Chapter 4.

1.4 ELECTROCHEMICAL BACTERIA SENSOR SYSTEM

As mentioned before, the optical sensor system discussed above has the drawback of requiring optical-electrical transducer, extra optical components (filter, lens, optical fiber, etc.) and more system integration effort, while electrochemical sensor system such as Clark Electrodes doesn't require these extra efforts. It is the vital drawback of consuming oxygen by many electrochemical sensors that makes them unsuitable for oxygen detection in biomedical applications. However, in many turbid fluidic samples, electrochemical sensors are always more preferable than optical sensors. Also, electrochemical sensors offer direct interface with the signal processing modules and monolithic system integration of electrochemical sensor system is relatively easy and straightforward. In this section an electrochemical sensor system for bacteria detection is introduced. The work is presented and discussed in detail in Chapter 5.

1.4.1 BACTERIA SENSOR SYSTEM

Bacterial biosensors are very important instruments for bacterial population count and pathogenic bacteria detection in many fields such as food industry, drugs discovery, clinical diagnostics and public health security [75]. Current gold standard techniques for these bacteria detections include microscopy, cell culture, plaque forming assays, ELISA (Enzyme Linked Immunosorbent Assay), and PCR (Polymerase Chain Reaction) [76-80]. These microbiological based methods are reliable and accurate but they have drawbacks of involving many steps of pre-enrichment, reactions with antigen-antibody or

manipulation of DNA which is time consuming and require extensive biological skills. This drawback is inconvenient for many applications particularly for on-site food safety and point-of-care diagnostics. Most of the commercial equipments employing these microbiological methods such as BacT/ALERT® 3D (BioMerieux, Inc.), BacTrac® (Sy-Lab, Inc.), RABIT® (Don Whitley Scientific Ltd.) and Malthus® Microbial Detection System (Malthus Diagnostics, Inc.) [81-84] are expensive and large bulky table top size instruments which further limits their widespread use. To address these issues of the conventional methods, many bacteria detection microsystems employing optical, mechanical and electrochemical principles are proposed for rapid, portable and low cost bacteria detection using MEMS [85-86], CMOS [87-89] and microfluidics [90-91] technologies. The general structure and classification of these systems are shown in Figure 1.7.

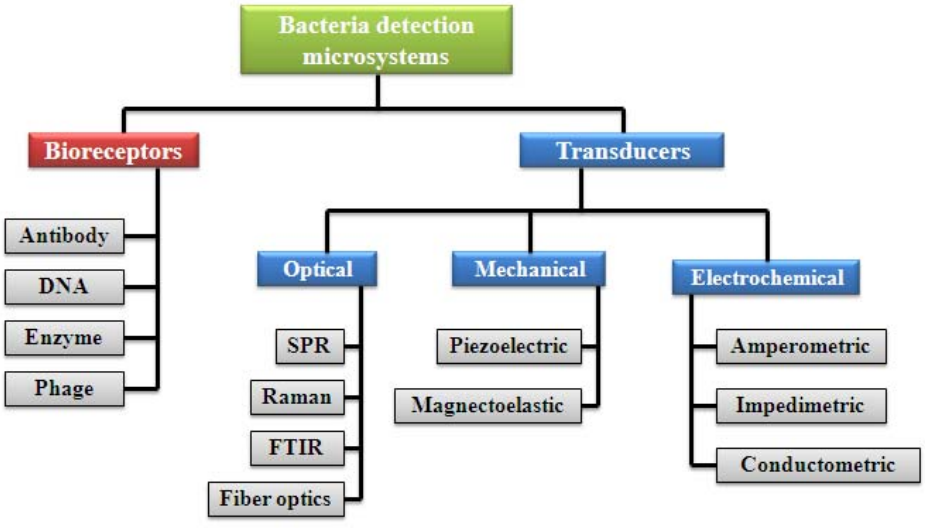

Figure 1.7 General structure and classification of bacterial detection microsystems (SPR: Surface Plasmon Resonance, FTIR: Fourier Transform Infrared)

There are two essential components in a bacterial sensor microsystem: bioreceptor and transducer [80]. The bioreceptor functions as the 'sensor' in Figure 1.1 which is the recognition element specific to the target bacteria of interest. Many biological entities are found useful as bioreceptors such as antibodies [76, 92-97], enzymes [98-99], DNA [100] and bacteriophages (or phages in short) [101-104]. Among these entities, bacteriophages are considered as the most promising because of their extremely high specificity, long-term survivability, low cost, ability to reproduce quickly in suitable hosts and potential to be excellent vehicles for therapeutics of bacterial diseases [105]. There are also different transducer types as shown in Figure 1.7: optical, mechanical and electrochemical. Generally speaking, electrochemical methods are more preferable to other methods particular in sensor microsystems because they allow monolithic integration with the back-end signal processing electronics, are easy to implement, can be mass-produced, and function with turbid samples. There are mainly three types of electrochemical sensing methods: amperometric, impedimetric, and conductometric [80].

An amperometric sensor system monitors the charges generated during the biochemical reactions between the analyte and the receptor at a fixed applied voltage potential [106-107]. Amperometric method is not suitable for the bacteriophage based bacteria detection since there is no biochemical reaction involved and there is no electrical charge generated. Impedimetric method is a popular method in many biological applications [108-109]. It offers real time label free detection by monitoring the capacitance, resistance and inductance information in the analyte solution at different frequencies. However, the complexity of impedimetric system implementation in CMOS makes it unsuitable for portable and low cost applications. An alternative to the impedimetric method is the conductometric method [84, 96, 110-111]. It only measures the resistance of the analyte solution between two electrodes and in some applications

this resistance information is sufficient to interpret biological events. The conductometric analysis can be done with DC stimulation and hence the circuitry is simpler to implement than impedimetric circuitry.

Within the work of this dissertation, bacteriophage is used as the bioreceptor and conductometric method is used as the transduction mechanism.

1.4.2 Bacteriophage and Conductometric Method

The utilization of bacteriophages as bioreceptors for specific bacteria detection has been studied for many years [102, 113-114]. Phages are nanoscale viruses that recognize specific bacteria with extreme selectivity to which they bind and inject their genetic material. Such injection allows replication of the phage and release of a new phage generation while killing the bacteria. Phages are ubiquitous in nature, have long-term survivability, are harmless to humans, and can be easily produced on a commercial scale

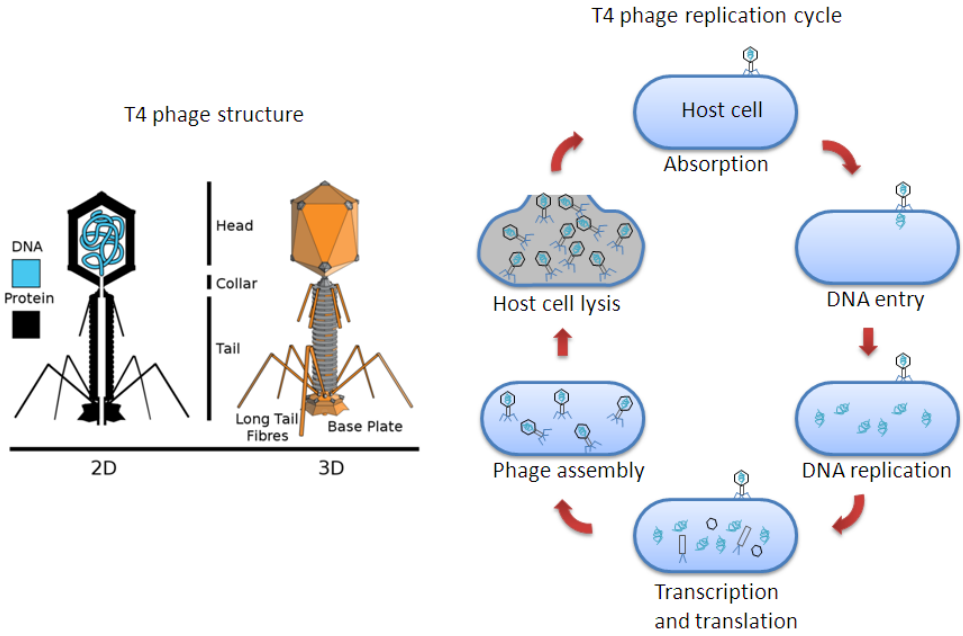

Figure 1.8 Typical structure and replication cycle of T4 phage [112]

in bio-fermentors [105]. The most well studied phage is the enterobacteria phage T4 (also called as coliphage T4) [115-116]. This T4 phage can recognize and lysis bacteria *Escherichia coli*(*E. coli*) cell by replicating itself within *E. coli* cell during the bacteria's exponential growth after capturing *E. coli* cell and injecting its DNA genome into the cell. The structure of the T4 phage and the replication cycle of the phage infecting bacteria cell is illustrated in Figure 1.8. The T4 phage essentially consists of a capsid (head), a contractile tail and six long tail fibers. The DNA of the phage resides in the capsid, the contractile tail can penetrate cell membrane and the six long tail fibers can recognize their host receptor with a very high specificity [116]. To start a phage infection, the fibers recognize particular membrane proteins of the host bacteria cell and adsorb the phage to the surface of the bacteria. After that, the contractile tail penetrates the bacterial membrane and injects the phage DNA into the bacteria cell. Once the phage DNA is injected, the host cell's normal synthesis of proteins and nucleic acids is disrupted and it is forced to manufacture phage products instead (phage's DNA and structural/non structural protein). After replication of these phage products, one copy of each is put in to assemble new phages and at the end of the cycle, the infected bacteria cell membrane is lysised (killed) by these newly produced phages. It is estimated during a single phage replication cycle one infected bacterium can generate 100 to 150 new phages [116] and these new phages are able to again infect other bacterial cells.

The electrical properties of a bacterial cell have been studied for many years [109, 117-118]. It was reported that the resistance coefficient of a bacteria membrane ranges from 10^2 and 10^5 $\Omega \cdot cm^2$ [109] which is much more insulating than the regular bacteria culture media (i.e. Luria-Bertani (LB) media). Based on this resistance difference, the bacteria concentration and interaction with phages can be detected through measuring the conductivity of the sample. This concept is illustrated in Figure 1.9 where bacteria sample

information can be interpreted based on the resistance characteristics of different samples or at different growth stages of the same sample. The bacteria detection system presented in this thesis is based on bacteriophage and CMOS conductometric IC and it is the first research work of integrating CMOS conductometric circuit and bacteriophage in a system to monitor the bacterial activity.

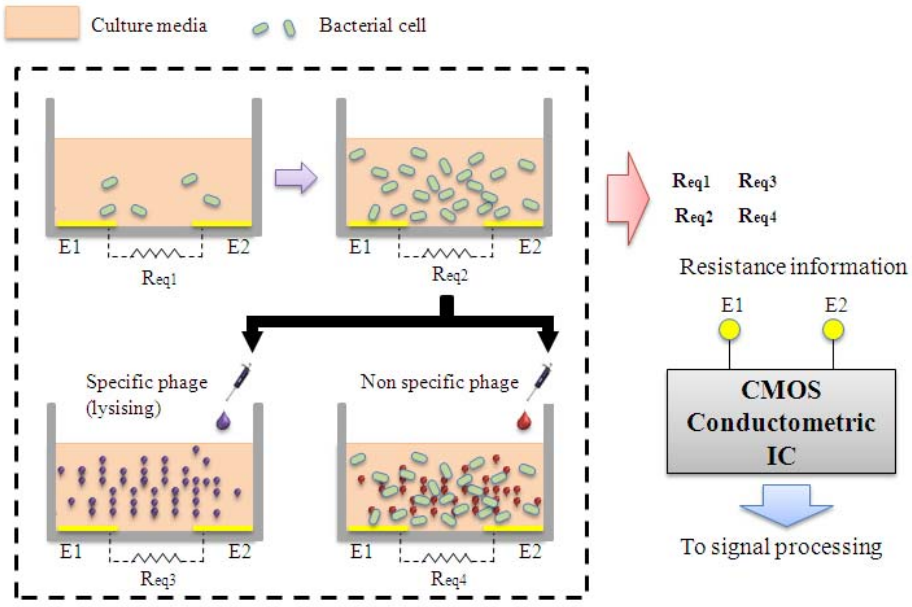

Figure 1.9 Conceptional diagram of the conductometric method for bacteria detection

1.5 DISSERTATION OBJECTIVES AND ORGANIZATION

The major objective of the work presented in this dissertation is to develop novel CMOS based integrated sensor microsystems for various biochemical applications. As introduced before, two types of CMOS based sensor systems are presented in this dissertation: CMOS based luminometric oxygen sensor systems and CMOS based conductometric bacteria sensor system.

Through Chapter 2 to Chapter 4, three CMOS based luminometric sensor microsystems are presented using different detection principles and custom designed CMOS ICs to enhance the performance of the existing luminometric sensor systems. A proof of the concept of luminescence microsensor imaging using CMOS imager is implemented. Finally, experimental feasibility of direct life-time measurement of luminescence is studied.

Chapter 2 presents a fully functional oxygen sensor microsystem using xerogel based oxygen sensor and CMOS detection circuit employing a novel circuit technique to enhance the detection sensitivity of the sensor system. The chapter provides the design and implementation of the CMOS phase luminometric integrated circuit, the fabrication of the xerogel based oxygen sensor, the theoretical analyzing of the novel circuit and the experimental results that depict the sensitivity enhancement made by this circuit.

Chapter 3 focuses on the luminescence multi-sensor systems using xerogel based oxygen sensor array and custom designed CMOS imagers. The chapter gives the design and implementation of a low power CMOS imager. A xerogel based oxygen sensor array is presented in this chapter for the experiment of CMOS imager based multi-sensor system. Optical and electrical system experiment results are given in this chapter to demonstrate the performance and functionality of the proposed multi-sensor system.

Chapter 4 concentrates on the exploration of direct life-time measurement of the fluorescence. In this chapter, design and implementation of CMOS IC are described targeting the direct measurement of excited-state luminescence lifetimes. Simulation and experiment results are present to analyze the hurdles in the direct life time measurement.

For the CMOS based conductometric bacteria sensor system, the work presented in this dissertation is the first research work integrating CMOS conductometric IC and bacteriophages to monitor bacterial activity. This work illustrated the feasibility of this novel system to be used for bacteria detection and monitoring. Chapter 5 presents the design and implementation of the novel bacteria sensor system based on CMOS conductometric IC and bacteriophage. Design considerations for the CMOS ICs are intensively discussed for this specific biological application. The biological background specifically employed in the experiments of this chapter is also introduced. At the last of the chapter, the functionality of this bacteria sensor system is demonstrated by the experimental results and intensive discussion is given.

Finally, chapter 6 provides a summary of this dissertation and concludes with possible future developments of these CMOS based biochemical sensor microsystems.

CHAPTER 2 CMOS PHACE LUMINOMETRIC SENSOR MICROSYSTEM

As described in the Chapter 1, oxygen is an important parameter in many applications such as monitoring blood oxygen demand, process control in food/beverage manufacturing, waste water treatment, and patient respiratory systems. Fluorescence or luminescence based oxygen sensors have several advantages including fast response, they do not consume oxygen, and they require no additional reagents [119]. The basic luminescence sensor operation involves exciting the sensor materials with a lower wavelength optical source and monitoring the excited state emission response from the sensor materials at a higher wavelength. More than often, these sensors are based on measurement of the luminescence intensity or lifetimes of specific luminophores that are immobilized within a variety of thin films (sol-gels, porous polymers) that are used to reliably house the luminophores during the sensor operation [120-121].

In luminometric oxygen sensor system lifetime based sensors are more preferable than intensity based sensors as they incorporate (a) minimal susceptibility to light source (excitation) and detector drift, (b) insensitivity to changes in optical path, and (c) insensitivity to drift due to luminophore degradation and/or leaching [122]. However, the direct measurement of the excited-state lifetimes can necessitate elaborate signal detection and processing instrumentation when performed in the time-domain because the lifetimes are relatively short. Phase luminometry is an alternative to time-domain methods that is simpler and requires less effort in the development of the signal detection

and processing instrumentation [123]. In this approach, the sample is excited with sinusoidal modulated light and the phase shift between the excitation and the luminescence is measured which is directly related to excited state luminescence lifetimes of the luminophores.

The oxygen sensor described here is based on encapsulating the luminophore tris(4,7-diphenyl-1,10-phenanthroline)ruthenium(II) $[Ru(dpp)_3]^{2+}$, well known to be responsive to gaseous oxygen, in the xerogel matrices. Assuming all the luminophore molecules in the xerogel-thin-film are equally accessible to the O_2 molecules, Stern-Volmer equation is rewritten here again as in Equation 2.1 describes the relationship between O_2 concentration and luminophore quenching by O_2, where I_0 and τ_0 are the luminescence intensity or lifetime in the absence of O_2 respectively, I and τ are intensity or lifetime in the presence of O_2 respectively, *Ksv* is the Stern-Volmer constant, k_q is the bimolecular quenching constant and $[O_2]$ is the fractional gaseous O_2 concentration [64]. The sensor system demonstrated in this chapter is based on the measurement of lifetime which is presented as phase shift θ in the frequency domain between the reference (excitation) signal and resulting luminescence signal as described in Equation 2.2 [64]. Here, the luminophore is excited by sinusoidal modulated light source with a frequency *f*. The luminescence is at the same frequency but is phase shifted by θ. The phase shift is dependent on the excited state lifetime (τ) as shown in Equation 2.2. Based on Equation 2.1 and Equation 2.2, O_2 concentration can be obtained by measuring the phase shift θ. From Equation 2.1, the sensitivity of the sensing element (K_{SV}) is dependent on k_q and τ_0. Also, k_q depends on the quencher (O_2) solubility and diffusion coefficients within the xerogels.

$$\frac{I_0}{I} = \frac{\tau_0}{\tau} = 1 + K_{sv}[O_2] = 1 + K_q \tau_0 [O_2] \qquad (2.1)$$

$$\tan(\theta) = (2\pi f) \cdot \tau \qquad (2.2)$$

Xerogel host materials with different K_q values can be fabricated to develop a suite of sensing elements with different sensitivities to a particular target analyte while using the same luminophore [124]. In addition, different luminophores (e.g., $[Ru(dpp)_3]^{2+}$, PtOEP, $[Ru(bpy)_3]^{2+}$) can also be encapsulated in the same xerogel materials and each shows a different sensitivity to O_2 [125]. In the current work we employ a CMOS IC for signal detection and processing and using which we demonstrate, for the first time, how certain signal processing techniques can be utilized to dynamically tune and/or improve the sensor sensitivity while using any single-type of luminophore encapsulated in particular xerogels. This work has good implications to improve the signal to noise ratios, to develop optical sensors where high sensitivity is required for specific concentrations of the target analyte, and to incorporate "smartness" in optical chemical sensors. The developed sensors work over the full range of 0-100% O_2 concentration with a response time of less than 1 second.

2.1 CMOS SENSOR SYSTEM DESCRIPTION

Davenport et al. [67] first reported the integration of CMOS ICs for signal detection and processing and xerogel sensor materials for luminescence intensity based sensors. Later, Chodavarapu et al. [41] reported the first demonstration of CMOS based phase luminometric oxygen sensors system. Chodavarapu et al. [126] also showed more recent developments of CMOS luminescence based multi-sensor system with xerogel materials using a micro-LED array as the excitation source. Figure 2.1 shows the functional

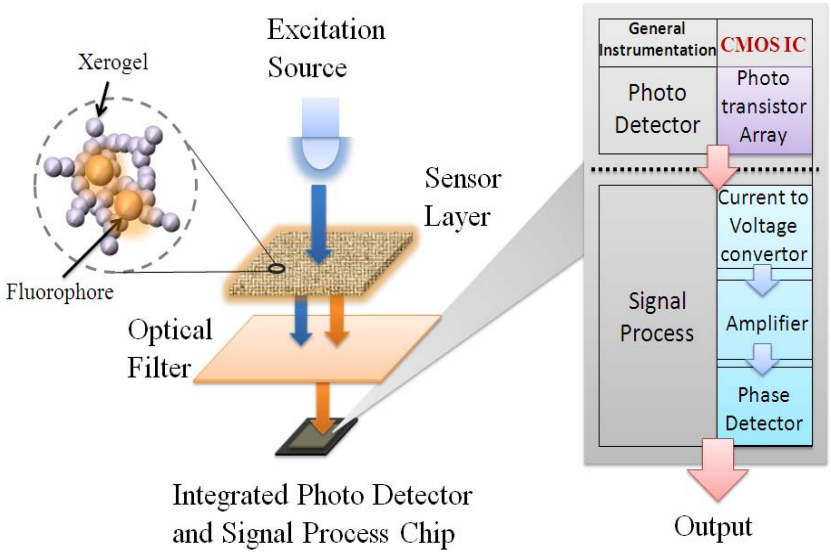

Figure 2.1 Functional components of the integrated sensor system

components of the CMOS integrated sensor system and its functionality is similar to our previously reported work [41]. The system uses a diode laser source (λ_{peak} = 445nm) which is sinusoidal modulated and excites the xerogel sensor materials. The resulting optical signals are passed through a long pass optical filter to remove the excitation signals and allow the luminescence signals (λ_{peak} = 600nm) to impinge on the CMOS IC.

Figure 2.2 shows the schematic block diagram of the CMOS IC. The IC essentially consists of four blocks, (i) phototransistor array, (ii) current to voltage converter, (iii) amplifier block, and (iv) phase detector. The 16x16 array of high-sensitive phototransistors converts the impinged optical signals into electrical current signals and sends the signals to an operational amplifier (op-amp) based circuit that acts as a current-to-voltage converter. The following voltage signals are then amplified by another op-amp based circuit and finally sent to a NXOR based phase detector. The phase detector provide a DC voltage proportional to the phase shift between the detected optical signal and a fixed reference sinusoidal signal obtained from a standard function generator. We

describe a new non-linear phase detector that achieves tunable signal sensitivity (volts/degree phase-shift) for the sensor system. Figure 2.3 shows the microphotograph of the fabricated 2.2mmx2.2mm CMOS IC in AMI 1.5µm process available through MOSIS (www.mosis.org).

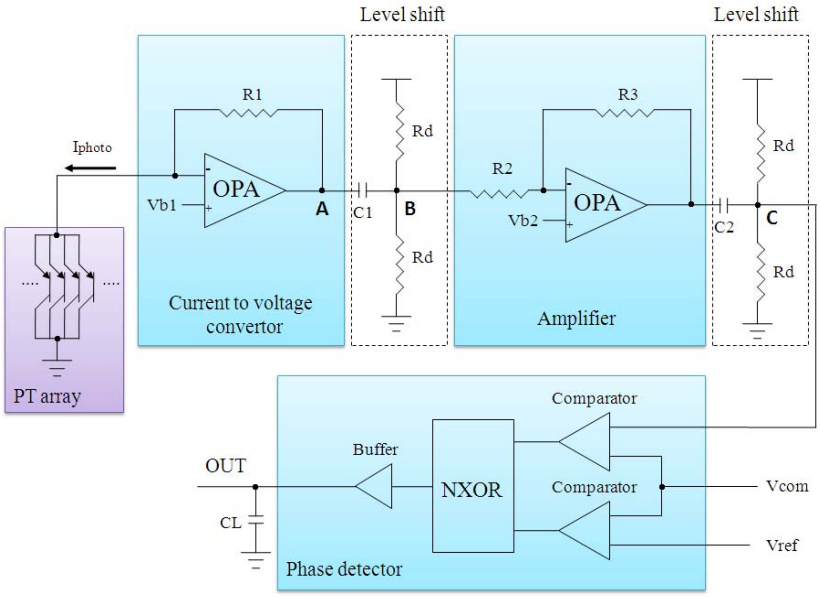

Figure 2.2 Schematic block diagram of the CMOS IC

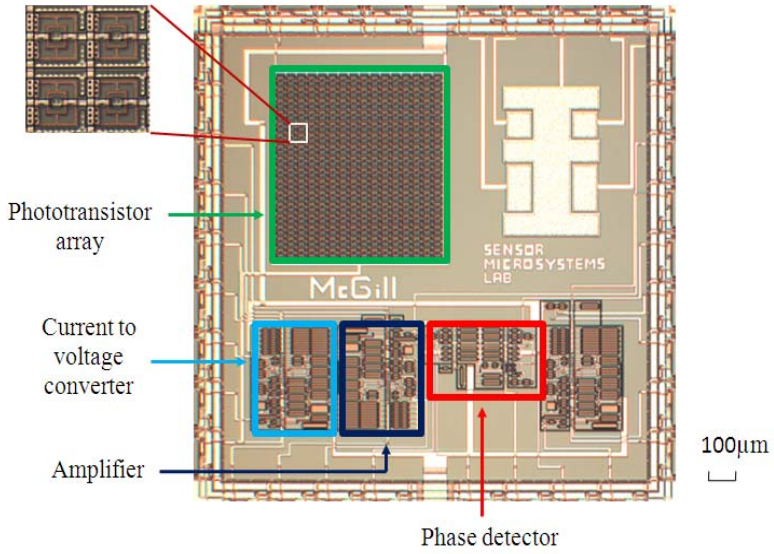

Figure 2.3 Microphotograph of CMOS IC for phase luminometric studies

2.2 CMOS LUMINOMECTRIC IC DESIGN

2.2.1 PHOTOTRANSISTOR ARRAY

The IC consists of a high-gain 16x16 phototransistors array. The structure of phototransistor pixel is similar to a bipolar junction transistor and is formed by p-active (emitter)/n-well (base)/p-substrate (collector). We previously conducted several studies to determine that the above phototransistor has one of the highest responsivity (electrical current output/optical power input) of the photodetectors available in the standard CMOS process and particularly in the visible region of the electromagnetic spectrum [41, 67]. This vertical phototransistor can produce currents that are at least 100 times larger comparing to a comparable sized photodiode. Figure 2.4 shows the microphotograph of a single 43.5µm x 46.5µm phototransistor pixel. The polysilicon grid shown in Figure 2.4 covers the n-well (base) to form a ring around the p-substrate contact and set to the highest potential (V_{DD}) to increase the depletion region where the generated charge carriers can be easily swept to p-active region. However, the bandwidth of operation for

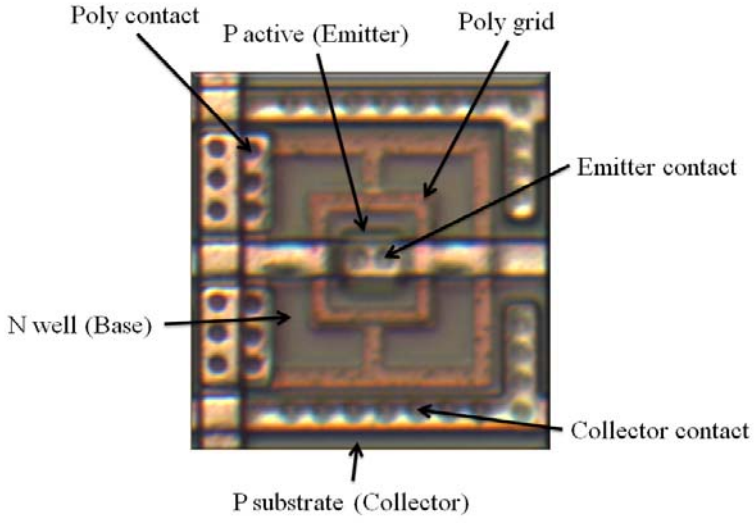

Figure 2.4 Microphotograph of the high-gain phototransistor

the phototransistor is limited to few hundred kilohertz which is sufficient for operation with many luminophores whose excited state lifetimes are longer than several hundred nanoseconds.

2.2.2 CURRENT-TO-VOLTAGE CONVERTER (IVC) AND REGULATED GAIN AMPLIFIER (RGA)

The IVC includes one Trans-Impedance Amplifier (TIA) followed by a voltage level shifter [46]. The TIA is a high-gain rail-to-rail folded-cascode op-amp and one external feedback resistor R_1 (2MΩ) to regulate the conversion gain. The input to TIA is the I_{photo} which is generated by the phototransistor array due to the detected luminescence signals. The output of the IVC includes both a DC component I_{dc} which is caused by circuit biasing conditions and AC component I_{ac}. Here, we are only interested in the AC component which contains the phase information of the sinusoidal modulated luminescence signals. The output of the IVC is amplified by the RGA which is identical to the high-gain rail-to-rail folded-cascode op-amp used for the IVC. The gain of the amplifier is regulated using two external resistors R_2 (100kΩ) and R_3 (1MΩ) to 10V/V. Figure 2.5 shows the schematic of the op-amp used in IVC and RGA.

Predicting the exact value of DC voltage level after each circuit stage is difficult, given the varying luminescence intensity levels and different circuit biasing in each block, and hence its value is reset to the known DC level of 1/2 V_{DD} between each circuit block using a high-pass voltage divider. The first level shifter consists of capacitor C_1 and two identical resistors R_d. The second level shifter consists of capacitor C_2 and two identical resistors R_d. Hence from Figure 2.2, the voltage at nodes A, B and C can be expressed as Equations 2.3, 2.4 and 2.5 respectively.

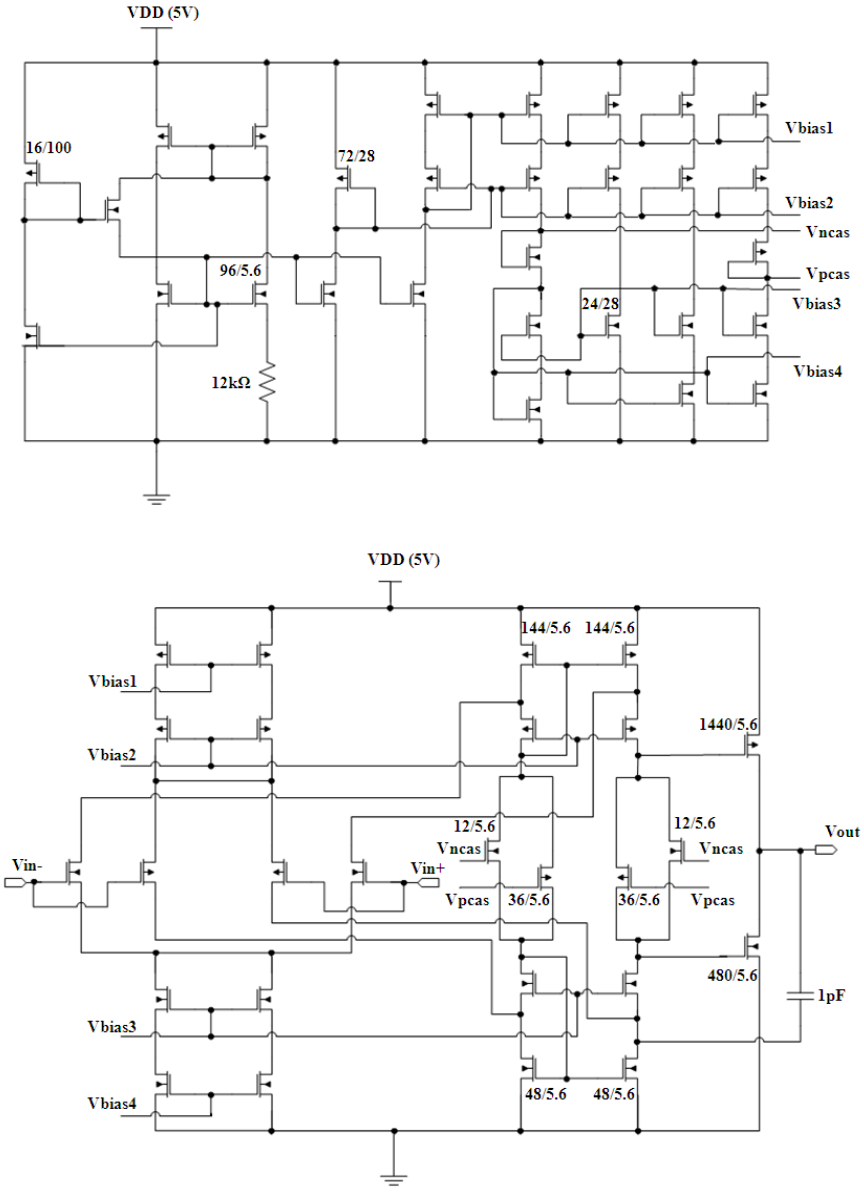

Figure 2.5 Schematic of high-gain high-swing rail-to-rail folded-cascode op-amp used in IVC (W/L ratio of all unlabelled PMOS is 72/5.6, W/L ratio of all unlabelled NMOS is 24/5.6, unit: µm/ µm)

$$V_A = V_{b1} + (I_{dc} + I_{ac}) \cdot R_1 \qquad (2.3)$$

$$V_B = \frac{1}{2} V_{DD} + \frac{I_{ac} \cdot R_1}{\sqrt{1 + \frac{4}{\omega^2 C_1^2 R_d^2}}} \qquad (2.4)$$

$$V_C = \frac{1}{2}V_{DD} + \frac{R_3}{R_2} \cdot \frac{I_{ac} \cdot R_1}{1 + \frac{4}{\omega^2 C_1^{\,2} R_d^{\,2}}} \qquad (2.5)$$

where, ω is the angular frequency (set by the frequency of the modulation of the optical excitation source).

2.2.3 PHASE DETECTOR

The output of the amplifier is directed to a phase detector which gives a DC voltage output related to the phase difference, θ, between a fixed reference sinusoidal signal obtained from the function generator, V_{ref}, and V_C. There are two components in the phase detector (1) comparator and NXOR and (2) low-pass filter stage. Standard wide-swing differential amplifies are used as comparators and a standard digital cell is used for NXOR gate [46]. The output of NXOR is sent to a tuneable low pass filter which enables the phase detector to switch between three operation modes as will be described later. The DC level and amplitude of V_C is decided by Equation 2.5. V_{com} (from Figure 2.2) is set at 1/2 V_{DD}. The output of comparator and NXOR stage is a periodic square-wave signal with a period of 1/2 T and a duty cycle of D expressed as Equation 2.6 in which θ represents the phase difference between V_C and V_{ref} and T represents the period of V_C and V_{ref}.

$$D = 1 - \frac{2\Delta\tau}{T} = 1 - \frac{\theta}{\pi} \qquad (2.6)$$

The output of the NXOR is sent to the low pass filter stage which includes a buffer circuit and a load capacitor C_L as shown in Figure 2.6. The buffer is a standard

differential amplifier configured as a voltage follower with V_{bias} as controlling voltage. In a single pulse duration of V_{in}, there will be a source current I_1 charging the load capacitor C_L and in the non-pulse duration, there will be a sink current I_2 discharging C_L. C_L is designed to be relatively large value (1nF) so that the voltage change in V_{out} can be ignorable during charging/discharging cycles. The amount of charges which move into C_L during charging period Q_1 and the amount of charges which move out of C_L during discharging period Q_2 can be estimated using Equation 2.7. We can also relate both charging and discharging currents by Equation 2.8.

$$Q_1 = \int_0^{\tau} I_1 dt = I_1 \cdot \tau \qquad \text{(a)}$$

$$Q_2 = \int_{\tau}^{\frac{1}{2}T} I_2 dt = I_2 \cdot (\frac{1}{2}T - \tau) \qquad \text{(b)}$$

-------- (2.7)

$$I_1 \cdot (\frac{1}{2}T - \tau) = I_2 \cdot \tau \qquad (2.8)$$

The low pass filter is used to translate the phase difference θ into a DC voltage V_{out}. I_1 and I_2 expressed in Equation 2.8 are both related to V_{out}. By solving Equation 2.8, V_{out} can be expressed as a function of θ. Since I_1 and I_2 will change with M0 and M4 switching into different operation regions, the discussion of solving Equation 2.8 will be divided into three zones of operation; Zone I: M0 in saturation and M4 in triode; Zone II: M0 in triode and M4 in saturation; Zone III: both M0 and M4 in saturation.

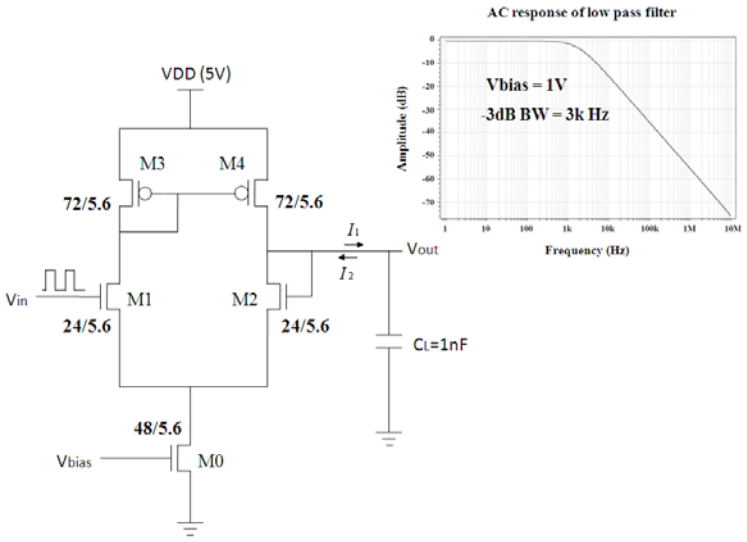

Figure 2.6 Schematic of low-pass filter in phase detector and its low pass characterization

Zone I: From Equation 2.6, when θ is close to 0 or D close to 1 which means V_{out} is close to V_{DD}, M0 goes into saturation while M4 stays in the triode region. I1 and I2 are expressed as equation 2.9, where μ_p and μ_n are the hole and electron mobility; C_{ox} is unit gate capacitance; V_{tp} and V_{tn} are threshold voltages; V_p is the gate voltage of M4; λ_p and λ_n are channel length modulation factors of PMOS and NMOS respectively. V_{out} and the derivative of V_{out} with respect to θ and can be estimated as Equation 2.10 and Equation 2.11. In this zone, S is estimated at $1/\pi$ since δ and γ can be approximated to be on the same order of value.

$$I_1 = \mu_p C_{ox} \frac{W_4}{L_4} (V_{DD} - V_p + V_{tp})(V_{DD} - V_{out}) = \gamma (V_{DD} - V_{out}) \quad \text{(a)}$$

$$I_2 = \frac{1}{2} \mu_p C_{ox} \frac{W_2}{L_2} (V_{bias} - V_{tn})^2 (1 + \lambda_n V_{out}) = \delta (1 + \lambda_n V_{out}) \quad \text{(b)}$$

$$\gamma = \mu_p C_{ox} \frac{W_4}{L_4} (V_{DD} - V_p + V_{tp}) \quad \text{(c)}$$

$$\delta = \frac{1}{2}\mu_p C_{ox}\frac{W_2}{L_2}(V_{bias} - V_{tn})^2 \quad \text{(d)}$$

-------- (2.9)

$$Vout = V_{DD} - \frac{\delta\theta}{\gamma(\pi - \theta)} \quad (2.10)$$

$$S = \frac{\partial Vout}{\partial\theta} \approx -\frac{\delta}{\gamma\pi} \quad (2.11)$$

Zone II: when θ is close to π or D is close to 0 which means V_{out} is near GND, M0 goes into triode region while M4 stays in the saturation. I_1 and I_2 can be expressed as Equation 2.12. Replacing I_1 and I_2 in Equation 2.8, V_{out} and the derivative of V_{out} with respect to θ can be estimated as Equation 2.13 and Equation 2.14. Since α and β are in the same order, resolution S in zone II can be estimated as 1/π.

$$I_1 = \frac{1}{2}\mu_p C_{ox}\frac{W_4}{L_4}(V_{DD} - V_p + V_{tp})^2[1 + \lambda_p(V_{DD} - V_{out})] = \alpha\ [1 + \lambda_p(V_{DD} - V_{out})] \quad \text{(a)}$$

$$I_2 = \mu_n C_{ox}\frac{W_2}{L_2}(V_{bias} - V_{tn})\cdot V_{out} = \beta\cdot V_{out} \quad \text{(b)}$$

$$\alpha = \frac{1}{2}\mu_p C_{ox}\frac{W_4}{L_4}(V_{DD} - V_p + V_{tp})^2 \quad \text{(c)}$$

$$\beta = \mu_n C_{ox}\frac{W_2}{L_2} \quad \text{(d)}$$

------- (2.12)

$$Vout = \frac{\alpha(1 + \lambda_p V_{DD})}{\frac{\beta\pi}{\pi - \theta} + \alpha\lambda_p} \quad (2.13)$$

$$S = \frac{\partial Vout}{\partial\theta} = -\frac{\alpha(1 + \lambda_p V_{DD})}{[\beta + \alpha\lambda_p(\pi - \theta)]^2} \approx -\frac{\alpha}{\beta\pi} \quad (2.14)$$

Zone III: when θ is neither close to π or 0 which means V_{out} is around the middle between V_{DD} and GND, both M0 and M4 stay in the saturation region. I_1, I_2, V_{out} and the derivative of V_{out} with respect to θ are estimated from Equation 2.15 to Equation 2.17. Since α and δ in Equation 2.15 are of same order in value, while λ_n is in the order of 0.01 (1.5μm process), S can be estimated as -100/π which is much larger than the resolution in zone I or II.

$$I_1 = \alpha[1+\lambda_p(V_{DD}-V_{out})] \quad \text{(a)}$$

$$I_2 = \delta(1+\lambda_n V_{out}) \quad \text{(b)}$$

------- (2.15)

$$Vout = \frac{1}{\lambda_n}\cdot[1-\frac{\delta(\lambda_n+\lambda_p)}{\alpha\lambda_p(\frac{\pi}{\theta}-1)+\delta\lambda_n}] \quad (2.16)$$

$$S = \frac{\partial Vout}{\partial\theta} \approx -\frac{4\alpha\delta}{\lambda_n(\alpha+\delta)^2\pi} \quad (2.17)$$

Figure 2.8 shows a measured relationship between phase detector output voltage, V_{out} and detected phase shift, θ, between its two input signals as the V_{out} moves across the Zones I, II, and III. V_{max} and V_{min} voltages are also illustrated which describe the region of maximum sensitivity in the output voltage of the phase detector for the given bias voltage, V_{bias}, and they can be expressed by Equation 2.18. As seen from Equation 2.18 and Figure 2.8, the size of zone III will decreases with increasing Vbias. To achieve a desired size of zone III, the bias voltage, Vbias, should be adjusted properly. The measured response of phase detector under different bias voltage is illustrated in Figure 2.7.

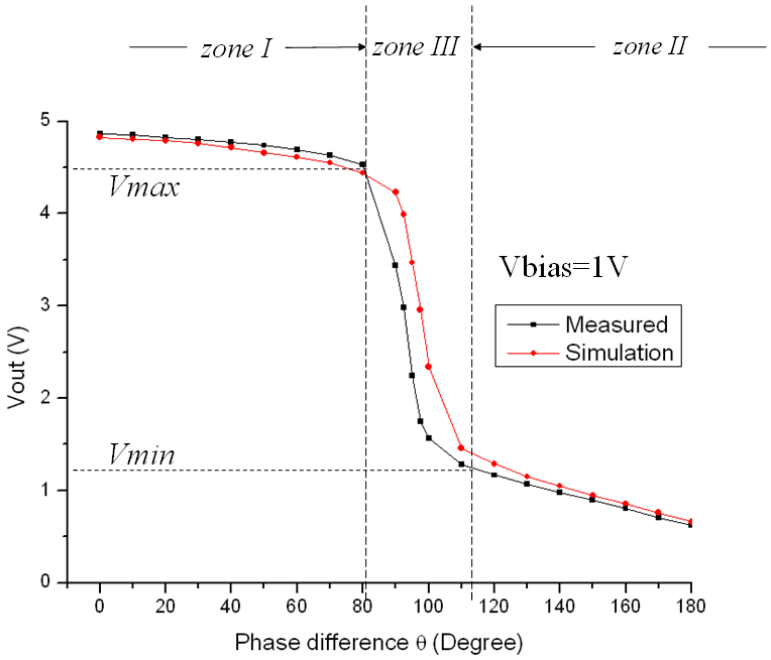

Figure 2.8 Measured response of phase detector when Vbias =1.0 V

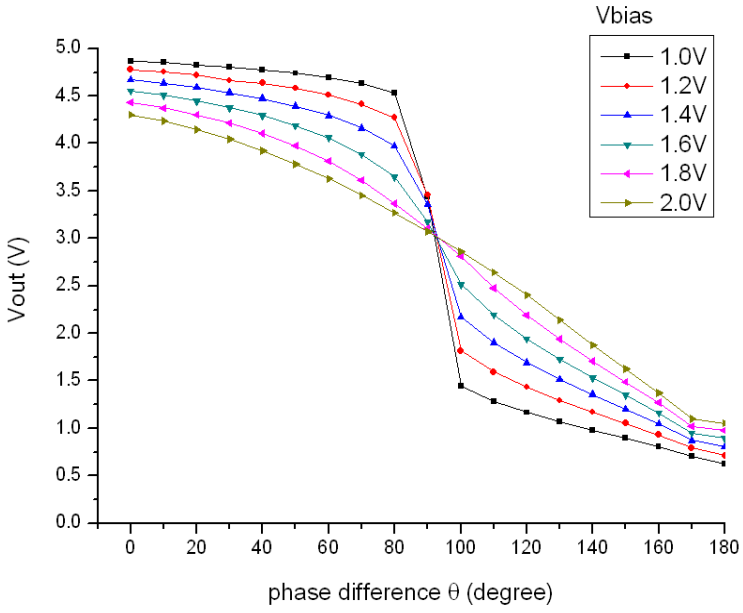

Figure 2.7 Measured response of phase detector for different Vbias

$$V_{\max} = V_{DD} - \sqrt{\frac{\mu_n}{\mu_p}} \cdot (V_{bias} - V_{tn}) \quad \text{(a)}$$

$$V_{\min} = 2V_{bias} - V_{tn} \quad \text{(b)}$$

------- (2.18)

2.3 XEROGEL SENSOR FABRICATION

The following reagents were used: tetraethylorthosilane (TEOS) (United Chemical Technologies), *n*-octyltriethoxysilane (C_8-TEOS) (Gelest, Inc.), HCl (Fisher Scientific), and EtOH (Quantum Chemical). Tris (4,7'-diphenyl-1,10'-phenanthroline)ruthenium(II) chloride pentahydrate ($[Ru(dpp)_3]Cl_2 \cdot 5H_2O$) was purchased from GFS Chemicals. Glass microscope slides were purchased from Fisher Scientific Co..

The sol was prepared by mixing 3.4 mmol of TEOS with 3.4 mmol of C8-TEOS, 21.4 mmol EtOH, and 400 μL of 0.1 M (0.04 mmol) HCl, in the order listed. The sol solution was mixed for 1 hr at room temperature. 100 μL of the sol stock solution was then doped with 20 μL of the $[Ru(dpp)_3]^{2+}$ stock solution (12.5 mM in EtOH). Spin-coated films were prepared by using a micropipette to deliver 50 μL of a particular $[Ru(dpp)_3]^{2+}$-doped sol solution onto the face of a clean glass microscope slide. Xerogel thin films were formed by using a spin coater (2000 rpm, 30 s). Finally, the xerogel films were aged at 80°C for 5 days before experimental testing.

2.4 EXPERIMENTAL RESULTS AND DISCUSSION

The experiment setup for the phase luminescence sensor is shown in Figure 2.9. It consists of a laboratory DC power supply (Instek: GPS-3303) and function generator (Tabor Electronics: WW2572A) to supply the CMOS IC and modulate the laser (λ_{peak}=445nm Coherent: CUBE). The sensor response is measured by CMOS IC as a function of gaseous O_2 concentration. A digital multimeter (Keithley: 2700) is used to read-out the output of IC. The O_2 concentration is varied by changing its relative percentage with respect to gaseous N_2 concentration. The gases are mixed within a custom built flow-meter, consisting of a matched pair of air flow controllers connected to O_2 and N_2 gas cylinders. In operation, the laser excites the film. The resulting optical signal is passed through a long-pass optical filter (Cut-off, λ = 590nm) to remove the excitation signal and allow the luminescence impinge on the CMOS IC. After the optical signal is processed by the IC, the output is a DC voltage value proportional to the phase shift between the signal obtained from the phototransistor and a reference signal obtained

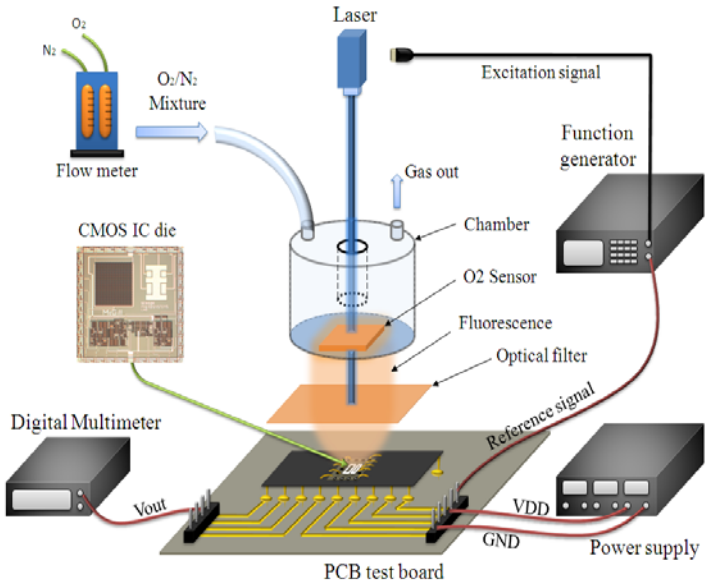

Figure 2.9 Experimental setup for evaluating the CMOS phase luminometic system

from the function generator. The DC voltage value is manually translated to degrees using a preset calibration data for the phase detector as reported in Figure 2.7.

For the CMOS IC, the V_{DD} is set to 5.0V. The excitation sinusoidal modulation frequency is set at 38kHz. Figure 2.10 shows the output of the sensor system with the phase detector tuned to provide a linear response (Vbias, shown in Figure 2.6, is set as 1.7V). The sensor operates in the full scale (0% to 100%) of O_2 concentrations and the system provides an approximately linear change of 350mV (in other words, 3.5mV/%change in O_2 concentration). *θsensor* is caused by the O_2 sensor, which various with the O_2 concentration. *θcircuit* is the phase difference between modulation signal and reference signal, plus the phase shift caused by laser and CMOS circuitry. Figure 2.11 shows the output of our sensor system with the phase detector tuned to provide a nonlinear response (V_{bias} is set as 1.0V). In this configuration, the sensor becomes more sensitive in a particular range of O_2 concentration although the sensor works the full scale of O_2 concentrations (0% to 100%)). The system provides a very high sensitivity between

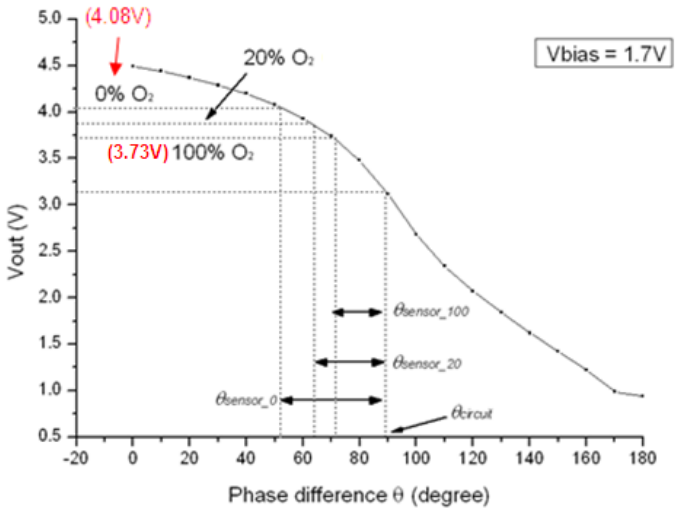

Figure 2.10 Calibration of phase detector with V_{bias}=1.7V

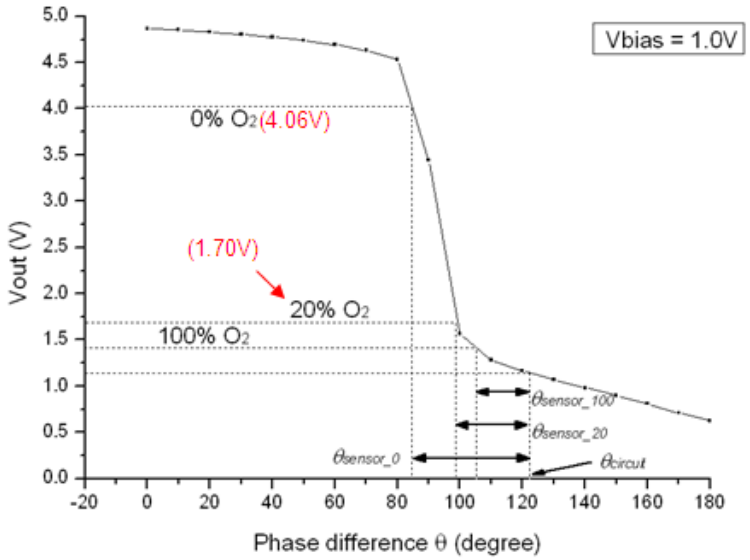

Figure 2.11 Calibration of phase detector with Vbias= 1.0 V

0% and 20% O_2 concentration (particularly useful for biomedical applications) with an output voltage change of 2.36V or 118mV/% change in O_2 concentration. Further, the region of high sensitivity response can be moved to any particular range of O_2 concentration by simply shifting the phase of the reference sinusoidal signal provided to the phase detector.

Figure 2.12 shows the response of the sensor system with the phase detector operating with a non-linear response (Vbias set to 1.0V) and the O_2 concentration repeatedly varied between 0% and 20% in steps of 5% with respect to the N_2 concentration. Using the preset calibration of phase detector shown in Figure 2.11, we can find *θcircuit* and *θsensor* under different O_2 concentration. In the current work the resolution of the sensor system is greatly enhanced to 118mV/degree due to the nonlinear phase detector. Figure 2.13 shows the experimental result when the O_2 concentration is changed repeatedly from 0% to 100% and back to 0%. The sensor shows a reversible and repeatable performance. The total phase shift with O_2 concentration changing from 0% to 100% is 21 degrees

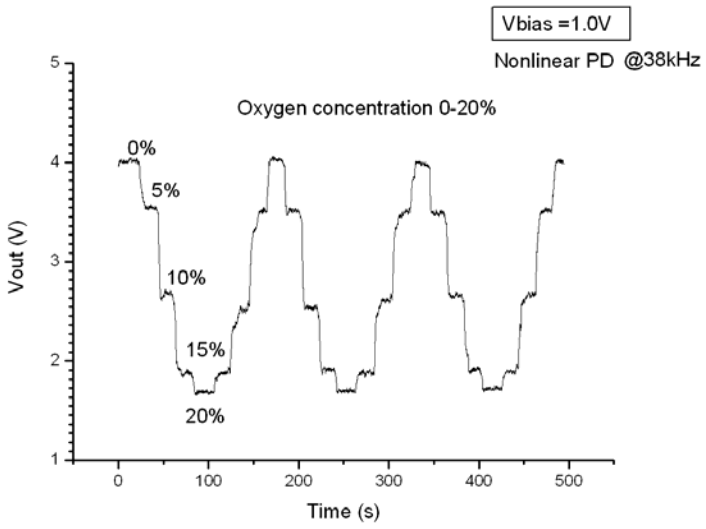

Figure 2.12 Sensor system response with O2 concentration varying from 0% to 20%

operating at 38kHz, which is at the same order as our previous works [41]. However, we notice that the signal sensitivity is significantly enhanced between 0% and 20%. Further, we can notice that the noise level is reduced to less than 1% of the signal change between 0% and 20% O_2 concentrations and thus significantly improves the accuracy of the sensor in that specific range.

In the current work, we used a laser diode as the optical excitation source. This marks a shift from our previous works where we preferred the use of an LED as excitation source towards low power sensors [41, 126]. The GaN blue LED has a "yellow tail" optical response that extends in the wavelength range of the fluorescence from $[Ru(dpp)_3]^{2+}$ [65]. The use of a short-pass filter after the LED to remove longer wavelengths also does not effectively eliminate the yellow tail. Further, the intensity of the yellow response is in many cases significant compared to the luminescence intensity. The frequency of the yellow tail response from the GaN LED is same as the luminescence, hence the phase shift recorded is an intermediate value between the excitation signals and the actual luminescence signals. Further, the optical density of luminescence signals generated from

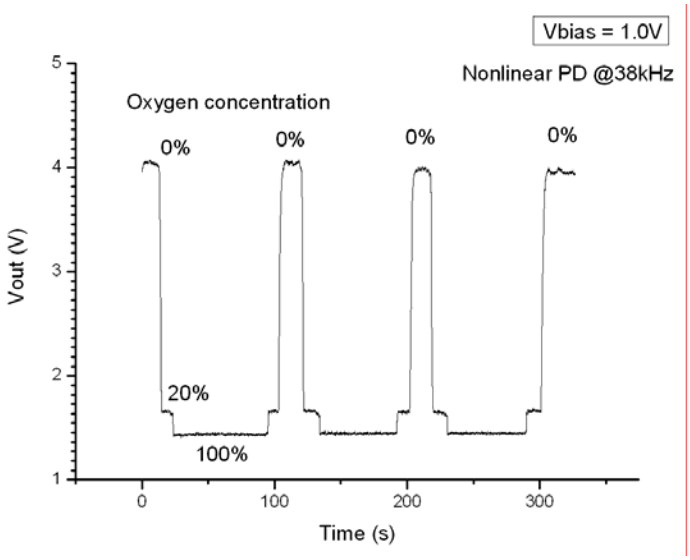

Figure 2.13 Sensor system response with O2 concentration varying from 0% to 100% with employing non-linear response from phase detector

using an LED is low which reduces the signal conversion rate of CMOS photodetectors and thus limits the frequency of modulation to lower tens of kHz. This limitation has a direct influence on the range of lifetimes that can be detected by the sensor system (From Equation 2.2).

In recent times, the availability of reliable, long lasting and affordable GaN laser diodes and VCSELS (Vertical Cavity Surface Emitting Lasers) operating in blue wavelengths creates various possibilities in incorporating them in integrated sensors. We can expect that in near future, they will become much cheaper and low power consuming. More recently, several companies have made available 3V battery powered diode pumped solid state (DPSS) laser emitting at 473nm (Aquarius from Laser Glow Inc.). The developments in blue wavelength solid-state lasers allow us to overcome several issues discussed above in using LED sources. However, these discussions in light sources should not overshadow the main goal of this work which is to implement a CMOS signal

processing circuit technique to dynamically tune and improve the sensitivity in phase luminometry sensors.

2.5 SUMMARY AND CONCLUSION

We presented the design and implementation of a phase luminescence sensor system with improved and tunable detection sensitivity achieved using a CMOS IC and xerogel sensor materials. As a prototype, we demonstrate an oxygen sensor system by encapsulating the luminophore $[Ru(dpp)_3]^{2+}$ in the xerogel matrices. We discussed the behavior of a non-linear phase detector that allows the phase luminescence system to change its detection sensitivity controlled by a single bias voltage. The increase in the detection sensitivity reduces the dynamic range of operation for the sensor. We demonstrated a detection sensitivity of 118mV/%change in O_2 concentration which exceeds the performance shown by previous other similar sensors. This work has good implications to improve the signal to noise ratios and to develop optical sensors where high sensitivity is required for specific concentrations of the target analyte particularly for many biomedical applications. Finally, the works provides opportunity to incorporate "smartness" in future optical chemical sensors by having the ability of variable detection sensitivities with any particular optical recognition element.

CHAPTER 3 CMOS MULTI-SENSOR MICROSYSTEM

Besides making improvement to the luminescence sensor system, another important research direction is the luminescence based multi-sensor platform. In this chapter a multi-sensor platform is presented based on luminescence sensor microarrays and custom designed CMOS imager ICs.

Luminescence based sensor microarrays are becoming increasingly important in many environmental, biological, and health applications [127-128]. These sensor microarrays offer several advantages including fast response, they do not poison sample media, and they require no additional reagents [65]. Microarrays consist of an ordered arrangement of sensor elements that each can be made to sense a specific analyte in any test sample [129]. In the past, different approaches have been used to fabricate optical sensor microarrays including pin [130], ink-jet and screen printing [131-132], and photolithography [133]. Micro-pin printing methods use one or more pins to contact print/spot liquid onto a planar surface (e.g., a microscope slide). Pin-printing allows low cost, accurate, and high throughput immobilization of a variety of recognition materials. In this chapter, we are using the pin-printing methods to fabricate reusable xerogel based sensor arrays [130]. To acquire the luminescence from the sensors array, optical imager is required in the system. Here in this chapter we describe the design and development of a low noise, low power consuming, and high sensitivity CMOS imager to perform the

imaging task. The architecture of the proposed multi-sensor platform is shown in Figure 3.1.

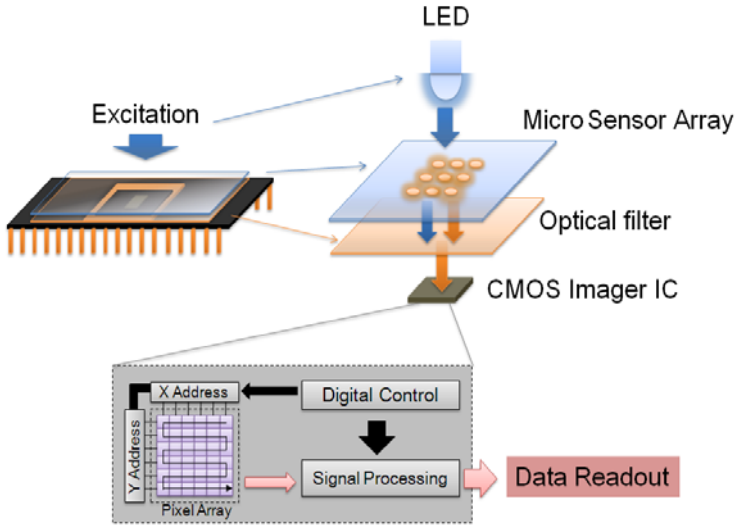

Figure 3.1 Simplified block diagram of the CMOS based multi-sensor system

In the work presented in this chapter, the sensor microarray is designed by co-encapsulating luminophore tris(4,7-diphenyl-1,10- phenanthroline) ruthenium(II) ($[Ru(dpp)_3]^{2+}$) and *tris*(2,2'-bipyridyl) dichlororuthenium(II) hexahydrate ($[Ru(bpy)_3]^{2+}$), both of which are well known to be responsive to gaseous O_2 [64], in the xerogel matrices. Thus, one can write the quencher-dependent response as [134],

$$\begin{aligned} I_0 / I &= [f_1 / (1 + K_{SV1}[Q]) + f_2 / (1 + K_{SV2}[Q])]^{-1} \\ &= [f_1 / (1 + k_q \tau_{0,1}[Q]) + f_2 / (1 + k_q \tau_{0,2}[Q])]^{-1} \end{aligned} \tag{3.1}$$

where, K_{SV1} and K_{SV2} are the Stern-Volmer constants, f_1 and f_2 denote that fraction of the total emission (in the absence of quencher) that arises from luminophore 1 and 2, respectively; $\tau_{0,1}$ and $\tau_{0,2}$ are the excited-state luminescence lifetimes for luminophores 1

and 2, respectively, in the absence of quencher; k_q is the bimolecular quenching constant between the luminophores and the quencher molecule; and I_0 and I are the luminescence intensity in the absence and presence of quencher (O_2), respectively. (Note: In Equation 3.1, we assume that k_q, the bimolecular quenching constant, is luminophore-independent because the luminophores are structurally similar and thus would be distributed similarly within the xerogel host matrix.) Inspection of Equation 3.1 shows that one can continuously tune the sensor response profile (i.e., I_0/I vs. $[O_2]$) within a single analyte-permeable host matrix by creating sensor elements that contain different fractions of luminophore 1 and 2. The luminophores are selected such that they show the same emission spectrum but each shows different τ_0 [134].

3.1 CMOS IMAGER INTEGRATED CIRCUIT

CMOS imager ICs have been used for many luminescence applications, starting with Vo-Dinh et al. [135] who reported a CMOS phototransistor based imager to implement a microsystem for DNA microarrays. Subsequent works were related to DNA microarrays [42, 136], modeling and simulation [137], and excited-state lifetime measurements [74]. Our CMOS imager IC (Figure 3.2) consists of three blocks: (i) active pixel array, (ii)

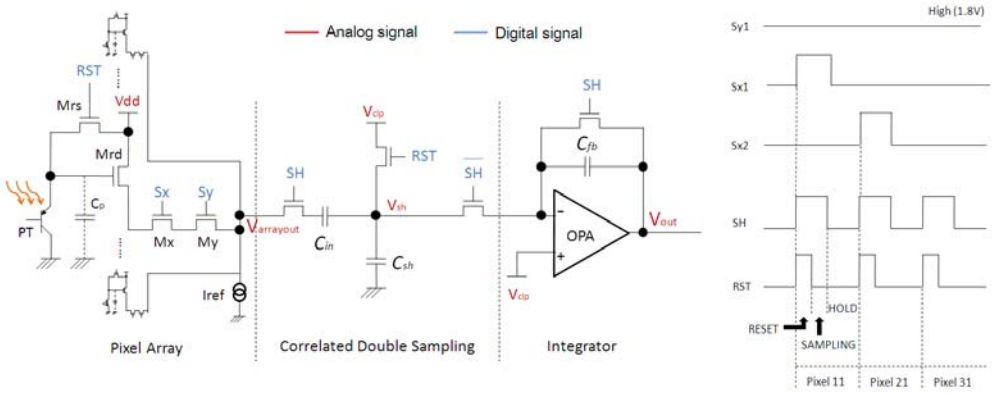

Figure 3.2 Schematic diagram of the CMOS Imager IC and typical waveform of key digital signals

digital control circuit and X-Y address circuit, and (iii) analog signal processing circuit. The imager uses an active pixel sensor (APS) array based on standard circuit designs [138]. To operate the APS array, three digital control signals are required: *RST*, S_x and S_y. The output signal of pixel array is read out serially at $V_{arrayout}$ by the signal processing circuit. The signal processing circuitry mainly includes the correlated doubling sampling (CDS) circuit and integrator circuit. The CDS block is used to minimize the fixed pattern noise (FPN) and the integrator is used to integrate the ramp shaped signal into DC form for serial readout. Three digital signals are needed to operate the signal processing circuit: *RST*, *SH*, and the complementary signal of *SH*. All the required digital signals in the imager IC are generated on-chip by the digital control circuit/X-Y address circuit and are synchronized with the external clock signal, *CLK*. Figure 3.3 shows the microphotograph of the fabricated 1.5mmx1.9mm CMOS imager IC in TSMC 0.18µm-CMOS process available through CMC (www.cmc.ca).

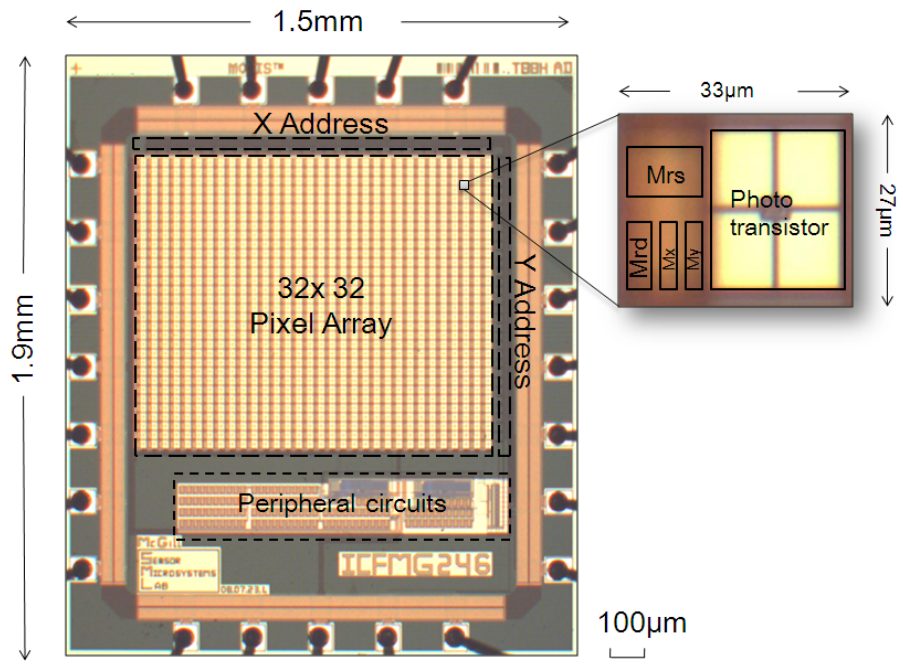

Figure 3.3 Microphotograph of the CMOS imager IC, The inset picture shows a single active pixel sensor (APS)

The CMOS imager IC which forms the essential part of many commercial digital cameras typically consists of an array of individually accessible photosensitive pixels. Our imager IC includes a 32x32 array (1024 elements) of APSs. Each APS pixel uses a vertical p-n-p phototransistor as the photodetector. Phototransistors can produce current levels that are several times larger in comparison to comparably sized photodiodes. The vertical p-n-p phototransistor can only be used in an emitter-follower configuration and it is formed by the p-active (emitter)/n-well (base)/p-substrate (collector) [67]. Each APS element contains the phototransistor and four MOSFETs (M_{rs}, M_{rd}, M_x and M_y) as shown in Figure 3.2. M_{rs} is the reset transistor and M_{rd} acts as a source follower. M_x and M_y are the address transistors that perform the serial pixel readout. The serial readout data is then processed by the signal processing circuit. Typical digital control waveforms of the imager are shown in Figure 3.2.

During the imager operation, there are three periods in a single scan circle: RESET, SAMPLING and HOLD. First, in the RESET period, the signal, RST is activated (1.8V) to charge the emitter terminal of the phototransistor with the impinged optical signals to V_{dd} (1.8V). During SAMPLING period, RST is deactivated (0V) and the signal is sampled through M_x and M_y. The voltage drop between RESET and SAMPLING period is $V_{arrayout}$ which can be calculated according to Equation 3.2, where I_{pt} is the current generated by the phototransistor when excited by the luminescence, T_{sample} is the time of the SAMPLING period, C_{pt} is the parasitic capacitance existing in the phototransistor. Finally, in the HOLD period, the signal is processed by the signal processing circuit while the rest of the pixel array is in idle mode.

$$\Delta V_{arrayout} = \frac{I_{pt} \cdot T_{sample}}{C_{pt}} \qquad (3.2)$$

From Figure 3.3, the size of each active pixel is 33µm by 27µm with a fill factor of 56.1%. The W/L ratios for the transistors in the active pixel are: M_{rs} 0.5/0.18, M_{rd} 4.8/0.5, M_x 4.8/0.5, M_y 4.8/0.5 (all dimensions are in µm). The size of phototransistor is 20µm by 25µm. Based on the TSMC 0.18µm process parameters, the parasitic capacitor C_{pt} can be estimated as 65fF. The typical value of the photocurrent generated by these phototransistors under luminescence is between a few hundred picoamperes and several tens of nanoamperes. As an example, with a sampling frequency of 1k Hz, $\Delta V_{arrayout}$ can be calculated as 384mV when I_{pt}=50pA (using Equation 3.2), and this voltage range can be easily handled by the signal processing circuit.

3.1.1 PERIPHERAL CIRCUITRY

All the required digital signals are generated by the on-chip digital block using an external clock source as reference. The analogue data flow is shown in Figure 3.2. The pixel array serial output is read out at $V_{arrayout}$ using a CDS circuit [138] followed by an integrator circuit. The basic operation of the circuit in Figure 3.2 is as follows: When the signal RST is active (1.8V), a selected pixel enters its RESET period, the voltage in the sample and hold capacitor (C_{sh}) is clamped at V_{clp}. At the same time the integrator is isolated from the CDS circuit and works as a simple voltage follower. The output voltage of the integrator during the RESET period is V_{clp}, no data will be readout. When the RST signal goes low (0V), the current pixel enters the SAMPLING period, the pixel array $V_{arrayout}$ output voltage drops proportional to the incident power of the optical signal (i.e., luminescence). Then, C_{sh} samples the drop in voltage and then the voltage is integrated into a DC value by the integrator circuit. Since CDS only samples the voltage drop and

the DC level of each pixel is isolated by C_{in}, FPN noise which is caused by pixel mismatch can be greatly suppressed. The output voltage of the CDS block, V_{sh}, can be expressed by Equation 3.3. The output voltage V_{out} during the HOLD period can be expressed by Equation 3.4. Substituting the value of ΔV_{pixout} obtained from Equation 3.4 into Equation 3.2, the relationship between V_{out} and I_{pt} can be derived as presented by Equation 3.5. Thus, the sensitivity, S, of CMOS imager IC can be calculated using Equation 3.6.

$$V_{sh} = V_{clp} - \Delta V_{arrayout} \cdot \frac{C_{in}}{C_{in} + C_{sh}} \tag{3.3}$$

$$V_{out} = V_{clp} + \Delta V_{arrayout} \cdot \frac{C_{in}}{C_{in} + C_{sh}} \cdot \frac{C_{sh}}{C_{fb}} \tag{3.4}$$

$$V_{out} = V_{clp} + \frac{C_{in}C_{sh}T_{sample}}{C_{fb}C_{pt}(C_{in} + C_{sh})} \cdot I_{pt} \tag{3.5}$$

$$S = \frac{\Delta V_{out}}{\Delta I_{pt}} = \frac{C_{in}C_{sh}T_{sample}}{C_{fb}C_{pt}(C_{in} + C_{sh})} \tag{3.6}$$

The CDS circuit block consists of three (3) switches and two (2) capacitors, and the integrator consists of one switch, one capacitor and an operational amplifier (op-amp). The op-amp used in the integrator is a high-gain high-swing rail-to-rail folded-cascode amplifier [46]. The capacitor values are as follows: C_{in}=8pF, C_{sh}=2pF and C_{fb}=2pF. With C_{pt}=65fF and T_{sample}=5ms, the detection sensitivity S can be calculated as 6.12V/nA (output voltage/generated photocurrent). For a good output dynamic range, V_{clp} has to be set carefully. As seen from Equation 3.3 and 3.4, V_{clp} can neither be set too high (V_{sh} will get saturated) nor too low (V_{out} will get saturated). The calculated ideal point for V_{clp} is 0.9V for the current configuration (the ratio of C_{sh} to C_{fb} is 1). Finally, considering the

dynamic range of op-amp and mismatch issue of the capacitors, we set V_{clp} at 0.8V to obtain a good output dynamic range.

3.1.2 CMOS IMAGER IC CHARACTERIZATION

In this section we detail the characterization of the CMOS imager IC in terms of: responsivity, FPN noise and dark current. In luminescence monitoring applications the phototransistor (or in general the photodetector device) plays a critical role. From our previous work on the similar structured phototransistor we noticed a high responsivity (Ampere/Watt) over a wide range of the visible wavelength spectrum which is well suited for luminescence sensor applications [41]. For characterizing the current CMOS imager, we used an orange LED (λ_{peak}=595nm) to illuminate the CMOS imager uniformly. This wavelength was chosen because it is near the peak luminescence from our O_2 sensors. An

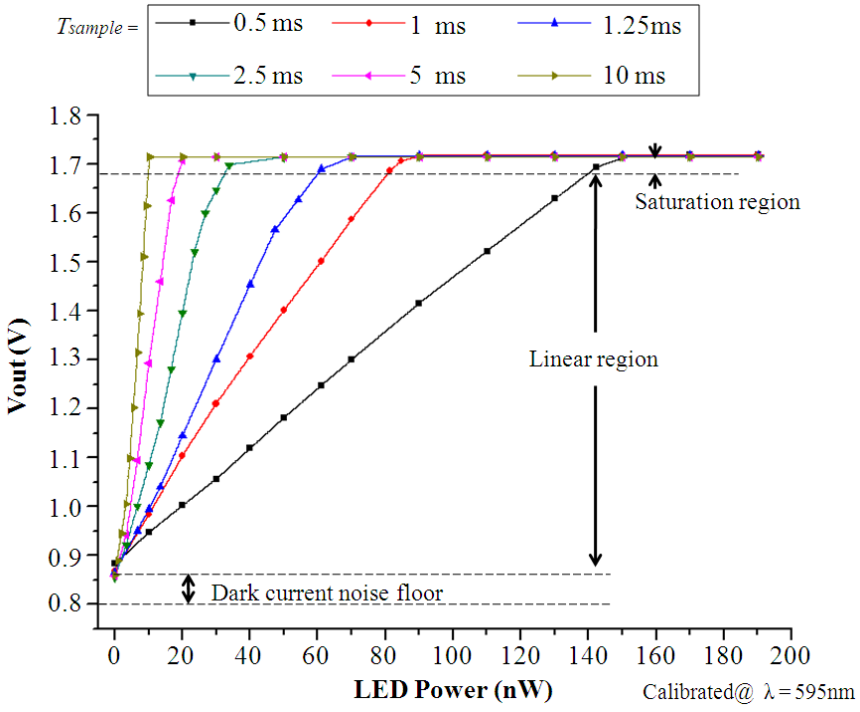

Figure 3.4 Measured relationship between incident power and sampling time *Tsample*

external clock generated by a data acquisition system (National Instruments) is used and its frequency is varied from 50Hz to 1kHz (equivalent to integration or sampling time, T_{sample}, varying from 10ms to 500 μs). Under each sampling time the voltage response of a single pixel is recorded. The LED optical power is measured by a calibrated power meter (Coherent Inc.). Figure 3.4 shows the relationship between incident optical power and voltage response under different sampling/exposure time T_{sample}. Detecting weak luminescence signals requires longer integration or sampling times. We selected 5ms as the sampling time to detect the weak luminescence signals in this work. This sampling time provides a good compromise between achieving high detection sensitivity and acceptable sampling time in this application.

FPN and dark current are two key performance parameters for any CMOS imager. We kept the CMOS imager IC in complete dark conditions at room temperature (25°C) and observed one frame of data (1024 pixels) from the imager IC. The FPN and dark current

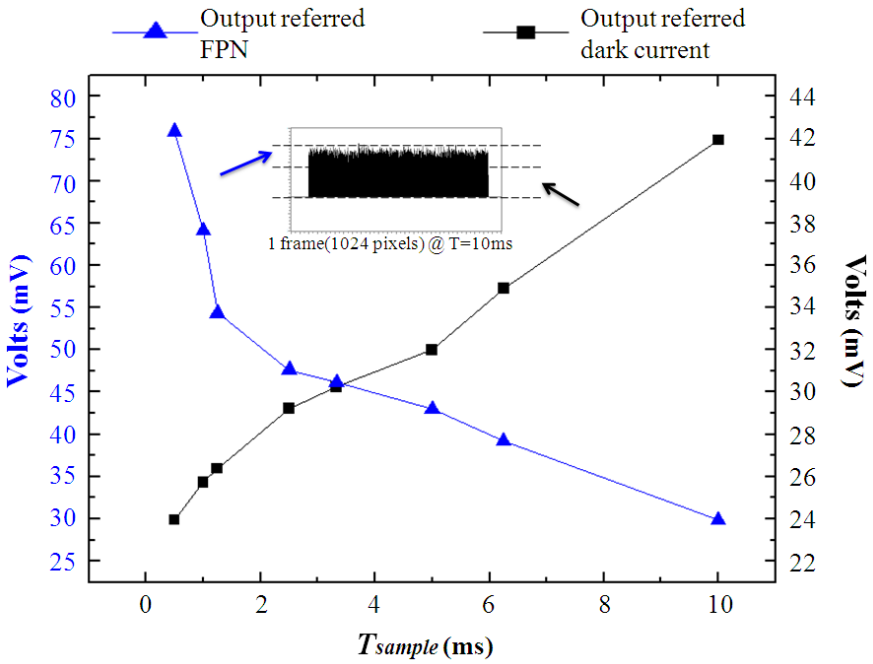

Figure 3.5 Measured relationship between FPN, dark current and sampling time *Tsample*

are recorded as a function of sampling time (0.5ms to 10ms) (Figure 3.5). The FPN shows a non-linear decrease from 77mV to 33mV with sampling time, T_{sample}. We notice that in the high sampling frequency range (low sampling time) the FPN noise profile has a larger slope in comparison to the low sampling frequency range. The output referred dark current shows a proportional increase from 24mV to 42mV with sampling time T_{sample}. We notice that the output referred dark current level is maintained to a low value due to the lower leakage current in the designed phototransistors and due to the lower VDD level (1.8V).

In this work, we also evaluated the effect of temperature on these hybrid xerogel microarrays which has not been studied to date. We did not pursue temperature analysis of the imager circuit *per se* as it has been previously studied and documented and we considered it redundant to be studied here [139-140]. So, the imager was always maintained at room temperature during the experimental measurements.

3.2 PIN-PRINTED XEROGEL SENSOR ARRAY

Reagents: The following reagents were used: tris(4,7'-diphenyl-1,10'-phenathroline) ruthenium(II) chloride ($[Ru(dpp)_3]Cl_2$) and tris(2,2'-bipyridine) ruthenium(II) chloride hexahydrate ($[Ru(bpy)_3]Cl_2 \cdot 6H_2O$) (GFS Chemicals, Inc.); tetraethylorthosilane (TEOS) (Gelest Inc.); *n*-octyltriethoxysilane (C8-TEOS) (Gelest Inc.); HCl (J.T. Baker); and EtOH (Quantum Chemical Corp.). Corning # 2947 microscope slides (Fisher Scientific Co.) were used as the xerogel substrates. All reagents were used as received without further purification. Deionized water was prepared to a specific resistivity of at least 18 MΩ-cm by using a Barnstead NANOpure® II system.

Stock sol preparation: Class II xerogels were produced by preparing a sol composed of TEOS (1.448 mL, 6.5 mmole) and C8-TEOS (2.052 mL, 6.5 mmole), EtOH (2.52 mL, 44 mmole) and HCl (0.8 mL of 0.1 N HCl, 0.08 mmole). This mixture was capped and magnetically stirred under ambient conditions for 1 hour.

Luminophore-doped sol preparation: It proved beneficial to have the sensor elements within the array exhibit nearly equal emission intensities in the absence of quencher. This way, we could record a single image at each O_2 concentration and avoid multiple images at varying integration times and the concomitant backgrounds. Table 3.1 reports the $[Ru(bpy)_3]^{2+}/[Ru(dpp)_3]^{2+}$-doped sol compositions that we prepared to yield the unique response profiles and achieve the aforementioned goal. Stock solution I was prepared by dissolving 187.2 mg of $([Ru(bpy)_3]Cl_2 \cdot 6H_2O$ in ethanol. Stock solution II was prepared by dissolving 58.5 mg $[Ru(dpp)_3]Cl_2$ in ethanol. Luminophore-doped sols in Table 3.1 were prepared by mixing (touch mixer, 1 min) the listed volumes of stock solutions I and II with the hydrolyzed sol. The sols were then stored in the dark without stirring under ambient conditions. Sensor elements were formed from these sols.

Table 3.1
DESCRIPTION OF THREE DIFFERENT SENSORS

Sensor Row	**Volume of sol (mL)**	**Stock solution I (µL)**	**Stock solution II(µL)**
A	1.6	150	250
B	1.6	66	344
C	1.6	26	374

Metal mask: A metal mask is used to improve the contrast for the detected luminescence by reducing the background excitation signal. The mask was fabricated on the microscope slide with sputtered metal layers of titanium (adhesion layer, 500 nm

thick) and gold (masking layer, 750 nm thick). The metal layers were photolithographically patterned and etched with 1:2:10 I_2:KI:H_2O and 20:1:1 H_2O:HF:H_2O_2 to define transparent circular openings for printing the xerogel sensors.

Sensor array fabrication: We formed the xerogel-based sensor elements by pin-printing with a 250μm diameter solid tungsten pin onto the surface of the masked substrates. Substrates were cleaned by an EtOH rinse, then with 1 M NaOH, washed with deionized water, cleaned with 1 M HCl, then with deionized water, at last with EtOH and then dried with N_2. The relative humidity within the printing chamber was maintained at 30$\pm$5 %, the temperature was 20-22 ^{o}C, the pin velocity was 15 mm/s with pin acceleration at 15 mm/s and pin-to-surface contact time was set at 7 ms. All sensor arrays were aged under ambient conditions in the dark for at least seven (7) days prior to assessment and testing.

3.3 EXPERIMENTAL RESULTS AND DISCUSSION

Figure 3.6 shows the experimental setup for characterizing the CMOS luminescence imaging system. A laboratory DC power supply (INSTEK: PST-3202) and a function generator (TABOR: WW2572) are used to supply the CMOS imager IC and power the blue LED (λ_{peak}=470nm) which is used as excitation source. The blue LED is located in a test chamber along with the 3x3 O_2 sensor array. The O_2 concentration in the test chamber is controlled by a custom built flow-meter, consisting of a matched pair of air flow controllers connected to O_2 and N_2 gas cylinders. The temperature of the air flow is controlled by using a thermal oven and monitored using a thermometer. The thermal oven is fitted with tubes to allow the gas to enter and leave the oven. Sufficient time is allowed for the gas to be heated inside the oven before the measurements are taken. The

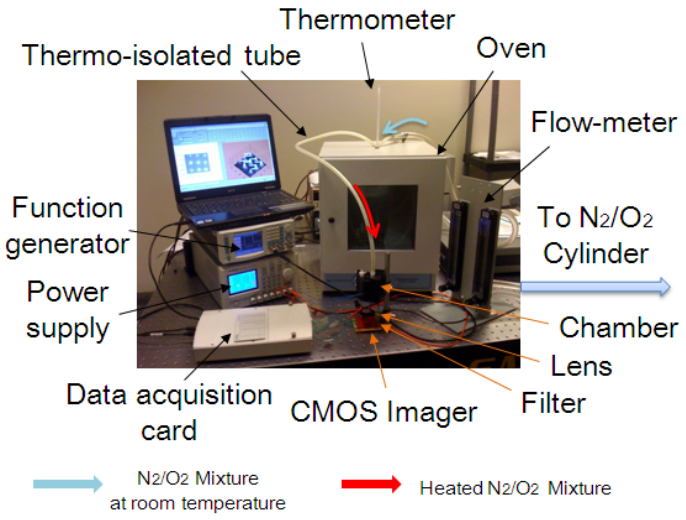

Figure 3.6 Experimental setup for evaluating the luminescence imaging system

test chamber is placed very close to the oven to minimize the ambient exposure time of the heated gases (Note: the gas tubes used are thermally insulated.) Even with all these precautions we cannot guarantee that the temperature of the gases can be accurately controlled. In the following temperature analysis we only record the temperature as set by the thermal oven and the actual temperature of the gases may be slightly different. Hence, the temperature gradient which is well regulated by the thermal oven may be a more accurate measure to analyze the obtained results. This arrangement was used as the imager IC was required to be kept at room temperature.

In the test chamber, a long-pass optical filter (Cut-off, λ = 590nm) is placed between the chamber and the imager IC to remove the LED excitation optical signal and allow only the sensor array luminescence to fall on the imager. A bi-convex optical lens (Diameter =25.4mm, Focal length=25.4mm) is used to focus the luminescence signal from the sensor array onto the CMOS imager. A data acquisition card (NI: DAQPad-6259) connected to a personal computer is used to process the CMOS imager serial

output signal. The imager sampling frequency is set at 100Hz (T_{sample}=5ms) in all the subsequent experiment testing.

Figure 3.7 shows the visualized luminescence images of the 3x3 sensor array when the O_2 concentration is varied from 0% to 100% at room temperature (25^{o}C). All three sensor elements arranged in a column are designed to provide identical sensitivity to O_2 concentration. Figure 3.8(a) shows the averaged response curves of all sensor elements for multiple measurements. For each measurement the data point is taken from the peak response of each sensor element in the 3 by 3 array. We notice in Figure 3.8(c) the response curve of sensor C1 behaves too differently with sensor C2 and C3. The sensor

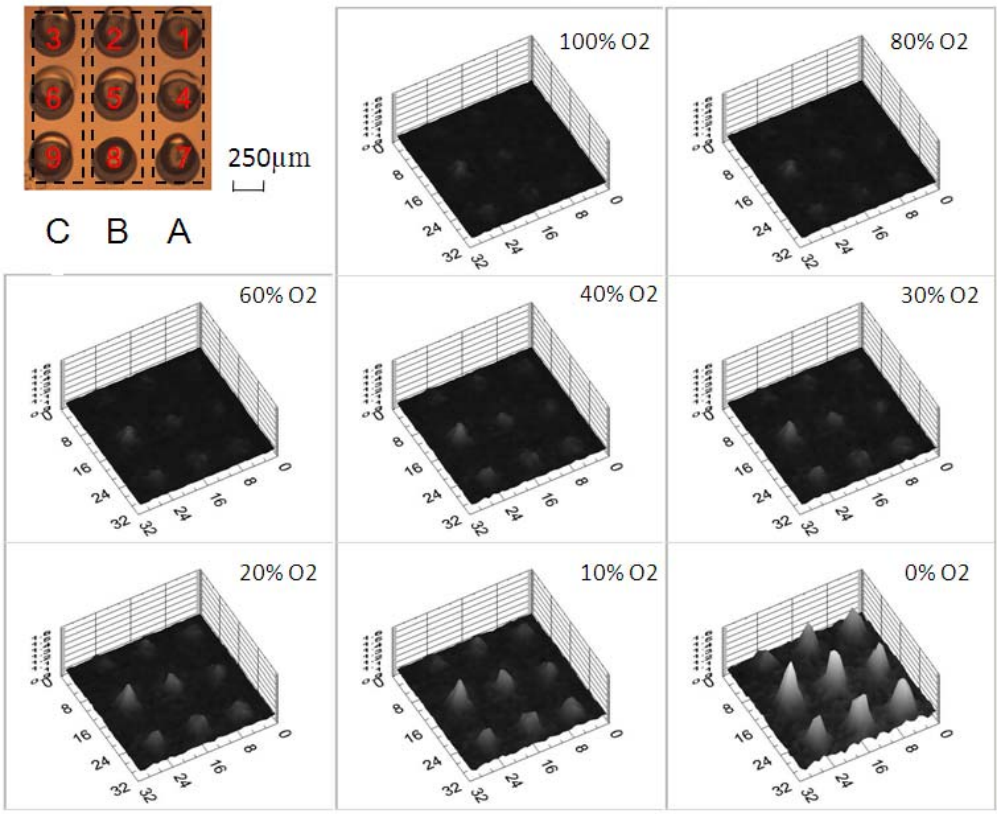

Figure 3.7 Visualized images from the CMOS IC with varying O2 concentrations at room temperature (25^{o}C)

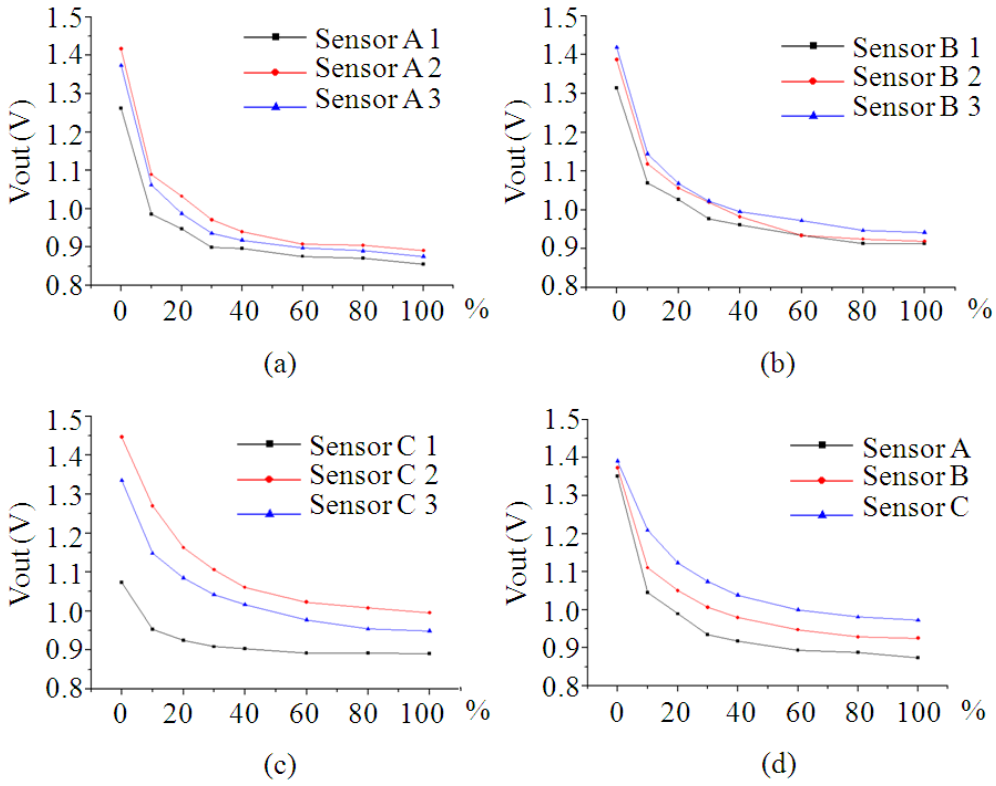

Figure 3.8 Response curves of sensor elements in the array

C1 is considered as one failure element (due to degradation of the material/misalignment during the array fabrication) and is dropped in the further data process. As expected, from Figure 3.8(d) each type of sensor provides a different average sensitivity as following: sensor type A (4.78±0.36 mV/%O_2 change), sensor type B (4.49±0.23 mV/%O_2 change), and sensor type C (4.19±0.3 mV/%O_2 change).

Figure 3.9 presents the Stern-Volmer plot of the three different sensor types at room temperature. Here, the simulated value of the imager offset voltage (802mV) is subtracted from the measured voltage values for the different O_2 concentrations. The graph shows the ratio of the voltage value when no oxygen is present to the voltage value for different O_2 concentrations (i.e., I_0/I). Data of sensor A3, B3 and C3 are taken to demonstrate the Stern-Volmer response and are fit using Equation 3.1. The obtained data exhibit a non-

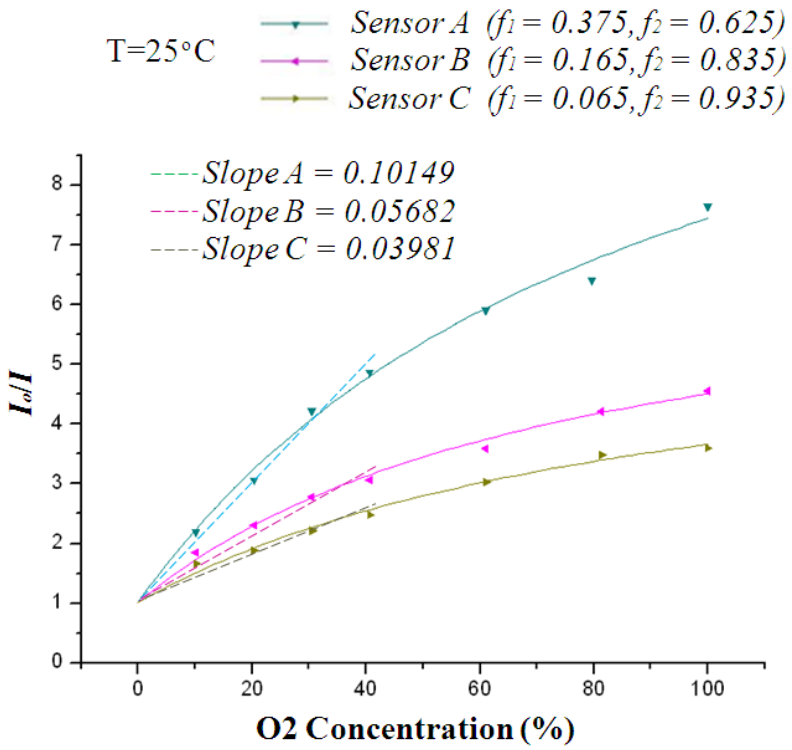

Figure 3.9 Stern-Volmer plot of sensors (A, B and C) fit into a linear Stern-Volmer response (Equation 3.1) at room temperature

linear response as expected for the binary array used here and matches well with the response obtained previously for similar sensors [134]. We then graph a linear fit (shown by dotted lines in Figure 3.9) to the individual sensor responses at lower oxygen concentrations (<40% O_2 concentration with respect to N_2). This allows simplified process to solve Equation 3.1 to determine K_{SV1} and K_{SV2}.

The availability of three independent responses from Figure 3.9 helps in solving for the values of f_1, f_2 (1-f_1), K_{SV1} and K_{SV2} of the sensor microarray (from Equation 3.1). As the temperature of the O_2 gas is changed, the values of f_1 and f_2 (1-f_1) does not change as it is the same sensor array, but the values of K_{SV1} and K_{SV2} change. We repeat the process as described in the previous paragraph for different temperatures. At each temperature, we plot the sensor response and use a linear fit to the response at lower O_2 concentrations

to form 3 equations (using Equation 3.1 for the different sensor types) to determine K_{SV1} and K_{SV2}. In all cases, we use identical values of f_1 and f_2 (1-f_1) as shown in Figure 3.9 to calculate the values of K_{SV1} and K_{SV2}.

In Figure 3.10, we report the temperature-dependent K_{SV} values between 25°C and 50°C (as recorded by the thermal oven). K_{SV1} (associated with $[Ru(dpp)_3]^{2+}$) decreases as temperature increases. This suggests that, within the xerogel matrix, the $[Ru(dpp)_3]^{2+}$ k_q temperature dependent increase is exceeded by the $[Ru(dpp)_3]^{2+}$ τ_0 temperature dependent decrease, leading to a K_{SV1} that decreases as temperature increases. K_{SV2} (associated with $[Ru(bpy)_3]^{2+}$) appears to be temperature independent. This suggests that, within the xerogel matrix, the $[Ru(bpy)_3]^{2+}$ k_q temperature dependent increase is compensated by the

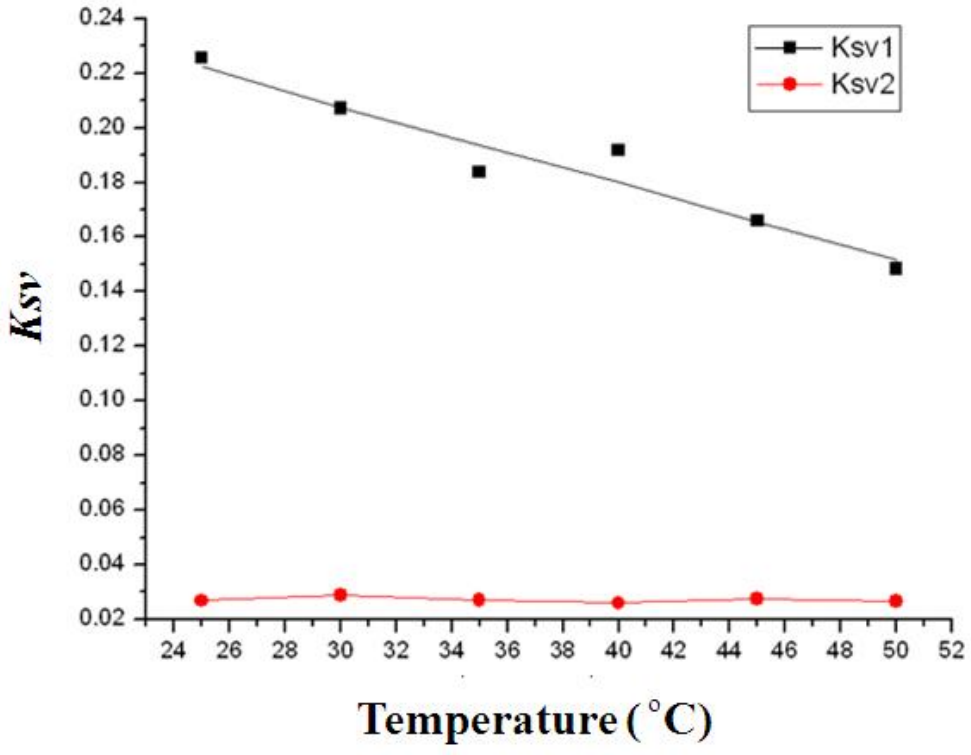

Figure 3.10 Simplified block diagram of the CMOS based multi-sensor system

$[Ru(bpy)_3]^{2+}$ τ_0 temperature dependent decrease, leading to a K_{SV2} that appears to be temperature independent. In summary, Figure 3.10 reports a significant result in understanding the temperature dependence of photoluminescence based sensor microarrays of the type described herein.

3.4 SUMMARY AND CONCLUSIONS

In this chapter it presents the design and implementation of a CMOS multi-sensor microsystem prototype using pin-printed luminescent xerogel sensor microarray and custom designed CMOS imager. The effect of temperature on the operation and performance of the sensor microarray is also studied. We described the development of a low noise, low power consuming, and high sensitivity CMOS imager which is used to image the luminescence response of the xerogel based sensor microarray. The xerogel microarrays were deposited using micro-pin printing and we employed the strategy of mixing different ratios of two oxygen sensitive luminophores in each sensor spot in the microarray to generate sensor responses with different sensitivities. The technologies reported here can be used in near future to develop low power and intelligent optical sensor microarrays which can be dynamically calibrated for temperature variations.

CHAPTER 4 LUMINESCENCE LIFETIME BASED SENSOR MICROSYSTEM

As explained in Chapter 2, in luminescence oxygen sensor system lifetime based sensors are more preferable than intensity based sensors as they incorporate (a) minimal susceptibility to light source (excitation) and detector drift, (b) insensitivity to changes in optical path, and (c) insensitivity to drift due to luminophore degradation and/or leaching. In Chapter 2, phase luminometry is employed to measure the lifetime indirectly and the sensor system provides robust and reliable performance compared to sensor systems based on luminescence intensity based sensors. However, there are several drawbacks that plague the phase luminometry sensing technique which include (i) lack of easy scalability for multi-sensor systems and (ii) low frequency response of the high-gain photodetectors which limits the operation of the CMOS phase luminometry system to luminophores with excited state lifetimes on the order of few microseconds and longer. Further, the output provided is an analog voltage which has to be converted to digital signals for storage or transmission. Here, in this chapter we propose a new technique named Direct Time Interval Measurement (DTIM) to directly measure the lifetime of the luminescence.

The proposed DTIM technique is based on transient response of luminophores and time-to-digital conversion technique that has comparatively simple circuit implementations compared to other direct time domain measurement techniques and provides a direct digital signal output. The general system block diagram of DTIM is

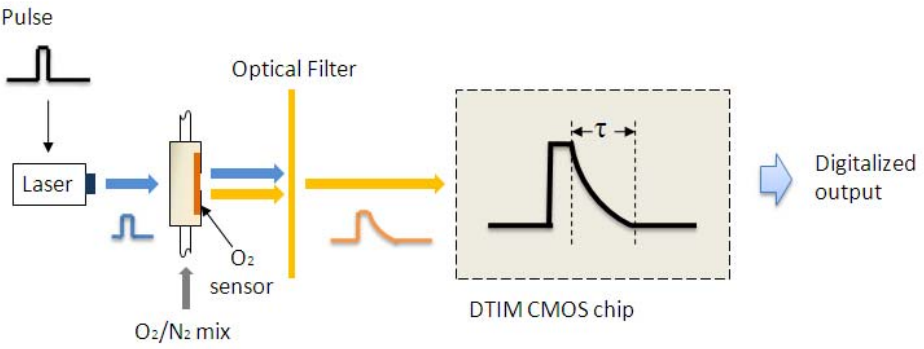

Figure 4.1 Simplified block diagram of the CMOS based multi-sensor system

shown in Figure 4.1. The excitation source shown in Figure 4.1 is a laser pulse. The xerogel sensors used are similar to sensors described in Chapter 2. The luminescence generated from the xerogel sensors upon excitation has an exponentially decaying response with a lifetime dependent on the ambient oxygen concentration. This decaying luminescence is detected by DTIM CMOS IC and provides an output digital signal. The DTIM CMOS IC has to be designed strategically to interpret the lifetime information containing in the decay of the luminescence.

4.1 DTIM CMOS IC

Figure 4.2 shows the block diagram of the DTIM IC. The IC includes a phototransistor array (PTA), transimpedance amplifier (TIA), regulated gain amplifier (RGA), fall time detector (FTD), and time-to-digital convertor (TDC). The circuitry (except PTA) is covered by metal layer to prevent noise due to interference of optical signals with circuitry. In operation, an LED is used to generate short pulses repeating at a low frequency (few hundred hertz) to excite luminophores which subsequently generate exponentially decaying luminescence response. The luminescence response is detected and processed by the DTIM IC which is designed and fabricated in TSMC 0.35µm-

CMOS process available through CMC (www.cmc.ca). The microphotograph of the IC is shown in Figure 4.3.

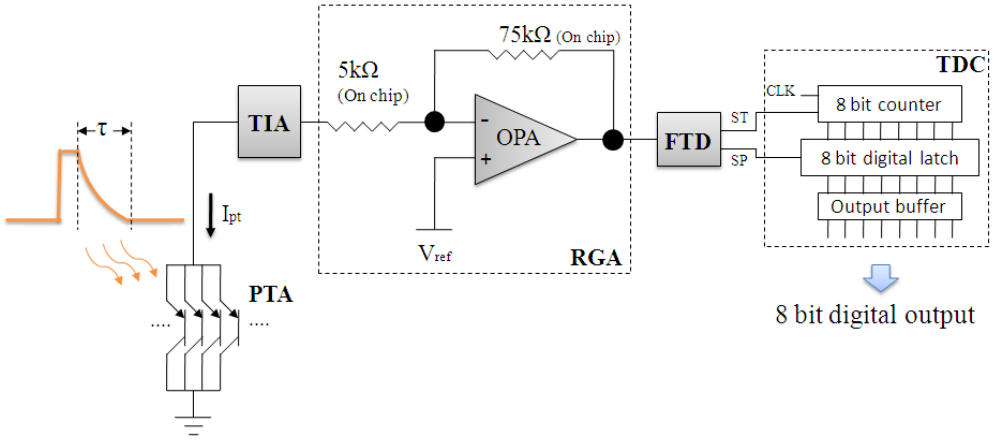

Figure 4.2 Block diagram of the DTIM IC

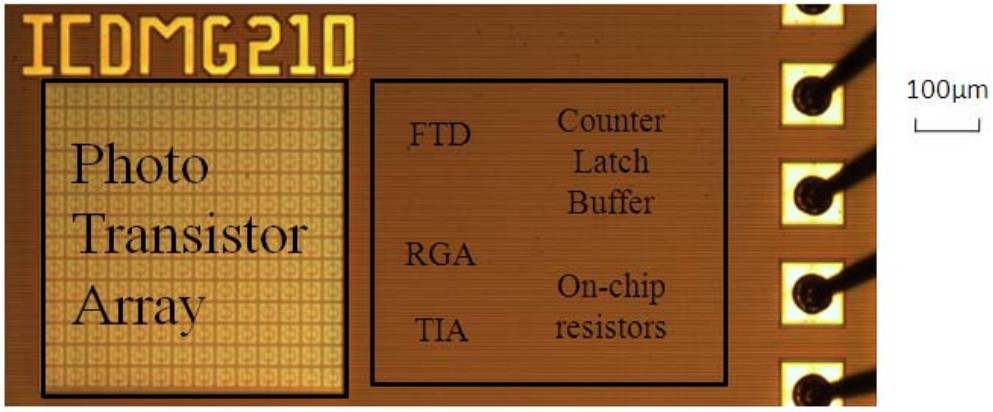

Figure 4.3 Microphotograph of DTIM IC

4.1.1 PHOTOTRANSISTOR ARRAY (PTA)

The PTA consists of 196 identical phototransistors connected in parallel and arranged in 14 x 14 array occupying 490µm x 490µm area. Each phototransistor is similar to a bipolar junction transistor and is formed by p-active (emitter) / n-well (base) / p-substrate

(collector). We already examined several times in previous chapters this vertical phototransistor which has high responsivity in the visible electromagnetic spectrum [41]. The photo-current from the PTA is converted to a voltage signal and amplified by a transimpedance amplifier (TIA).

4.1.2 TRANSIMPEDANCE AMPLIFIER (TIA)

To detect the falling edge of the luminescence, a wide-band TIA with a large gain to detect the weak luminescence is needed. A regulated cascode (RGC) TIA [141] shown in Figure 4.4 is used in our design for that purpose. The output node is buffered by M3 and M4 from the PTA which has large parasitic capacitance so that a higher bandwidth is achieved. The gain and bandwidth of the RGC TIA can be derived as:

$$A_{TIA} = 2 \cdot \frac{1}{g_m} = \frac{2nV_T}{I_{dc}} \qquad (4.1)$$

$$BW_{TIA} = \frac{g_m}{2\pi C_p} \qquad (4.2)$$

where $C_p = C_{GB,M2} + C_{DB,M3} + C_{in,Buffer}$.

The simulation result of the gain and bandwidth of the RGC TIA is shown in Figure 4.5. For the current design, the transfer impedance and bandwidth of the TIA is set as 11MΩ and 5MHz respectively.

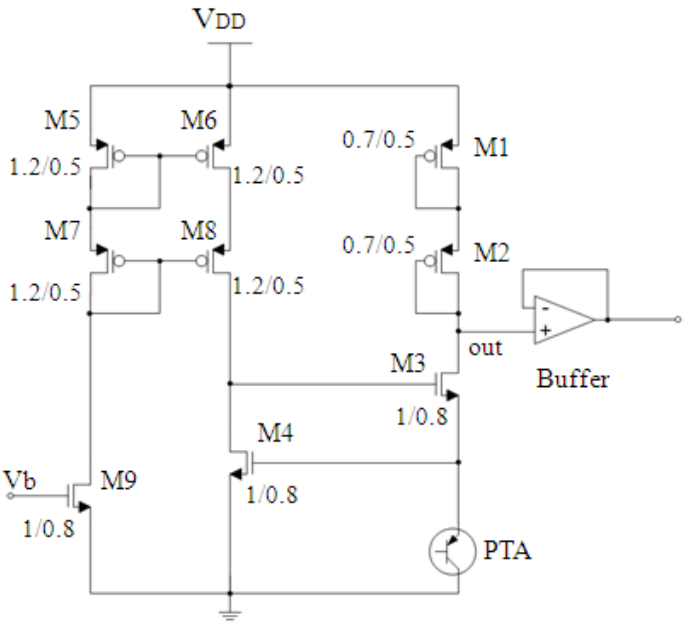

Figure 4.4 Schematic of RGC TIA (transistor size unit: μm/μm)

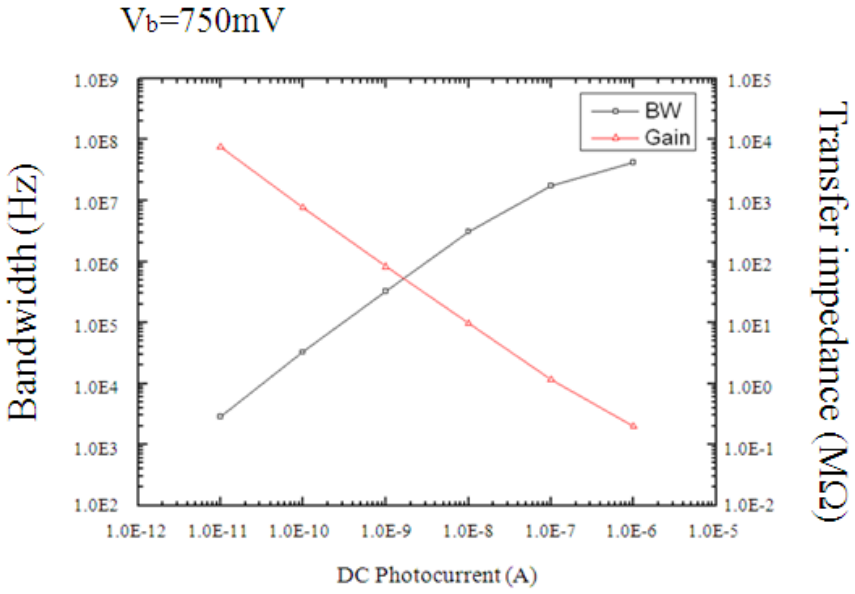

Figure 4.5 Simulation result of the RGC TIA

4.1.3 REGULATED GAIN AMPLIFIER (RGA)

The output of the TIA is amplified by RGA. The gain of the RGA is set at 15 V/V using on-chip resistors as shown in Figure 4.2. RGA includes a rail-to-rail folded-cascode

operational amplifier following the design described in Chapter 2. The bandwidth of the OPA used in RGA is designed as 205MHz which is larger than the bandwidth of the RGC TIA block.

4.1.4 FALL TIME DETECTOR (FTD) AND TIME TO DIGITAL CONVERTER (TDC)

A FTD is used to detect the decay time of the signal from the RGA. The FTD consists of a series of 16 comparators that are used to generate positive edges based on the voltage level of the input signal. From the schematic of FTD which is shown in Figure 4.6, V_{plus} is fixed and the input signal varies between V_{minus} and V_{plus}. The D Flip-Flop array and logic gates are used to track the first positive edge which indicates the start of the fall of input signal. The time interval between positive edge of signal ST and positive edge of signal SP is the fall time of the input signal. The comparators used here have complementary input stage [142] as shown in Figure 4.7. The rise/fall time of the

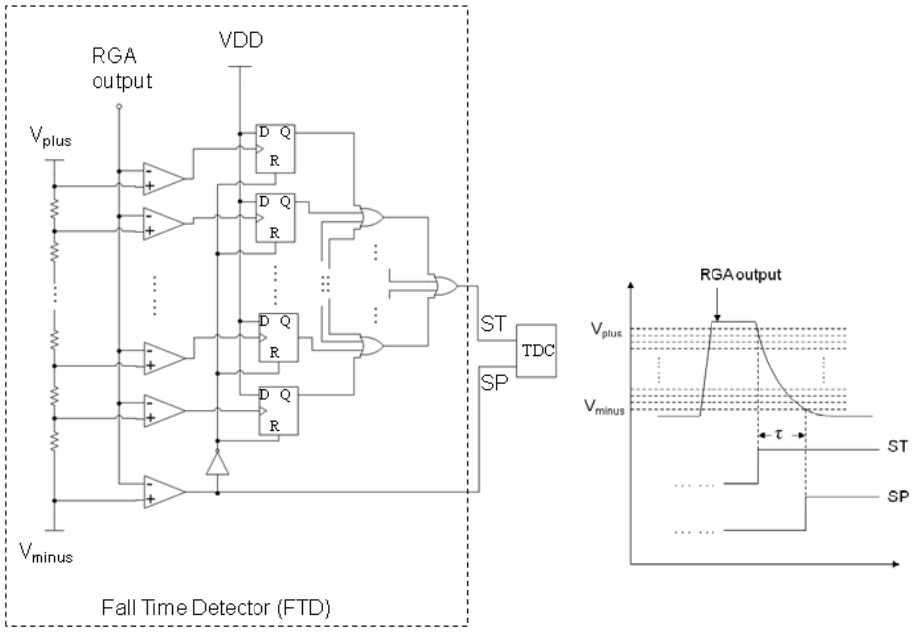

Figure 4.6 Schematic of FTD

complementary comparator is designed to stay within 10ns+/-6ns range through the full 0V to 3.3V input DC range. The output of FTD is connected to a Time to Digital Converter (TDC). All digital circuits are built using standard digital cell library provided by TSMC.

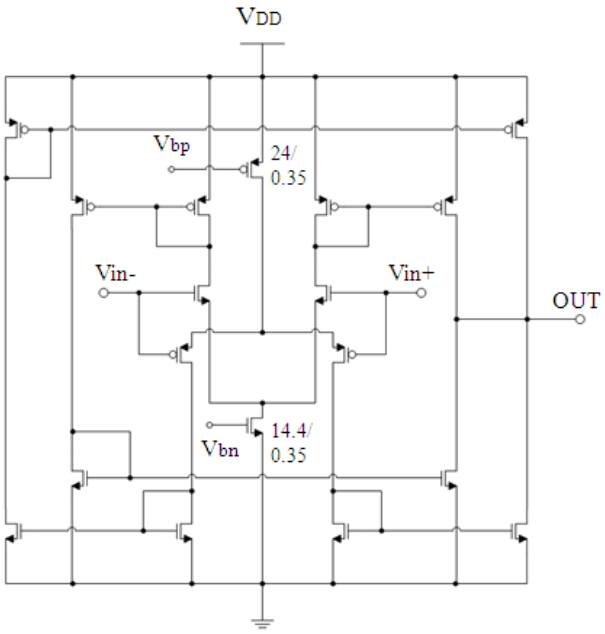

Figure 4.7 Schematic of complementary comparator used in FTD

In the TDC as shown in Figure 4.2, the positive edge of signal ST will activate an 8-bit counter. Later, the positive edge of signal SP will latch the current output of the counter. The latched 8 bits digital output represents the time interval, τ, which is read out through a buffer. The time resolution of the TDC is decided by the frequency of external clock signal CLK.

4.1.5 SYSTEM SIMULATION

Figure 4.8 shows the simulation of the DTIM IC. An ideal current source (pulse input with 9nA as 'low', 11nA as 'high') connected in parallel to a 1pF capacitor (estimated value of the parasitic capacitance of PTA) is given as input to TIA. The value of the photo-current is estimated from our previous experiments [41, 66]. The frequency of CLK in TDC is set at 20MHz for a time resolution of 50ns. From Figure 4.8, the relationship between the fall time of the input current pulse and the system output (8-bit digital output) is linear as the fall time is varied from 200ns to 14.4µs.

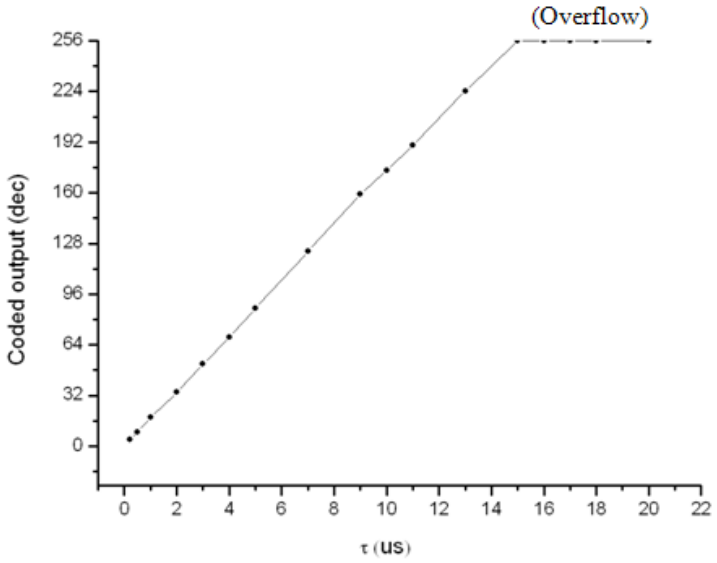

Figure 4.8 System simulation result

4.2 EXPERIMENT RESULTS

Figure 4.9 shows the measurement result of the DTIM IC when an optical signal with 4µs fall time is incident on the PTA. The oscilloscope view shows the output of RGA and FTD. The response time of the PTA, TIA and RGA cause the fall time to extend to 4.2µs. The fall time measured by FTD is 4µs as the triggering for ST and SP can be calibrated to

accommodate the response time delay of PTA, TIA and RGA, which varies little throughout the designed DTIM IC operating range (200ns to 14.4μs). The DTIM IC consumes 4.5mW of power with 3.3V DC supply and can detect luminescence lifetimes with 100ns resolution.

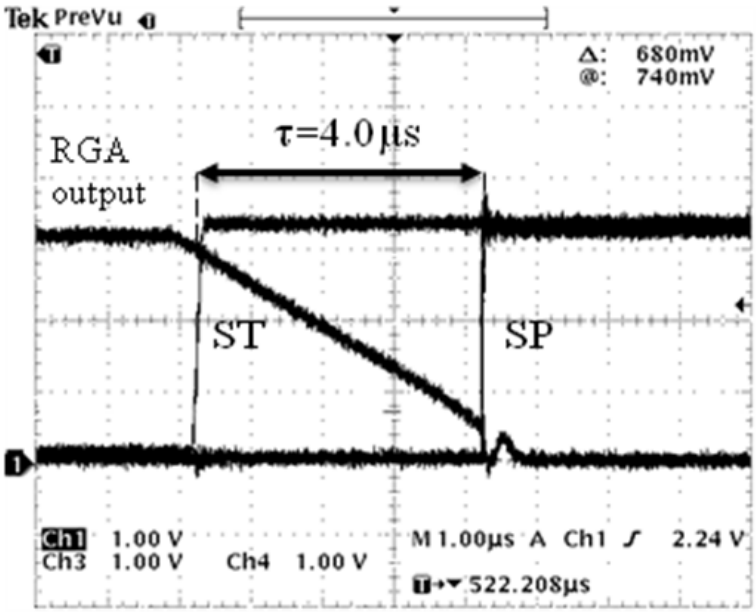

Figure 4.9 Experimental measurements of DTIM IC

4.3 SUMMARY AND CONCLUSIONS

We developed and examined a CMOS IC for the direct measurement of luminescence lifetimes in miniaturized chemical sensors. The DTIM IC, fabricated in TSMC 0.35μm CMOS process, is designed to detect lifetimes from 200ns to 14.4μs with a resolution of 100ns and provide an 8-bit digital output. DTIM system can be tuned to detect longer lifetimes. The system also allows compensation to overcome the response time delay of the photodetection and signal processing circuitry. The proposed DTIM system offers an alternative method for the luminescence lifetime measurement.

DTIM is a challenging method for luminescence lifetime measurement in the sense of its requiring large bandwidth CMOS circuits (photodetector, TIA, etc.) for short lifetime (~100ns) detection, especially with the need for large gain phototransistor as the photo-current conversion stage. The parasitic capacitance existing in the TIA stage of the fabricated CMOS IC limits the minimum detectable optical signal decay time to 4 μs in the current system, which is very different from the simulation results. The reason for this mismatch can be credited to the large active-substrate capacitance in TSMC 0.35 μm technology. This detection limit may be improved by using CMOS technology with smaller feature size. However, the designing the phototransistor array with large gain in deep sub-micron CMOS processes is quite challenging. Besides the circuit limitation, the systematic limitation in DTIM method is also noticeable. Regular LED cannot be used as the pulse excitation source since it causes decay (~μs) to the pulse excitation. When the laser is used the color filter used to remove the excitation will emit fluorescence, which makes the measurement very inaccurate particularly in the short luminescence lifetime case. In future, the TIA needs to be improved to have a wider bandwidth and systematic configuration has to be considered to direct measure the luminescence lifetime using the proposed DTIM method.

CHAPTER 5 CMOS BACTERIAL SENSOR MICROSYSTEM

As explained in Chapter 1, bacterial biosensors are very important instruments for bacteria population count and pathogenic bacteria detection in many fields such as food industry, drugs discovery, clinical diagnostics and public health security [75]. Here, in this chapter we present the design and implementation of a CMOS conductometric based sensor system for colony growth monitoring and specific sensing of *Escherichia coli* (*E. coli*) bacteria. The specific detection of *E. coli* is done by employing T4 bacteriophages as receptor organisms.

Figure 5.1 shows a simplified block diagram of the novel CMOS conductometric sensor system to achieve a portable, low cost and effective bacteria monitoring/sensing

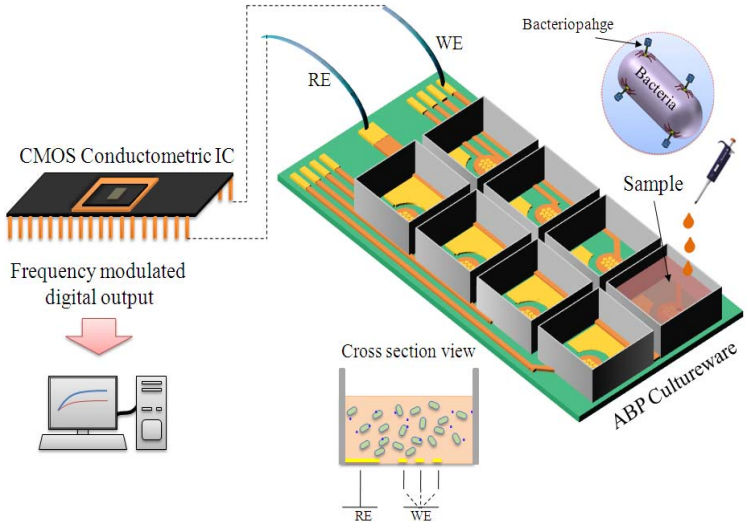

Figure 5.1 Block diagram of CMOS conductometric biosensor system

system. We employ commercially available electrode arrays (8W1E-PCB) from Applied BioPhysics Inc. (ABP) Troy, New York for immobilization of bacteriophages and subsequent bacteria sensing. The optical micrograph of one of the electrodes in the array is shown as an inset in Figure 5.2. The electrodes consist of a common reference electrode (RE) and a working electrode (WE). These electrodes are regularly used in many commercial bacterial sensor systems listed previously which will allow easy acceptance of the developed system by other academic/industry groups. The electrodes RE and WE are connected to interfacial CMOS conductometric IC followed by signal processing module. Here, the input of the conductometric IC is the resistance of the sample solution (Luria-Bertani media used for bacteria growth) between two electrodes (RE and WE) and the output and the output is frequency-modulated serial digital signal.

5.1 CMOS CONDUCTOMETRIC INTEGRATED CIRCUIT

5.1.1 SYSTEM DESCRIPTION

The CMOS conductometric IC is fabricated in TSMC 0.35μm process available through CMC (www.cmc.ca). The circuit block diagram is shown in Figure 5.2. In operation, a voltage, V_{WE}, is applied between WE and RE which generates the current, I, the value of which is based on the resistance, R, of the target solution between WE and RE (Equation 5.1). The current I is then integrated into voltage V_{int} by the integrator circuit which consists of an operational amplifier (OPA), a capacitor C_{int} (implemented on-chip) and a reset NMOS switch. The relationship between I and V_{int} during the switch's off state can be expressed by Equation 5.2,

$$I = \frac{V_{WE} - V_{RE}}{R} \qquad (5.1)$$

$$V_{int} = V_{WE} + \frac{I \cdot t}{C_{int}} \qquad (5.2)$$

where, t is the integration time. V_{int} is then compared with threshold voltage V_{th} using a comparator circuit. The comparator generates a rising edge and this rising edge is then delayed by the delay module to guarantee a complete rising edge is generated within the feedback loop. The rising edge triggers the one-shot module to generate a pulse with fixed pulse width, which resets the integrator through the reset NMOS switch and initializes the next pulse generation loop. The Power-on-Reset (PoR) signal is used to initialize the entire circuitry when the chip is powered on. Details of the circuit blocks will be discussed in the next section. Using Equation 5.2, the time required for V_{int} to reach the threshold voltage V_{th} can be expressed by Equation 5.3,

$$\tau = \frac{C_{int} \cdot (V_{th} - V_{WE})}{I} \qquad (5.3)$$

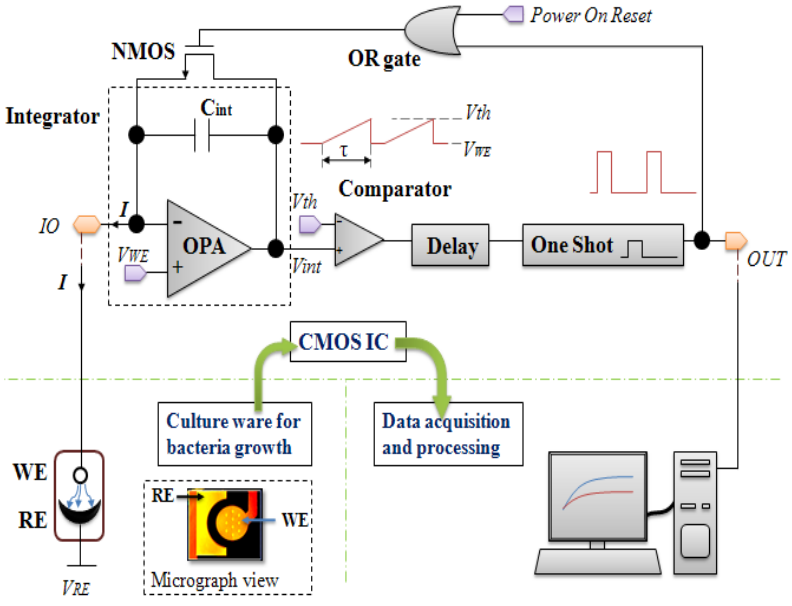

Figure 5.2 Schematic diagram of the CMOS conductometric IC and the system configuration

The output pulse period T can then be expressed by Equation 5.4,

$$f = \frac{1}{T} = \frac{1}{\tau + t_{pw} + t_d} \qquad (5.4)$$

where, t_{pw} is the pulse width and t_d is the delay time respectively. In the current system, t_{pw} and t_d *are* designed to be much smaller than τ (τ>> t_{pw}+t_d). For a simplified model, using Equations 5.1, 5.2 and 5.3, Equation 5.4 can be rewritten as,

$$f = \frac{1}{T} \approx \frac{1}{\tau} = \frac{V_{WE} - V_{RE}}{R \cdot C_{int} \cdot (V_{th} - V_{WE})} \qquad (5.5)$$

From Equation 5.5, the CMOS conductometric IC converts the resistance between the two electrodes WE and RE into a frequency representation which is processed by subsequent data acquisition system. The IC layout and micrograph are shown in Figure 5.3. The circuit details are not seen under the microscope view because the top dummy metal layer is added for thermo balance during the fabrication. The size of the CMOS conductometric IC is 190µm by 220µm (bonding pads excluded). The IC consumes an average power of 1.85mW with 3.3V DC power supply.

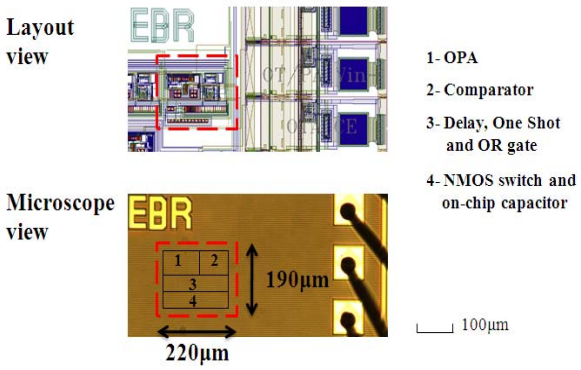

Figure 5.3 Layout and Microscope view of the CMOS conductometric IC

5.1.2 CMOS CONDUCTOMETRIC INTEGRATED CIRCUIT DESIGN

The CMOS circuitry mainly consists of three circuits: 1) integrator, 2) comparator and 3) digital conversion block which includes delay circuit, one-shot circuit, and OR gate.

Integrator: the integrator converts the current I flowing through the sample solution into a voltage signal V_{int} at the output node of the integrator. The schematic of the OPA is shown in Figure 5.4, with its critical simulation parameters listed in Table 5.1. The OPA is designed to be as versatile as possible such that it can operate with different system configurations (different C_{int}, V_{WE}, etc.) at the cost of large power consumption. Further improvement and compromise can be made in subsequent versions. The capacitor C_{int} implemented on-chip as 10pF using poly1-ploy2 structure. The size of the NMOS working as a switch is 4µm/0.5µm.

Comparator: the comparator compares the output of the integrator with V_{th} and gives out a rail-to-rail digital output. A rail-to-rail comparator [142] described in chapter 4 is implemented to process any type of signal coming from the integrator. Its schematic is

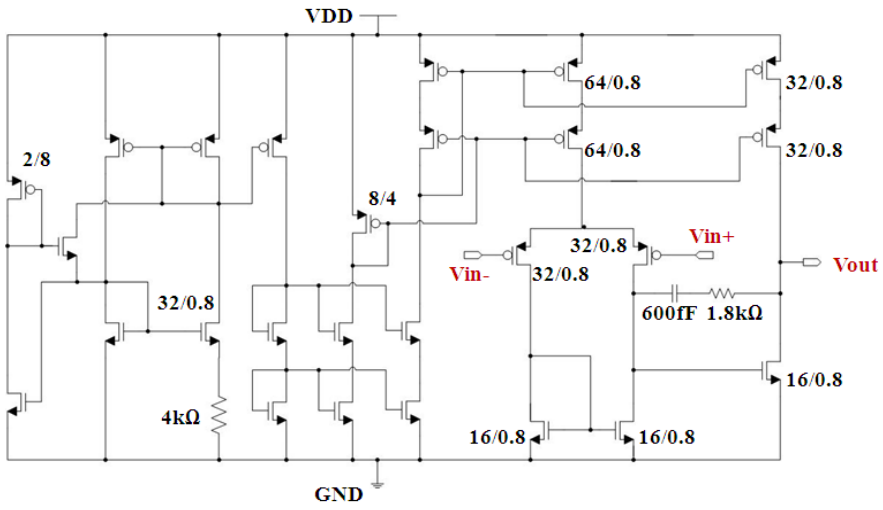

Figure 5.4 Schematic of OPA used in the integrator (The size of all unlabelled NMOS is 4µm/0.8µm, and the size of all unlabelled PMOS is 8µm/0.8µm)

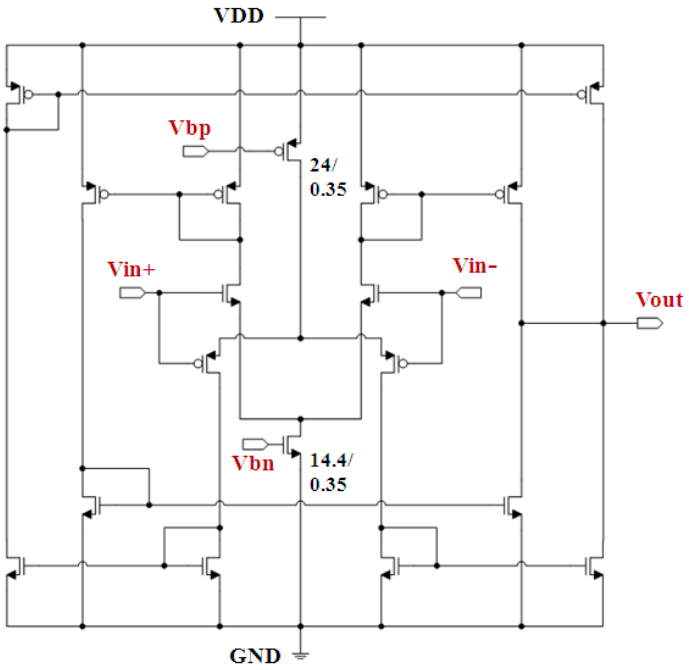

Figure 5.5 Schematic of the rail to rail comparator (The size of all unlabelled NMOS is 2.4µm/0.35µm, and the size of all unlabelled PMOS is 4µm/0.35µm)

Table 5.1
SIMULATED PARAMETERS OF OPA

Parameter	**Value**
DC gain	73.1dB
Bandwidth	206MHz
Slew rate	121MV/s (100mV step)
Phase Merge	81degree
Input swing range	0~1.75V
Output swing range	270mV~2.5V
Power consumption	1.15mW

again shown in Figure 5.5. This comparator overcomes the issue with comparator circuits with NMOS input or PMOS input stage that can only work within a certain range of input voltages as shown in Figure 5.6.

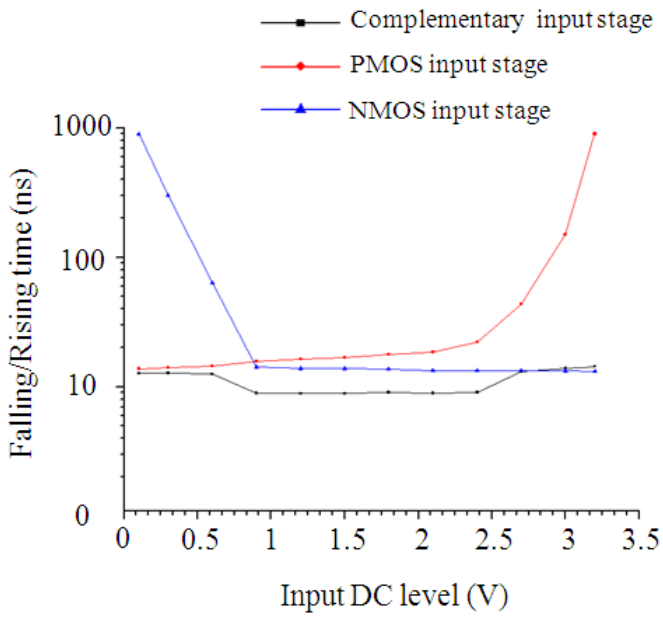

Figure 5.6 Simulated output rising/falling time using rail to rail comparator architecture (Vbn=0.7V, Vbp=2.5V)

Digital Conversion Circuit: The digital conversion circuit expands the digital pulse given out by the comparator to a fixed width pulse for further signal processing and initialize the integrator for the next pulse generation. The main part of the digital conversion block is the one-shot circuit. The schematic of one-shot circuit is shown in Figure 5.7. Once a rising edge is generated by the comparator, the D flip-flop is triggered to pass the VDD at node D to the output node Q. Then the capacitor, C_{os}, starts charging through, R_{os}. Theoretically, once the node *E* is charged beyond ½ VDD, *RST* is enabled and 0 is generated at the node Q. Thus, a complete pulse is generated with pulse width equal to t_{pw} which is determined by the time constant of the charging circuit related to R_{os} and C_{os}.

The delay circuit inserted between comparator and one-shot circuit is used to guarantee a complete rising edge is generated for the D flip-flop. As we can see from Figure 5.2, the rising edge would be incomplete if the initial signal generated by OR gate

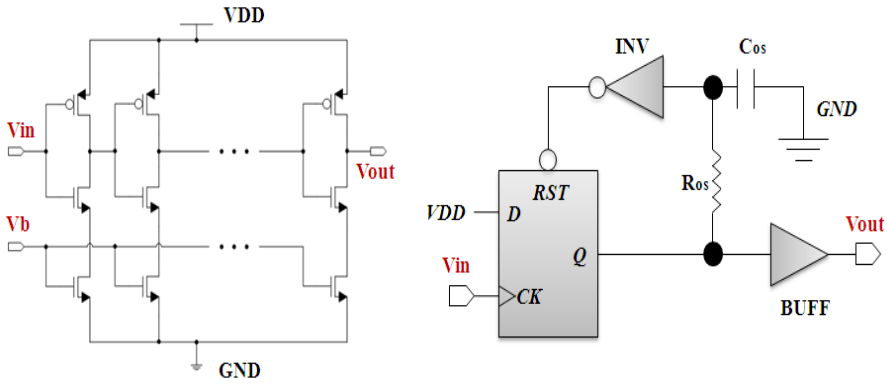

(a) (b)

Figure 5.7 (a) Schematic of delay circuit and (b) schematic of one shot circuit (The size of all unlabelled NMOS is 4.9µm/0.35µm, and the size of all unlabelled PMOS is 6.3µm/0.35µm.)

arrives before the output of comparator reaches VDD, which causes uncertainty in the circuit system. The schematic of the delay circuit is shown in Figure 5.7. The delay time is designed as 50ns based on the simulated rising time of the comparator shown in Figure 5.6 which is around 10ns. The OR gate together with the external *Power-on-Reset* signal are used to initialize the operation of the circuit system.

5.1.3 CMOS IC CHARACTERIZATION

All control parameters of the CMOS conductometric IC system, such as C_{int}, R_{os}, C_{os}, V_{th} and V_{WE}, have to be set before the actual experimentation. One constrain in selecting the values of these components is the ability of the National Instruments Data Acquisition card (NI-DAQ) for continuous recording and storing the data into a computer. Bacterial analysis based on population growth monitoring typically take about 2-24 hours depending on the initial Colony Forming Unit (CFU) count of the bacteria. Lower bacterial CFU take longer time to monitor. Hence, the NI-DAQ is set at a low sampling frequency to avoid unmanageably large amount of data. On the other hand, to ensure the

output pulse is accurately acquired the sampling rate cannot be set too low. Here, the t_{pw} is set as 1μs which sets the sampling rate of the data acquisition module to 10M/s (10 samples/pulse width). Under this constrain, R_{os} is selected as 200kΩ and C_{os} = 3pF. The measured t_{pw}=0.96μs is shown in Figure 5.8. The theoretical value of t_{pw} using R_{os}=200kΩ and C_{os}=3pF is calculated as 0.66μs. The reason for this mismatch is due to the parasitic capacitance of the chip pads which contribute an extra 1~2pF to C_{os}.

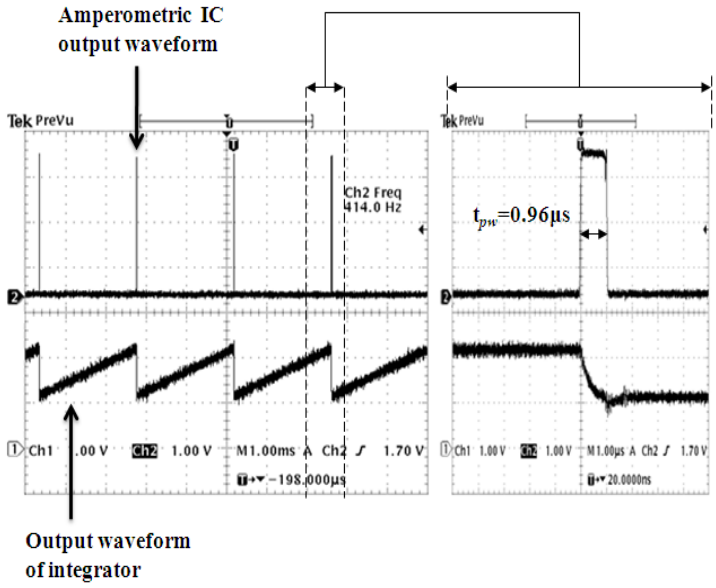

Figure 5.8 Measured output waveform of the configured conductometric IC system (square wave) and the output waveform of the integrator (triangle wave) under the condition of R equals to 6MΩ

The output frequency range is set as less than 5 kHz (τ=50 μs) to satisfy the condition $\tau >> t_{pw}$ to have an accurate conversion between *f* and R using Equation 5.5. V_{th} and V_{WE} are set as 2.2V (2/3VDD) and 1.1V (1/3VDD), respectively, both of which are within the OPA's input swing range. V_{RE} in Figure 5.2 is set as 0.5V to obtain a potential difference of 0.6V between WE and RE. C_{int} is chosen as 220pF to generate output frequency between 100 Hz and 5 kHz when the resistance, *R*, varies from 500kΩ to 25MΩ which is

the resistance range of the samples tested in this work based on the primary test results obtained using a standard multimeter.

A typical waveform of the CMOS conductometric IC system under the above configuration is shown in Figure 5.8 in which one 6MΩ resistor is connected between WE and RE. The conversion characteristic of the configured system can be presented by replacing parameters in Equation 5.5 with the values selected above,

$$f = \frac{2.48}{R} \quad GHz \qquad (5.6)$$

The actual conversion characteristic of the configured CMOS conductometric IC system is calibrated by connecting different values of standard resistors between WE and

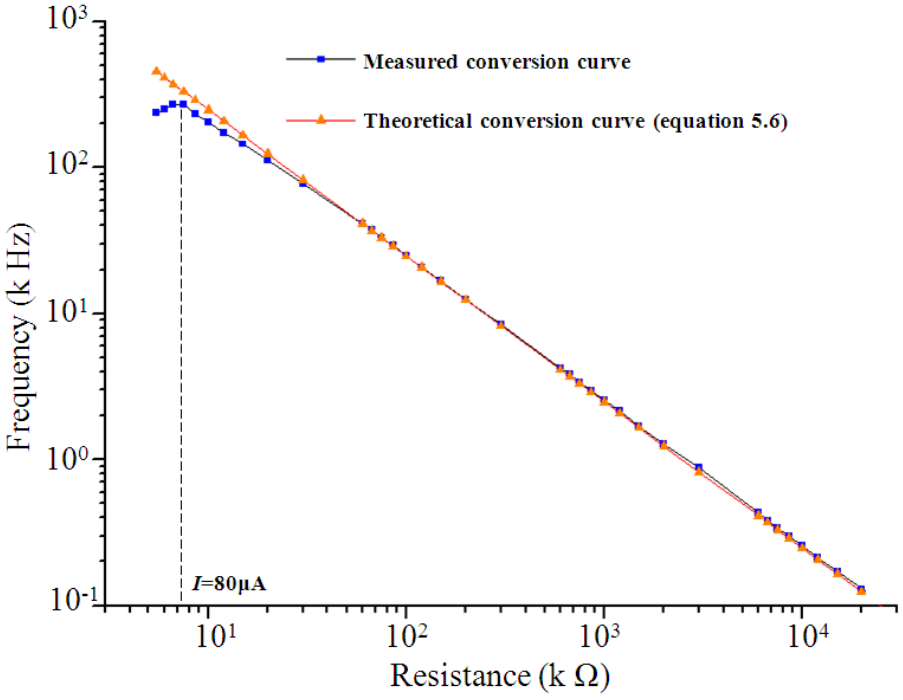

Figure 5.9 Measured and theoretical conversion curve of the configured CMOS conductometric

RE. The measured result is shown in Figure 5.9. The measured curve is in good match with the theoretical curve when the output frequency is less than 100 kHz. When the output frequency is higher than 100 kHz (τ=10 μs) the assumption $\tau >> t_{pw}+t_d$ which is used to derive Equation 5.6 is invalid and so the measured response diverges from the theoretical curve. At a critical point when R is so small that the generated current I exceeds the maximum current the OPA's output stage can supply, the circuit system fails to respond correctly. Figure 5.9 is used as the f-R conversion chart in all the following experiments.

5.2 BIOLOGICAL MATERIAL AND METHODS

5.2.1 BACTERIA AND BACTERIOPHAGE

As introduced in the first chapter, the electrical properties of a bacterial cell have been studied for many years [109, 117-118]. It was reported that the resistance coefficient of a bacteria membrane ranges from 10^2 and 10^5 $\Omega \cdot cm^2$ [109] which is much more insulating than the bacteria culture media (Luria-Bertani (LB) media). Based on this resistance difference, resistance changes between WE and RE (Figure 5.2) during the bacteria growth can be detected using the CMOS conductometric IC system. The utilization of bacteriophages as bioreceptors for specific bacteria detection has also been studied for many years [102, 113-114]. Bacteriophages are viruses that recognize specific receptors on the bacterial surface to which they bind and inject their genetic material. Such injection allows replication of the phage and release of a new generation while killing the bacteria.

Here in this chapter, the most well studied bacteriophage enterobacteria phage T4 (also called as coliphage T4 or T4 phage in short) [115-116] is used as the bioreceptor to

recognize the target bacteria *Escherichia coli (E. coli)*. This T4 phage can recognize and lysis *E. coli* cell by replicating itself within *E. coli* cell during the bacteria's exponential growth after capturing *E. coli* cell and injecting its DNA genome into the cell. To compare and confirm the interaction between T4 phage and *E. coli*, another bacteriophage T4_43amE4322 B22 is used in the experiments here as control. T4_43amE4322 B22 phage is a mutant T4 phage which can also capture *E. coli* cell and inject its DNA genome into the bacteria cell. But it cannot replicate itself during the bacteria growth due to the mutation, thus cannot lysis the bacteria cell.

5.2.2 BIOLOGICAL MATERIALS PREPARATION

Culture media: Culture media for the bacteria and the bacteriophages amplification used in the experiments were LB with casein peptide 10g/L, yeast extract 5g/L, NaCl 5g/L maintained at pH 7±0.2.

Bacteria: E. coli strain B (purchased from ATCC, product number 11303) was used as the target bacteria in all of the following experiments. The bacteria were incubated in LB broth at 37°C with 250 rpm agitation for 3 hours. The incubated bacteria stock was stored at 4°C in refrigerator after incubation. Bacterial titration on LB agar petri dish was used to determine the concentration of the bacteria stock and then it was diluted into specific concentrations. 10μL of seven dilutions (dilution factor $D_B = 10^{-1, -2, -3, -4, -5, -6, -7}$) of the bacteria stock were put on LB agar Petri-dish separately. The LB agar Petri-dish was dried and then put into the incubator overnight at 37°C. The colony number (N_C) was done using a colony counter the following day. The dilution with the clearest colonies counting was selected to calculate the concentration of the original bacteria stock based on the following Equation,

$$Bacterial\ \ titer = N_C \times \frac{1}{D_B} \times \frac{10\mu L}{1mL} \quad \text{(CFU/mL)} \qquad (5.7)$$

where, CFU is notation for Colony Forming Unit. After the concentration of the bacteria stock was determined, dilutions were made using the bacteria stock and the LB to produce *E. coli* samples with specific concentrations for experimentation.

Bacteriophage: T4 bacteriophages were purchased from ATCC (product number 11303-B) and T4_43 amE4322 B22 bacteriophages were prepared in-house at BioPhage Pharma Inc. Amplification of T4 phages was done on *E. coli* strain CAJ 70 purified by ultra-centrifugation for 1 hour at 15 000 rpm, suspended in SM solution (NaCl 5.8g/L, $MgSO_4$-$7H_2O$ 2.0g/L, 50 ml/L of Tris-HCl 1M pH 7.5, 1ml/L of gelatin 10%(w/v), autoclaved 30 minutes). Amplification of T4_43amE4322 B22 (T4_43) phages was done on *E. coli* strain CR63/5 in the same way as T4 phage. The concentration of the amplified phages was determined based on titration on a bacteria lawn. The LB agar Petri dishes were prepared by pouring 3 ml of LB top agar (7g/L of bacteriological agar) and being kept at 52°C before using. 100 µl of *E. coli* strain CAJ 70 (for T4) or CR63/5 (for T4_43) fresh culture was put on the surface of the LB agar as bacteria lawn. Then, 10µL of seven dilutions (Dilution factor $D_P = 10^{-1, -2, -3, -4, -5, -6, -7}$) of the amplified phage were put on the LB agar layer separately. The LB agar Petri-dish was dried and then put into the incubator overnight at 37°C. The number of the lysised plaque (N_{DP}) in the bacteria lawn is counted the following day using a colony counter. The concentration of the amplified phage was calculated using the dilution with clearest count based on Equation 5.8,

$$Bacteriophage\ \ titer = N_{LP} \times \frac{1}{D_p} \times \frac{10\mu L}{1mL} \quad \text{(PFU/mL)} \qquad (5.8)$$

where, PFU is notation for Plaque Forming Unit. After the concentration of the amplified phage was determined, dilutions were made using the amplified phages and the LB to produce phage samples with specific concentrations for experimentation.

5.3 Experimental Results and Discussion

Figure 5.10 shows the experimental setup for the bacteria monitoring system. One ABP Cultureware™ 8-well array is filled with different *E. coli* solutions and is placed into an incubator (Lab-line air-Jacketed Flo-Thru CO_2 incubator model 320). The CMOS conductometric IC system is connected with the ABP cultureware through a wire outside the incubator to measure the current flowing through the *E. coli* solutions. A National Instruments data acquisition card (NI: DAQ, model: 6259) connected to a computer was used to collect and process the output of the CMOS conductometric IC system. A

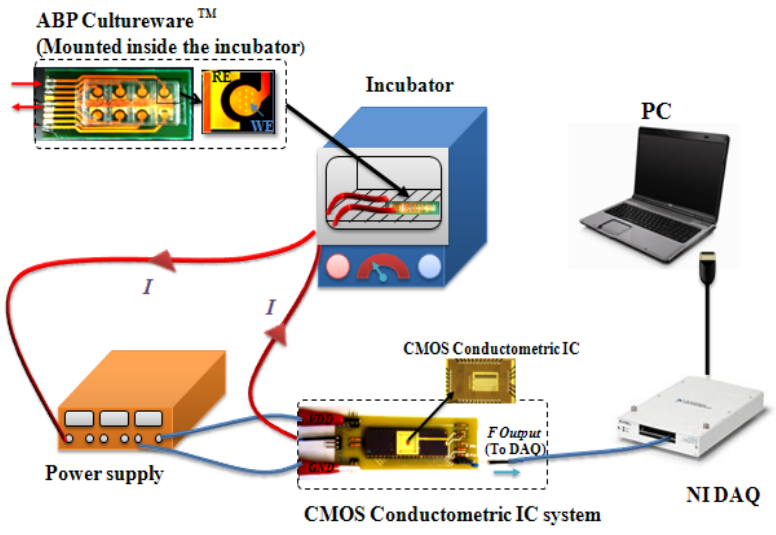

Figure 5.10 Experimental setup for the bacteria monitoring system

laboratory DC power supply (INSTEK: PST-3202) was used to power the CMOS system.

In the first experiment the CMOS system is used to monitor the *E. coli* growth. One LB sample (used as control or baseline) and three test *E. coli* samples with different initial concentrations are monitored simultaneously. Monitoring the growth of larger concentrations of bacteria (greater than 10^5 CFU/mL) is fairly straightforward and most available commercial bacterial monitoring systems can achieve it. The novelty and uniqueness in the current work lies in the fact that we are able to monitor extremely low concentrations of bacteria which is difficult to achieve even with many large table-top size commercial available systems. Also, monitoring of such low concentrations of bacteria has never been previously demonstrated with a CMOS IC based system.

The test samples include LB only, $4x10^2$ CFU/mL, $4x10^3$ CFU/mL, and $4x10^4$ CFU/mL. All samples are connected to the CMOS IC using a simple switch matrix controlled by the NI-DAQ. In each sample well the volume of the test sample is 600μL. The temperature of the incubator is set as 37 degree for the *E. coli* growth. The experimental results are shown in Figure 5.11 which plots the resistance between WE and RE which is converted through measured frequency using the calibration curve from Figure 5.9. Available works on CMOS bacterial detection system are listed in Table 5.2.

Table 5.2
COMPARISON OF CMOS BACTERIA DETECTION SYSTEMS

	Detection principle	**Targeted bacteria**	**Detected concentration(CFU/mL)**
[87]	Capacitive	*E. coli*	10^6~10^7
[88]	Optical	*E. coli*	10^6
[89]	Amperometric	*P. aeruginosa*	10^8
This work	**Conductometric**	*E. coli*	10^2~10^4

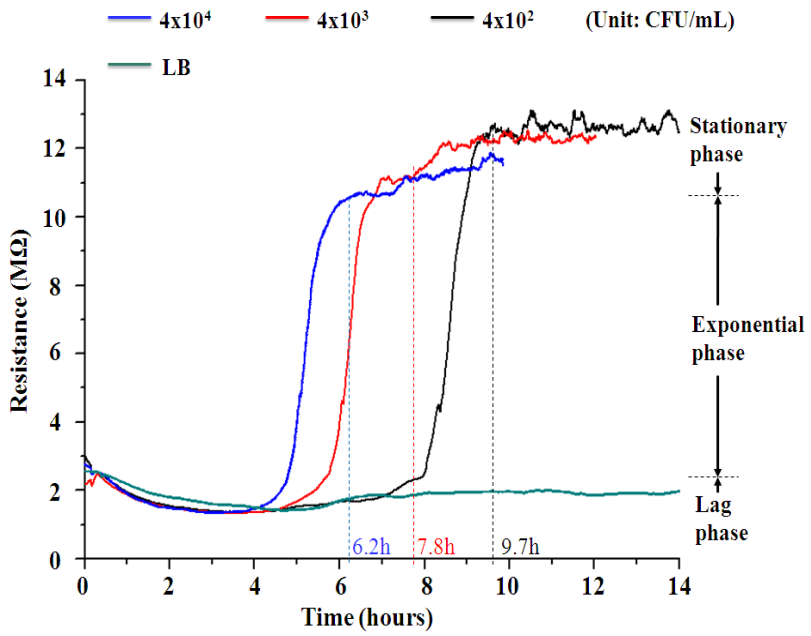

Figure 5.11 Measured resistance characteristic curve to monitor the growth of *E. coli* with different initial concentrations

As shown in Figure 5.11, three phases are monitored during the *E. coli* growth, which can be characterized by several changes in the genes expression pattern and morphological aspects [143-144]. The first phase is the lag phase during which the *E. coli* population adapts itself to the new surrounding conditions. The duration of this adaption depends on many factors such as the bacterial identity, the initial growth stage of the cells, the inoculums size and any changes in the physio-chemical environment [145]. As seen from Figure 5.11, the duration of the lag phase is inversely proportional to the initial concentration (smaller initial concentration has longer lag phase). Similar results have been previously demonstrated in other studies [146-147]. After the adaptation of the *E. coli* population to the new environment, the resistance characteristic curve enters the second phase: exponential growth phase. During this phase, the metabolic activity, DNA replication activity and protein expression activity are at the highest level. The *E. coli* cells are replicating themselves at a very high rate. As explained before the bacteria cells

are more insulating than the culture media, thus a sharp exponential increase in the resistance characteristic curve is observed during this phase. We can see a great increase of resistance due to the attachment of bacteria to the electrode surface. This exponential phase finishes when the nutriments (protein, etc.) in the culture media (LB) are exhausted and the third phase stationary phase is initialized.

During the stationary phase, the *E. coli* population stops their rapid replication due to the lack of nutriments and the accumulation of metabolic wastes, thus a flat region appears in the resistance characteristic curve (Figure 5.11). The time it takes to enter the stationary phase is inversely proportional to the initial concentration of *E. coli*: 6.2 hours for $4x10^4$ CFU/mL, 7.8 hours for $4x10^3$ CFU/mL and 9.7 hours for $4x10^2$ CFU/mL. Fewer bacteria take more time to consume all nutriments and produce enough metabolic waste to inhibit the bacterial growth. Figure 5.11 demonstrates the system's ability to monitor the bacteria growth and distinguish different concentrations of the bacteria according to the time it takes to enter the exponential phase or reach the stationary phase.

The CMOS sensor system is also tested to monitor the recognition and lysis of bacteria with bacteriophages. Three samples are prepared for this experiment: T4 phage with *E. coli*, T4_43 phage with *E. coli* and T4 phage only. The total volume is 500 µL for all these three samples but with different components: A) 100µL T4 phage (10^4 PFU/mL), 100µL *E. coli* (10^5 CFU/mL) and 300µL LB, B) 100µL T4_43 phage (10^4 PFU/mL), 100µL *E. coli* (10^6 CFU/mL) and 300µL LB, and C) 100µL T4 phage (10^4 PFU/mL) and 400µL LB. The *E. coli* was pre-incubated to accelerate the lag phase and to shorten the experiment time. As explained in section III.A, T4 phage is a bacteriophage that can specifically recognize *E. coli* strain B cell and lysis it. T4_43 phage is a mutant T4 phage that cannot lysis *E. coli*. The experiment results are shown in Figure 5.12. The T4 phage

resistance characteristic curve (curve C) is used as a base line reference showing that the sample C (T4 phage only) is relatively stable during the 24 hours of experiment. For the sample B (mutant T4_43 phage with *E. coli*), since the T4_43 phage cannot lysis the *E. coli* cell, the *E. coli* population goes through the regular bacteria growth phases (lag, exponential and stationary). This process is recorded by the system as the resistance characteristic curve B in Figure 5.12.

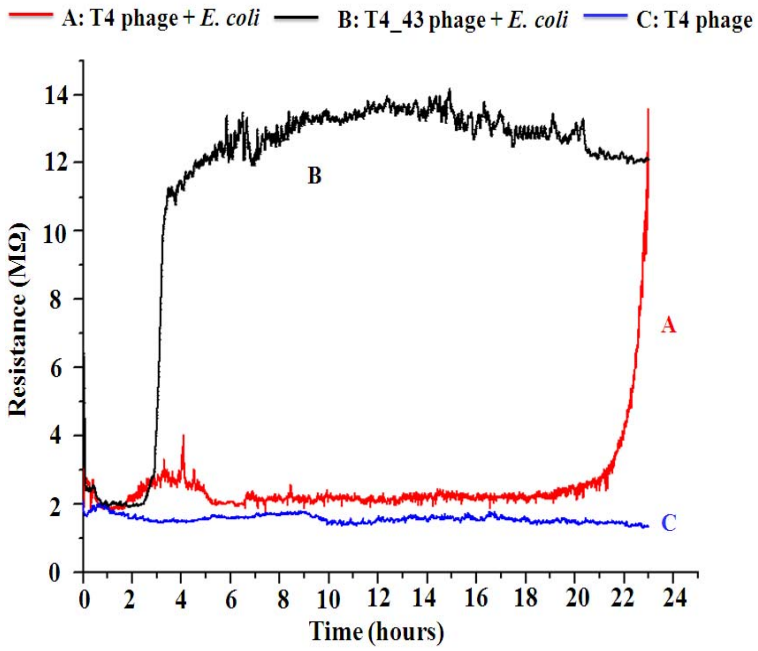

Figure 5.12 Measured resistance characteristic curve to monitor the recognition and lysising of the T4 bacteriophage to *E. coli*

For sample A (T4 phage with *E. coli*), the T4 phage can lysis the *E. coli* cell during its exponential growth as seen from Figure 5.12. In the first 2 hours the *E. coli* cell adapts itself to the new environment and the T4 phage acquires *E. coli* cell and injects DNA genome into the cell. After the adaption the *E. coli* cell tries to replicate, thus an increase in the resistance similar to the start of the regular exponential phage is observed, from hour 2 to hour 3. Along with the replication of the *E. coli* cell, the T4 phage also replicates inside the *E. coli* cell. At some time point during hour 3 to hour 4, the first

batch of infected *E. coli* cells are lysised and 100-150 new bacteriophages are released from each lysised cell [116]. Since the insulating bacteria cell is lysising at a rapid rate (1 *E. coli* cell releases 100-150 new T4 phages) a trend of decreasing in the resistance characteristic curve is observed from hour 3.5 to hour 5. After hour 5, a stationary phase is reached. This stationary phase is not like the stationary phase during the bacteria growth which is correlated to a lack of nutriment or an excess of metabolic waste. This stationary stage is observed when a population of bacteria is exposed to antibiotics or bacteriophages governed by a growth control mechanism named persistence [148-149]. During this stage, the bacteria cells stop their replication due to 'seeing' bacteria lysising and bacteriophage replication. This stationary phase lasts for 15 hours until some bacteria cells become (mutant, etc.) resistant to the phage infection. After that the exponential growth of T4 phage resistant *E. coli* bacteria group starts from hour 20 as observed in the resistance characteristics for sample A.

5.4 SUMMARY AND CONCLUSIONS

We presented the design and implementation of CMOS conductometric system for *E. coli* growth monitoring and *E. coli* sensing. The specific detection of *E. coli* was done by employing T4 phages as receptor organisms. The prototype system demonstrates the ability to monitor the three phases of *E. coli* bacteria growth and the ability to monitor the recognition and lysising process of *E. coli* bacteria with T4 phages. The novelty and uniqueness in the current work lies in the fact that we are able to monitor very low concentrations of bacteria using standard commercial electrochemical electrode arrays which will allow easy acceptance of the developed system by other academic/industry groups. The bacterial detection range can be easily tuned by changing the system parameters to directly compete in performance to more expensive large size commercial

bacterial monitoring systems. The prototype system provides an opportunity to develop portable, low cost and mass producible bacteria monitoring system which can be used for various applications.

CHAPTER 6 SUMMARY, CONCLUSIONS AND FUTURE WORK

6.1 SUMMARY AND CONCLUSION

The work presented in this dissertation was focused on the development of CMOS based sensor microsystems for biochemical applications. Specially, we concentrated on the detection and signal processing from optical based and electrochemical based sensing methodologies using custom designed CMOS ICs.

6.1.1 OPTICAL SENSING

With regard to optical sensing, we developed three CMOS based sensor microsystems based on different luminescence detection methodologies targeting different applications. In Chapter 2, a phase luminometric sensor system based on frequency domain lifetime measurement is presented. Frequency domain lifetime measurement is employed due to the fact that the luminescence lifetimes we are trying to detect in this dissertation (fluorescence) are on the order of several hundred nanoseconds to few microseconds and it requires complex CMOS circuitry to realize the direct time domain lifetime detection. A non-linear phase detector circuit technique is proposed and implemented to enhance the performance of the sensor system. In the following Chapter 3, we concentrated on the development of multi-sensor microsystem based on luminescence intensity measurement and pin-printed sensor microarrays. Low power, high sensitivity and noise suppressing CMOS imager is developed to image the luminescence from the sensor microarrays.

Functionality of the sensor system is proved by experimental results and thermal effect on different luminophores is also studied using this multi-sensor system. Finally in Chapter 4, as an exploring first step towards multi-sensor lifetime imaging, Direct Time Interval Measurement (DTIM) is proposed as a new signal processing technique. A CMOS DTIM IC is developed based on RGC TIA and TDC circuits. DTIM technique hurdles and difficulties are also discussed.

In the experiments to prove the functionality of these sensor microsystem prototypes, oxygen is used as an analyte and luminophores (fluorophores) $[Ru(bpy)_3]^{2+}$ and $[Ru(dpp)_3]^{2+}$ are employed as the sensing element since we have previous experience and performed intensive studies on this kind of oxygen detection system. They can be altered by other luminophores or other optical sensing elements for analytes in different kinds of biochemical applications.

6.1.2 ELECTROCHEMICAL SENSING

Comparing to optical sensing, electrochemical sensing requires less effort on the development of detection circuit and it provides more convenient interface between fluidic biochemical samples and the signal processing electronics for system integration. With regard to electrochemical sensing, we concentrated on the bacteria activity monitoring based on conductometric methodology. A CMOS conductometric IC with a digital output is developed to monitor the growth of bacteria and to detect the bacteria by employing bacteriophage as a sensing element. This is the first research work of integrating CMOS conductometric circuit and bacteriophage in a system to monitor the bacterial activity.

6.2 FUTURE WORK

There are still a lot of issues to be addressed before these sensor microsystem prototypes developed in this dissertation can enter practical use.

6.2.1 OPTICAL SENSING

As explained earlier, one of the drawbacks in optical sensing system is that it requires many optical components such as filters, lens and excitation sources (laser, LED, etc.). To realize an integrated sensor microsystem, these components have to be well integrated with the CMOS ICs and sensor microarrays. In future, near field imaging technique, custom fabricated PDMS/PMMA polymer filter, micro LED arrays and other system integration technologies are necessary to be employed to perform the system integration of optical sensing systems.

6.2.2 ELECTROCHEMICAL SENSING

The electrochemical sensor system developed in this dissertation is for bacteria detection. It is capable to detect 10^2 CFU/mL within 10 hours, which is the best performance among the reported CMOS based bacteria detection systems. However, this performance is still needs to be improved for real-time monitoring and rapid point-of-care applications. In future, different structures of electrodes and other techniques such as surface acoustic waves for forcing the joining of bacteria and phages are necessary to be examined to accelerate the detection time and further improve the detection limit. Also, integration of large sensor arrays for bacteria activity monitoring using microfluidics and the developed CMOS IC is a promising research direction for high throughput screening and drug discovery.

6.2.3 General Considerations for Biochemical Sensor Microsystems

As for the general biochemical sensor microsystems, either optical or electrochemical, two important components not discussed in this dissertation and that need to be examined in future: the sampling aperture and the processing electronics for storage, display and transmission. Since the environment for most of the biochemical applications is fluidic, the sampling aperture such as fluidic chamber, fluidic channel and fluidic mixer are very important for microsystems to hold and condition the biochemical samples. To fabricate these sampling apertures and integrating them with the developed CMOS ICs is an important research aspect in future. For an applicable sensor microsystem device, it is also important to be systematically complete, which means it would not require extra table top electronics such as PCs, DAC cards and function generators to perform the sensing and signal processing. In future, to integrate these necessary electronics components with the developed CMOS ICs using microprocessors, FPGAs or DSPs is another research direction to enable an applicable sensor microsystem.

In conclusion, several sensor microsystem prototypes are presented based on optical/electrochemical methodologies and CMOS detection and processing ICs in this dissertation. We verified the functionality and feasibility of these microsystem prototypes used for biochemical applications. In future, based on the principles and prototypes discussed in this dissertation, we can develop novel sensor microsystems for different biochemical applications based on CMOS detection and signal processing in the manner of smaller size, lower cost and equivalent/better performance comparing to conventional available instruments.

REFERENCES

[1] A. Hoffman, "Galileo: Astronomer and Physicist," *Catholic Library World,* vol. 79, pp. 320-320, 2009.

[2] L. Behr, "Bourdon tube pressure gauge.," *Journal of the Optical Society of America and Review of Scientific Instruments,* vol. 10, pp. 710-710, Jun 1925.

[3] J. H. Filloux, "Deep Sea Tide Gauge with Optical Readout of Bourdon Tube Rotations," *Nature,* vol. 226, pp. 935-&, 1970.

[4] A. G. Bell, "US patent 174465," 1876.

[5] W. S. Hughes, "The potential difference between glass and electrolytes in contact with the glass," *Journal of the American Chemical Society,* vol. 44, pp. 2860-2867, Jul-Dec 1922.

[6] C. Mitchell, Ainsworth, "Science and the Detective," *The American Journal of Police Science,* vol. 3, pp. 169-182, March/April 1932.

[7] L. C. Clark, "Monitor and Control of Blood and Tissue Oxygen Tensions," *Transactions American Society for Artificial Internal Organs,* vol. 2, pp. 41-&, 1956.

[8] L. C. Clark, Jr. and C. Lyons, "Electrode systems for continuous monitoring in cardiovascular surgery," *Ann N Y Acad Sci,* vol. 102, pp. 29-45, Oct 31 1962.

[9] A. Ivask*, et al.*, "Detection of organomercurials with sensor bacteria," *Analytical Chemistry,* vol. 73, pp. 5168-5171, Nov 1 2001.

[10] D. Ivnitski*, et al.*, "Biosensors for detection of pathogenic bacteria," *Biosensors & Bioelectronics,* vol. 14, pp. 599-624, Oct 1999.

[11] J. C. Venter*, et al.*, "The sequence of the human genome," *Science,* vol. 291, pp. 1304-+, Feb 16 2001.

[12] H. Park*, et al.*, "Discovery of common Asian copy number variants using integrated high-resolution array CGH and massively parallel DNA sequencing," *Nature Genetics,* vol. 42, pp. 400-U61, May 2010.

[13] J. P. Goddard and J. L. Reymond, "Enzyme assays for high-throughput screening," *Current Opinion in Biotechnology,* vol. 15, pp. 314-322, Aug 2004.

[14] W. F. An and N. Tolliday, "Cell-Based Assays for High-Throughput Screening," *Molecular Biotechnology,* vol. 45, pp. 180-186, Jun 2010.

[15] A. Lambrianou*, et al.*, "Protein engineering and electrochemical biosensors," *Biosensing for the 21st Century,* vol. 109, pp. 65-96, 2008.

[16] J. L. Flanagan*, et al.*, "Computer-Steered Microphone Arrays for Sound Transduction in Large Rooms," *Journal of the Acoustical Society of America,* vol. 78, pp. 1508-1518, 1985.

[17] P. R. Scheeper*, et al.*, "A new measurement microphone based on MEMS technology," *Journal of Microelectromechanical Systems,* vol. 12, pp. 880-891, Dec 2003.

[18] L. M. Roylance and J. B. Angell, "Batch-Fabricated Silicon Accelerometer," *Ieee Transactions on Electron Devices,* vol. 26, pp. 1911-1917, 1979.

[19] M. Lemkin and B. E. Boser, "A three-axis micromachined accelerometer with a CMOS position-sense interface and digital offset-trim electronics," *Ieee Journal of Solid-State Circuits,* vol. 34, pp. 456-468, Apr 1999.

[20] T. L. Gustavson, *et al.*, "Precision rotation measurements with an atom interferometer gyroscope," *Physical Review Letters,* vol. 78, pp. 2046-2049, Mar 17 1997.
[21] J. A. Geen, *et al.*, "Single-chip surface micromachined integrated gyroscope with 50 degrees/h allan deviation," *Ieee Journal of Solid-State Circuits,* vol. 37, pp. 1860-1866, Dec 2002.
[22] H. Iams and B. Salzberg, "The secondary emission phototube," *Proceedings of the Institute of Radio Engineers,* vol. 23, pp. 55-64, Jan 1935.
[23] S. R. Arridge, "Optical tomography in medical imaging," *Inverse Problems,* vol. 15, pp. R41-R93, Apr 1999.
[24] C. Corot, *et al.*, "Recent advances in iron oxide nanocrystal technology for medical imaging," *Advanced Drug Delivery Reviews,* vol. 58, pp. 1471-1504, Dec 1 2006.
[25] R. F. Wagner and D. G. Brown, "Unified Snr Analysis of Medical Imaging-Systems," *Physics in Medicine and Biology,* vol. 30, pp. 489-518, 1985.
[26] R. A. Wolthuis, *et al.*, "Development of Medical Pressure and Temperature Sensors Employing Optical-Spectrum Modulation," *Ieee Transactions on Biomedical Engineering,* vol. 38, pp. 974-981, Oct 1991.
[27] A. M. Yu, *et al.*, "Nanostructured electrochemical sensor based on dense gold nanoparticle films," *Nano Letters,* vol. 3, pp. 1203-1207, Sep 2003.
[28] G. Marrazza, *et al.*, "Disposable DNA electrochemical sensor for hybridization detection," *Biosensors & Bioelectronics,* vol. 14, pp. 43-51, Jan 1 1999.
[29] K. Hashimoto, *et al.*, "Novel DNA Sensor for Electrochemical Gene Detection," *Analytica Chimica Acta,* vol. 286, pp. 219-224, Feb 18 1994.
[30] Y. B. Hu, *et al.*, "Direct Measurement of Glutamate Release in the Brain Using a Dual Enzyme-Based Electrochemical Sensor," *Brain Research,* vol. 659, pp. 117-125, Oct 3 1994.
[31] M. S. Wilson and W. Y. Nie, "Electrochemical multianalyte immunoassays using an array-based sensor," *Analytical Chemistry,* vol. 78, pp. 2507-2513, Apr 15 2006.
[32] B. D. Maccraith, "Enhanced Evanescent Wave Sensors Based on Sol Gel-Derived Porous-Glass Coatings," *Sensors and Actuators B-Chemical,* vol. 11, pp. 29-34, Mar 1 1993.
[33] J. H. Shin, *et al.*, "Enhanced serum carbon dioxide measurements with a silicone rubber-based carbonate ion-selective electrode and a high-pH dilution buffer," *Analytical Chemistry,* vol. 68, pp. 221-225, Jan 1 1996.
[34] B. C. Fagan, *et al.*, "Modification of micro-cantilever sensors with sol-gels to enhance performance and immobilize chemically selective phases," *Talanta,* vol. 53, pp. 599-608, Dec 4 2000.
[35] J. Tamayo, "Study of the noise of micromechanical oscillators under quality factor enhancement via driving force control," *Journal of Applied Physics,* vol. 97, pp. -, Feb 15 2005.
[36] B. Bae, *et al.*, "Design optimization of a piezoresistive pressure sensor considering the output signal-to-noise ratio," *Journal of Micromechanics and Microengineering,* vol. 14, pp. 1597-1607, Dec 2004.
[37] K. D. Benkstein, *et al.*, "Integration of nanostructured materials with MEMS microhotplate platforms to enhance chemical sensor performance," *Journal of Nanoparticle Research,* vol. 8, pp. 809-822, Dec 2006.
[38] R. Saeidpourazar and N. Jalili, "Microcantilever-Based Force Tracking With Applications to High-Resolution Imaging and Nanomanipulation," *Ieee Transactions on Industrial Electronics,* vol. 55, pp. 3935-3943, Nov 2008.

[39] C. P. Joshi and A. H. Titus, "Towards an autonomous integrated sensor system," *Sensors and Actuators B-Chemical,* vol. 139, pp. 110-117, May 20 2009.
[40] F. Yang and A. H. Titus, "Integrated colour detectors in 0.18 mu m CMOS technology," *Electronics Letters,* vol. 43, pp. 1279-1281, Nov 8 2007.
[41] V. P. Chodavarapu*, et al.*, "CMOS-based phase fluorometric oxygen sensor system," *IEEE Transactions on Circuits and Systems I-Regular Papers,* vol. 54, pp. 111-118, 2007.
[42] H. Eltoukhy*, et al.*, "A 0.18-/mu m CMOS bioluminescence detection lab-on-chip," *IEEE Journal of Solid-State Circuits,* vol. 41, pp. 651-662, Mar 2006.
[43] S. C. Chang, "Thin-Film Semiconductor Nox Sensor," *Ieee Transactions on Electron Devices,* vol. 26, pp. 1875-1880, 1979.
[44] M. Esashi and T. Matsuo, "Integrated Micro Multi Ion Sensor Using Field-Effect of Semiconductor," *Ieee Transactions on Biomedical Engineering,* vol. 25, pp. 184-192, 1978.
[45] J. H. Lee*, et al.*, "Evaluation of Semiconductor Gas Sensor System for Online Ethanol Estimation," *Biotechnology Letters,* vol. 3, pp. 251-256, 1981.
[46] R. J. Baker, *CMOS Circuit Design, Layout, and Simulation*, 2 ed. New York: Wiley-IEEE Press, 2008.
[47] E. R. Fossum, "CMOS image sensors: Electronic camera-on-a-chip," *Ieee Transactions on Electron Devices,* vol. 44, pp. 1689-1698, Oct 1997.
[48] V. P. Chodavarapu*, et al.*, "Differential read-out architecture for CMOS ISFET microsystems," *Electronics Letters,* vol. 41, pp. 698-699, Jun 9 2005.
[49] U. Brand*, et al.*, "Bio-Field-Effect Transistors for Process-Control in Biotechnology," *Sensors and Actuators B-Chemical,* vol. 4, pp. 315-318, Jun 1991.
[50] J. M. Bustillo*, et al.*, "Surface micromachining for microelectromechanical systems," *Proceedings of the Ieee,* vol. 86, pp. 1552-1574, Aug 1998.
[51] C. J. Lu*, et al.*, "First-generation hybrid MEMS gas chromatograph," *Lab on a Chip,* vol. 5, pp. 1123-1131, 2005.
[52] W. P. Eaton and J. H. Smith, "Micromachined pressure sensors: Review and recent developments," *Smart Materials & Structures,* vol. 6, pp. 530-539, Oct 1997.
[53] N. V. Lavrik*, et al.*, "Cantilever transducers as a platform for chemical and biological sensors," *Review of Scientific Instruments,* vol. 75, pp. 2229-2253, Jul 2004.
[54] C. M. Ho and Y. C. Tai, "Micro-electro-mechanical-systems (MEMS) and fluid flows," *Annual Review of Fluid Mechanics,* vol. 30, pp. 579-612, 1998.
[55] G. Lin*, et al.*, "Surface micromachined polysilicon heart cell force transducer," *Journal of Microelectromechanical Systems,* vol. 9, pp. 9-17, Mar 2000.
[56] H. Luo*, et al.*, "A post-CMOS micromachined lateral accelerometer," *Journal of Microelectromechanical Systems,* vol. 11, pp. 188-195, Jun 2002.
[57] A. V. Chavan and K. D. Wise, "A monolithic fully-integrated vacuum-sealed CMOS pressure sensor," *Ieee Transactions on Electron Devices,* vol. 49, pp. 164-169, Jan 2002.
[58] Y. C. Tseng*, et al.*, "Monolithic integration of carbon nanotube devices with silicon MOS technology," *Nano Letters,* vol. 4, pp. 123-127, Jan 2004.
[59] E. Yoon and K. D. Wise, "An Integrated Mass-Flow Sensor with on-Chip Cmos Interface Circuitry," *Ieee Transactions on Electron Devices,* vol. 39, pp. 1376-1386, Jun 1992.

[60] N. Kamamichi, *et al.*, "Fabrication of Bucky Gel Actuator/Sensor Devices Based on Printing Method," *2008 Ieee/Rsj International Conference on Robots and Intelligent Systems, Vols 1-3, Conference Proceedings,* pp. 582-587, 4181, 2008.

[61] S. Yokoyama, *et al.*, "Two-photon-induced polymerization in a laser gain medium for optical microstructure," *Applied Physics Letters,* vol. 82, pp. 3221-3223, May 12 2003.

[62] I. H. Chang, *et al.*, "Miniaturized lead sensor based on lead-specific DNAzyme in a manocapillary interconnected microfluidic device," *Environmental Science & Technology,* vol. 39, pp. 3756-3761, May 15 2005.

[63] V. Chodavarapu, in Ph. D. Dissertation, Department of Electrical Engineering, University of Buffalo, The State University of New York, 2006.

[64] J. R. Lakowicz, *Principles of Fluorescence Spectroscopy*, 2 ed. New York: Kluwer Academic/Plenum Publishers, 1999.

[65] E. J. Cho and F. V. Bright, "Optical sensor array and integrated light source," *Analytical Chemistry,* vol. 73, pp. 3289-3293, Jul 15 2001.

[66] L. Yao, *et al.*, "Sensitivity-Enhanced CMOS Phase Luminometry System Using Xerogel-Based Sensors," *Ieee Transactions on Biomedical Circuits and Systems,* vol. 3, pp. 304-311, Oct 2009.

[67] M. Davenport, *et al.*, "Chemical sensing systems using xerogel-based sensor elements and CMOS photodetectors," *IEEE Sensors Journal,* vol. 4, pp. 180-188, 2004.

[68] S. S. Karri, *et al.*, "Image analysis for multi-analyte xerogel based sensor arrays," *2005 Ieee Sensors, Vols 1 and 2,* pp. 373-376, 1413, 2005.

[69] C. H. Contag and M. H. Bachmann, "Advances in vivo bioluminescence imaging of gene expression," *Annual Review of Biomedical Engineering,* vol. 4, pp. 235-260, 2002.

[70] W. E. Huang, *et al.*, "Dissolved oxygen imaging in a porous medium to investigate biodegradation in a plume with limited electron acceptor supply," *Environmental Science & Technology,* vol. 37, pp. 1905-1911, May 1 2003.

[71] P. Hartmann, *et al.*, "Oxygen flux fluorescence lifetime imaging," *Sensors and Actuators B-Chemical,* vol. 38, pp. 110-115, Jan-Feb 1997.

[72] V. P. Chodavarapu, *et al.*, "CMOS mixed-signal phase detector for integrated chemical sensor systems," *2005 Ieee Sensors, Vols 1 and 2,* pp. 1068-1071,1413, 2005.

[73] H. S. Wong, "Technology and device scaling considerations for CMOS imagers," *Ieee Transactions on Electron Devices,* vol. 43, pp. 2131-2142, Dec 1996.

[74] G. Patounakis, *et al.*, "Active CMOS array sensor for time-resolved fluorescence detection," *Ieee Journal of Solid-State Circuits,* vol. 41, pp. 2521-2530, Nov 2006.

[75] M. Zourob, *et al.*, *Principles of Bacterial Detection: Biosensors, Recognition Receptors and Microsystems*. New York: Springer, 2008.

[76] B. W. Brooks, *et al.*, "Evaluation of a monoclonal antibody-based enzyme-linked immunosorbent assay for detection of Campylobacter fetus in bovine preputial washing and vaginal mucus samples," *Vet Microbiol,* vol. 103, pp. 77-84, Oct 5 2004.

[77] E. de Boer and R. R. Beumer, "Methodology for detection and typing of foodborne microorganisms," *Int J Food Microbiol,* vol. 50, pp. 119-30, Sep 15 1999.

[78] R. Kumar, *et al.*, "Evaluation of culture, ELISA and PCR assays for the detection of Salmonella in seafood," *Lett Appl Microbiol,* vol. 46, pp. 221-6, Feb 2008.

[79] W. B. Shim, *et al.*, "Production of monoclonal antibody against Listeria monocytogenes and its application to immunochromatography strip test," *J Microbiol Biotechnol,* vol. 17, pp. 1152-61, Jul 2007.
[80] V. Velusamy, *et al.*, "An overview of foodborne pathogen detection: In the perspective of biosensors," *Biotechnology Advances,* vol. 28, pp. 232-254, Mar-Apr 2010.
[81] J. Dupont, *et al.*, "Calibration of the impedance method for rapid quantitative estimation of Escherichia coli in live marine bivalve molluscs," *Journal of Applied Microbiology,* vol. 96, pp. 894-902, 2004.
[82] K. Horvath, *et al.*, "Using automatic conductimetry for monitoring spoilage bacteria on chilled pork cutlets," *Acta Alimentaria,* vol. 36, pp. 283-291, Jun 2007.
[83] S. Mirrett, *et al.*, "Controlled clinical comparison of BacT/ALERT standard aerobic medium with BACTEC standard aerobic medium for culturing blood," *Journal of Clinical Microbiology,* vol. 41, pp. 2391-2394, Jun 2003.
[84] A. L. Myllyniemi, *et al.*, "An indirect conductimetric screening method for the detection of antibiotic residues in bovine kidneys," *Analyst,* vol. 127, pp. 1247-1251, 2002.
[85] R. Bashir, "BioMEMS: state-of-the-art in detection, opportunities and prospects," *Advanced Drug Delivery Reviews,* vol. 56, pp. 1565-1586, Sep 22 2004.
[86] G. H. Wu, *et al.*, "Bioassay of prostate-specific antigen (PSA) using microcantilevers," *Nature Biotechnology,* vol. 19, pp. 856-860, Sep 2001.
[87] E. Ghafar-Zadeh, *et al.*, "Differential Monitoring of Bacterial Growth using CMOS Capacitive Sensors," *Ieee Transactions on Biomedical Circuits and Systems,* 2010, In press.
[88] S. H. Huang, "Detection of Escherichia coli using CMOS array photo sensor-based enzyme biochip detection system," *Sensors and Actuators B-Chemical,* vol. 133, pp. 561-564, Aug 12 2008.
[89] N. Nikkhoo, *et al.*, "A CMOS Integrated Bacterial Sensor for Rapid Detection of Pseudomonas aeruginosa," *2008 Ieee Biomedical Circuits and Systems Conference - Intelligent Biomedical Systems (Biocas),* pp. 213-216, 2008.
[90] J. Q. Boedicker, *et al.*, "Detecting bacteria and determining their susceptibility to antibiotics by stochastic confinement in nanoliter droplets using plug-based microfluidics," *Lab on a Chip,* vol. 8, pp. 1265-1272, Aug 2008.
[91] K. R. King, *et al.*, "A high-throughput microfluidic real-time gene expression living cell array," *Lab on a Chip,* vol. 7, pp. 77-85, 2007.
[92] G. A. Campbell and R. Mutharasan, "Detection of pathogen Escherichia coli O157:H7 using self-excited PZT-glass microcantilevers," *Biosens Bioelectron,* vol. 21, pp. 462-73, Sep 15 2005.
[93] R. Guntupalli, *et al.*, "A magnetoelastic resonance biosensor immobilized with polyclonal antibody for the detection of Salmonella typhimurium," *Biosens Bioelectron,* vol. 22, pp. 1474-9, Feb 15 2007.
[94] S. Pal, *et al.*, "Nanowire labeled direct-charge transfer biosensor for detecting Bacillus species," *Biosens Bioelectron,* vol. 22, pp. 2329-36, Apr 15 2007.
[95] A. D. Taylor, *et al.*, "Quantitative and simultaneous detection of four foodborne bacterial pathogens with a multi-channel SPR sensor," *Biosens Bioelectron,* vol. 22, pp. 752-8, Dec 15 2006.
[96] O. Tokarskyy and D. L. Marshall, "Immunosensors for rapid detection of Escherichia coli O157:H7 - perspectives for use in the meat processing industry," *Food Microbiol,* vol. 25, pp. 1-12, Feb 2008.

[97] J. Waswa, *et al.*, "Direct detection of E. Coli O157:H7 in selected food systems by a surface plasmon resonance biosensor," *LWT - Food Science and Technology,* vol. 40, pp. 187-192, 2007.
[98] F. Perez, *et al.*, "Rapid detection of Escherichia coli in water by a culture-based amperometric method," *Analytica Chimica Acta,* vol. 427, pp. 149-154, 2001.
[99] J. L. Brooks, *et al.*, "Experimental enzyme-linked amperometric immunosensors for the detection of salmonellas in foods," *J Appl Bacteriol,* vol. 73, pp. 189-96, Sep 1992.
[100] C. Sun, *et al.*, "Electrochemical DNA biosensor based on proximity-dependent DNA ligation assays with DNAzyme amplification of hairpin substrate signal," *Biosens Bioelectron,* Apr 24.
[101] S. Balasubramanian, *et al.*, "Lytic phage as a specific and selective probe for detection of Staphylococcus aureus--A surface plasmon resonance spectroscopic study," *Biosens Bioelectron,* vol. 22, pp. 948-55, Jan 15 2007.
[102] A. Singh, *et al.*, "Immobilization of bacteriophages on gold surfaces for the specific capture of pathogens," *Biosens Bioelectron,* vol. 24, pp. 3645-51, Aug 15 2009.
[103] F. Xie, *et al.*, "Amorphous magnetoelastic sensors for the detection of biological agents," *Intermetallics,* vol. 17, pp. 270-273, 2009.
[104] S. Huang, *et al.*, "Optimization of phage-based magnetoelastic biosensor performance," in *Technical Proceedings of the 2008 NSTI Nanotechnology Conference and Trade Show, NSTI-Nanotech, Nanotechnology 2008*, 2008, pp. 642-645.
[105] E. Kutter and A. Sulakvelidze, *Bacteriophages: Biology and Applications*. Boca Raton, Florida: CRC Press, 2005.
[106] S. Chemburu, *et al.*, "Detection of pathogenic bacteria in food samples using highly-dispersed carbon particles," *Biosensors & Bioelectronics,* vol. 21, pp. 491-499, Sep 15 2005.
[107] C. Ruan, *et al.*, "A bienzyme electrochemical biosensor coupled with immunomagnetic separation for rapid detection of Escherichia coli O15 : H7 in food samples," *Transactions of the Asae,* vol. 45, pp. 249-255, Jan-Feb 2002.
[108] L. J. Yang, *et al.*, "Interdigitated microelectrode (IME) impedance sensor for the detection of viable Salmonella typhimurium," *Biosensors & Bioelectronics,* vol. 19, pp. 1139-1147, May 15 2004.
[109] L. Yang and R. Bashir, "Electrical/electrochemical impedance for rapid detection of foodborne pathogenic bacteria," *Biotechnology Advances,* vol. 26, pp. 135-150, Mar-Apr 2008.
[110] I. M. Kolthoff, *et al.*, "Acid-Base Equilibria in Acetonitrile - Spectrophotometric and Conductometric Determination of Dissociation of Various Acids," *Journal of the American Chemical Society,* vol. 83, pp. 3927-&, 1961.
[111] Z. Muhammad-Tahir and E. C. Alocilja, "Fabrication of a disposable biosensor for Escherichia coli O157 : H7 detection," *Ieee Sensors Journal,* vol. 3, pp. 345-351, Aug 2003.
[112] S. J. Labrie, *et al.*, "Bacteriophage resistance mechanisms," *Nature Reviews Microbiology,* vol. 8, pp. 317-327, May 2010.
[113] R. Schuch, *et al.*, "A bacteriolytic agent that detects and kills Bacillus anthracis," *Nature,* vol. 418, pp. 884-889, Aug 22 2002.
[114] H. Katznelson and M. D. Sutton, "A Rapid Phage Plaque Count Method for the Detection of Bacteria as Applied to the Demonstration of Internally Borne Bacterial Infections of Seed," *Journal of Bacteriology,* vol. 61, pp. 689-701, 1951.

[115] H. W. Ackermann and H. M. Krisch, "A catalogue of T4-type bacteriophages," *Arch Virol,* vol. 142, pp. 2329-45, 1997.
[116] E. S. Miller*, et al.*, "Bacteriophage T4 genome," *Microbiol Mol Biol Rev,* vol. 67, pp. 86-156, table of contents, Mar 2003.
[117] R. Ehret*, et al.*, "Monitoring of cellular behaviour by impedance measurements on interdigitated electrode structures," *Biosensors & Bioelectronics,* vol. 12, pp. 29-41, 1997.
[118] R. Pethig and G. H. Markx, "Applications of dielectrophoresis in biotechnology," *Trends Biotechnol,* vol. 15, pp. 426-32, Oct 1997.
[119] C. McDonagh*, et al.*, "Tailoring of sol-gel films for optical sensing of oxygen in gas and aqueous phase," *Analytical Chemistry,* vol. 70, pp. 45-50, 1998.
[120] S. J. Kim*, et al.*, "Enhanced oxygen detection using porous polymeric gratings with integrated recognition elements," *Sensors and Actuators B-Chemical,* vol. 130, pp. 758-764, 2008.
[121] P. C. A. Jeronimo*, et al.*, "Optical sensors and biosensors based on sol-gel films," *Talanta,* vol. 72, pp. 13-27, 2007.
[122] W. Trettnak*, et al.*, "Miniaturized luminescence lifetime-based oxygen sensor instrumentation utilizing a phase modulation technique," *Sensors and Actuators B-Chemical,* vol. 36, pp. 506-512, 1996.
[123] C. McDonagh*, et al.*, "Phase fluorometric dissolved oxygen sensor," *Sensors and Actuators B-Chemical,* vol. 74, pp. 124-130, 2001.
[124] Z. Y. Tao*, et al.*, "Stable sensors with tunable sensitivities based on class II xerogels," *Analytical Chemistry,* vol. 78, pp. 1939-1945, 2006.
[125] V. P. Chodavarapu*, et al.*, "Multi-sensor system based on phase detection, an LED array, and luminophore-doped xerogels," *Electronics Letters,* vol. 41, pp. 1031-1033, 2005.
[126] V. P. Chodavarapu*, et al.*, "CMOS Integrated Luminescence Oxygen Multi-Sensor System," *Electronics Letters,* vol. 43, pp. 688-689, 2007.
[127] S. Nagl and O. S. Wolfbeis, "Optical multiple chemical sensing: status and current challenges," *Analyst,* vol. 132, pp. 507-511, 2007.
[128] M. Bally*, et al.*, "Optical microarray biosensing techniques," *Surface and Interface Analysis,* vol. 38, pp. 1442-1458, Nov 2006.
[129] F. S. Ligler*, et al.*, "The array biosensor: Portable, automated systems," *Analytical Sciences,* vol. 23, pp. 5-10, Jan 2007.
[130] E. J. Cho*, et al.*, "Multianalyte pin-printed biosensor arrays based on protein-doped xerogels," *Analytical Chemistry,* vol. 74, pp. 6177-6184, Dec 15 2002.
[131] P. Calvert, "Inkjet printing for materials and devices," *Chemistry of Materials,* vol. 13, pp. 3299-3305, Oct 2001.
[132] W. A. Zhao and A. van den Berg, "Lab on paper," *Lab on a Chip,* vol. 8, pp. 1988-1991, 2008.
[133] G. Wallraff*, et al.*, "DNA sequencing on a chip," *Chemtech,* vol. 27, pp. 22-32, Feb 1997.
[134] Y. Tang*, et al.*, "Tailored xerogel-based sensor arrays and artificial neural networks yield improved O-2 detection accuracy and precision," *Analyst,* vol. 131, pp. 1129-1136, 2006.
[135] T. Vo-Dinh*, et al.*, "DNA biochip using a phototransistor integrated circuit," *Analytical Chemistry,* vol. 71, pp. 358-363, Jan 15 1999.
[136] M. A. Gaspar*, et al.*, "Fabrication of a CMOS biochip for DNA diagnostics," *Abstracts of Papers of the American Chemical Society,* vol. 230, pp. U1114-U1114, Aug 28 2005.

[137] K. Salama, *et al.*, "Modeling and simulation of luminescence detection platforms," *Biosensors & Bioelectronics,* vol. 19, pp. 1377-1386, Jun 15 2004.
[138] J. Nakamura, *Imager Sensors and Signal Processing for Digital Still Cameras*: Taylor & Francis Group, 2006.
[139] S. G. P. Harvey and J. L. Bahr, "A temperature-controlled complementary metal oxide semiconductor camera," *Proceedings of the Institution of Mechanical Engineers Part B-Journal of Engineering Manufacture,* vol. 218, pp. 1217-1222, Sep 2004.
[140] B. C. Kim, *et al.*, "Temporal Noise Analysis and Reduction Method in CMOS Image Sensor Readout Circuit," *Ieee Transactions on Electron Devices,* vol. 56, pp. 2489-2495, Nov 2009.
[141] Q. Gu, *et al.*, "Laser Doppler blood flow complementary metal oxide semiconductor imaging sensor with analog on-chip processing," *Applied Optics,* vol. 47, pp. 2061-2069, Apr 20 2008.
[142] W. RedmanWhite, "A high bandwidth constant g(m) and slew-rate rail-to-rail CMOS input circuit and its application to analog cells for low voltage VLSI systems," *Ieee Journal of Solid-State Circuits,* vol. 32, pp. 701-712, May 1997.
[143] T. Nystrom, "Stationary-phase physiology," *Annu Rev Microbiol,* vol. 58, pp. 161-81, 2004.
[144] H. Makinoshima, *et al.*, "Growth phase-coupled alterations in cell structure and function of Escherichia coli," *J Bacteriol,* vol. 185, pp. 1338-45, Feb 2003.
[145] I. A. Swinnen, *et al.*, "Predictive modelling of the microbial lag phase: a review," *Int J Food Microbiol,* vol. 94, pp. 137-59, Jul 15 2004.
[146] T. P. Robinson, *et al.*, "The effect of inoculum size on the lag phase of Listeria monocytogenes," *Int J Food Microbiol,* vol. 70, pp. 163-73, Oct 22 2001.
[147] N. Gnanou Besse, *et al.*, "Effect of the inoculum size on Listeria monocytogenes growth in structured media," *Int J Food Microbiol,* vol. 110, pp. 43-51, Jul 1 2006.
[148] C. S. Hayes and D. A. Low, "Signals of growth regulation in bacteria," *Curr Opin Microbiol,* vol. 12, pp. 667-73, Dec 2009.
[149] S. Pearl, *et al.*, "Nongenetic individuality in the host-phage interaction," *PLoS Biol,* vol. 6, p. e120, May 20 2008.